DISSERTATION

Size effects in single crystal plasticity of copper under uniaxial loading

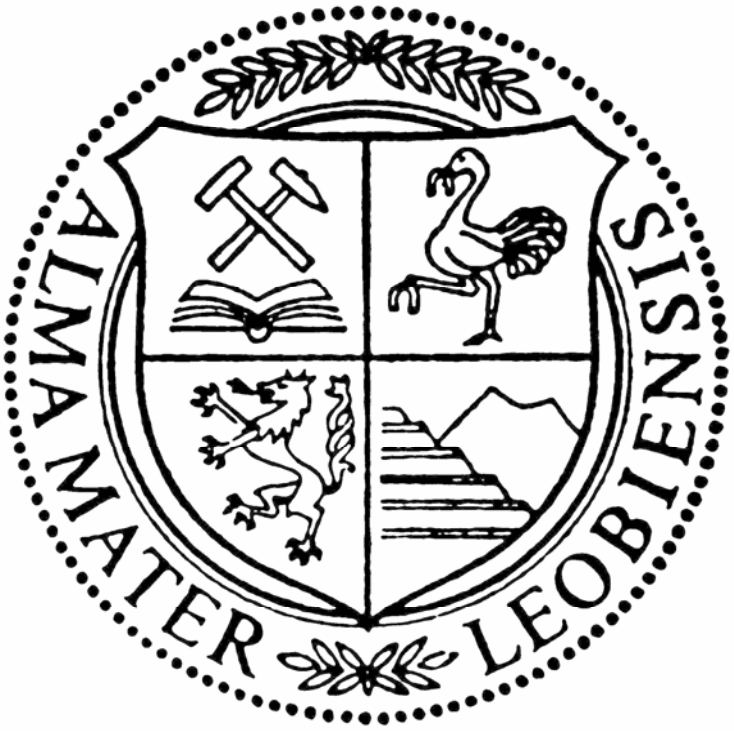

von Dipl. Ing. Daniel Kiener

An der Montanuniversität Leoben eingereichte Dissertation zur Erlangung des Doktorgrades der montanistischen Wissenschaften.

Die vorliegende Arbeit ist im Rahmen einer Kooperation der Österreichischen Akademie der Wissenschaften und der Materials Center Leoben Forschung GmbH entstanden (Projekt SP17/2).

Ich erkläre an Eides statt, dass diese Arbeit von mir selbstständig und unter Verwendung der angegebenen Literatur durchgeführt wurde.

Leoben, September 2007 Dipl. Ing. Daniel Kiener

Der Mensch hat dreierlei Wege klug zu handeln:
Erstens durch Nachdenken, das ist das edelste;
zweitens durch Nachahmen, das ist das leichteste;
drittens durch Erfahrung, das ist das bitterste.

Konfuzius

Man muss viel gelernt haben, um über das, was man nicht weiß, fragen zu können.

Jean-Jacques Rousseau

Danksagung

An dieser Stelle möchte ich mich bei all jenen bedanken, die mich während meiner Dissertation unterstützt haben. Vor allem bei meiner Familie, die mir diesen Weg ermöglicht hat und mir immer zur Seite gestanden ist.

Eine Doktorarbeit kann nur in einem angenehmen Umfeld gelingen. Deshalb möchte ich an erster Stelle allen Mitarbeitern des Erich Schmid Instituts danken, die mich so herzlich aufgenommen haben und es mir ermöglichten, in einem anregenden, guten Arbeitsklima zu forschen. Aus dem Werkstättenbereich danke ich besonders Franz Hubner für die komplette Adaption des Mikroindenters. In Metallographie und TEM Präparation haben Edeltraud Haberz und Gabriele Moser für mich das Präparieren unzähliger Proben übernommen. Sollte einmal ein Gerät nicht funktioniert haben, wurde es von Herwig Felber oder Gerald Reiter repariert. Jörg Thomas war am TEM immer zur Stelle.
Großer Dank geht auch an alle wissenschaftlichen Mitarbeiter, Dissertanten, Diplomanden und studentischen Mitarbeitern für inspirierende Diskussionen zu verschiedensten Problemstellungen. Stellvertretend für viele möchte ich mich bei Dr. Christian Motz, Dr. Boriana Rashkova, Prof. Otmar Kolednik, Dr. Werner Prantl, Dr. Gerhard Jesner, Dr. Martin Hafok, DI Martin Rester, DI Stefan Massl, DI Klaus Martinschitz, Malcolm Werchota, Hans-Peter Wörgötter und Wolfgang Pranger für ihr kritischen Anmerkungen bedanken. Besonderer Dank geht an Wolfgang Grosinger für seinen unermüdlichen Einsatz zur Verwirklichung der Mikrozugversuche.

Dr. Thomas Chudoba und Dr. Volker Linß von der Firma ASMEC möchte ich für ihre Kooperation bei der Adaption ihres UNAT für unser REM und die flexible Softwarelösung danken.

Für die wissenschaftliche Kooperation geht mein Dank an Prof. Monika Jenko (Institute of Metals and Technology, Slovenia), Prof. Helena van Swygenhoven und Robert Maaß (Paul Scherrer Institute, Switzerland) und Dr. Sašo Šturm (Jožef Stefan Institut, Slovenia).

Doch nicht nur das wissenschaftliche Umfeld hat zum Gelingen dieser Arbeit beigetragen. Während der Jahre meines Studiums waren immer Freunde zur Stelle, die mir bei Problemen mit Rat und Tat zur Seite gestanden haben und, sei es bei einem Kaffee oder ein paar Spritzern, zu Lösungen beigetragen haben. Namentlich erwähnen möchte ich an dieser Stelle Irene, Elfi, Verena und Daniel, Ursula und Bernd. Gesammelt bedanke ich mich aber auch bei allen „98ern“.

Mein größter Dank geht schließlich an die Betreuer dieser Arbeit. Auch wenn dies offiziell nur eine Person ist, bin ich doch zu gleichen Teilen Prof. Gerhard Dehm und Prof. Reinhard Pippan zu Dank verpflichtet. Sie haben mir nicht nur die Möglichkeit zur Dissertation am Erich Schmid Institut gegeben, sondern hatten die letzten drei Jahre auch immer ein offenes Ohr für meine Probleme. Vielmehr als für eure fachliche Kompetenz danke ich euch aber für eure Freundschaft. Gerhards verschmitztes Lächeln und Reinhards unermüdlicher Optimismus haben mir Antrieb gegeben, wenn nichts mehr zu gehen schien.

Daniel Kiener

Table of content

I Introduction

Plastic deformation in crystalline metals takes place by the shear of adjacent glide planes, which is promoted by the glide of dislocations [1]. In a perfect crystal containing dislocations, the barrier to overcome in order to initiate plastic deformation is given by the Peierls potential, which is very low. However, in most common engineering materials several constraints are present that hinder the motion of dislocations, leading to stresses exceeding the Peierls stress by far. The interaction of dislocations with these constraints leads to size effects in a manner that mechanical properties depend on a characteristic length scale of the material. This constraint can be an internal length scale, for example the grain size or an average particle spacing, but also internal strain inhomogeneities can obstruct dislocation motion. With the advent of miniaturized materials it was noticed that the external length scales in terms of sample dimension influence the mechanical properties (geometrical size effect).

Therefore, in the next paragraph a short review on the most common mechanical size effects and the according interpretation is provided. From this viewpoint, the aim of the thesis will be formulated.

1. Review on size effects and their interpretation

1.1 Size effects due to limitations by the internal length scale

The most prominent size effect caused by internal obstacles to dislocation motion is the so-called Hall – Petch effect [2-4]. Here the limiting length scale is given by the grain size:

$$\sigma = \sigma_0 + kd^{-0.5}, \tag{I.1}$$

where σ is the actual strength, σ_0 is the friction stress for infinite grain size, k is a constant, and d the grain size. σ_0 and k depend on the condition of the considered crystal [4, 5].

During deformation, the glide of dislocations is stopped at grain boundaries, which are considered as impenetrable obstacles. This leads to a pile-up of dislocations, creating a back-stress on the acting dislocation source. Therefore, the external stress required for further deformation increases. For a certain increment in global strain, equal numbers of dislocations have to be stored in individual grains. But for

smaller grain size, the spacing between individual dislocations in the created pile-up gets reduced, thus exerting a stronger back-stress on the acting source [6]. Therefore, the measured flow stress increases with decreasing grain size.
Similar size effects were observed for particles and other obstacles hindering dislocation motion. In this case the average obstacle spacing limits the stress necessary to bow out the moving dislocation to bypass the hard obstacle in terms of an Orowan mechanism [7].
A comparative review on these size effects was given by Arzt [8].

1.2 Size effects as a consequence of non-uniform deformation

In the last twenty years several experimental observations presented pronounced size effects in the presence of strain gradients caused by non-uniform deformation. Fleck et al. [9] observed increased torsional resistance of thin wires, while no effect on the tensile properties was observed. Stölken and Evans [10] reported increased bending strengths with reduced foil thickness, and several authors observed increased nanohardness with reduced indentation depth [11-13].

Non-uniform deformation requires the storage of geometrically necessary dislocations (GNDs) in the crystal, which causes a local gradient in strain. This strain gradient directly correlates to the density of GNDs ρ_G [14]:

$$\rho_G = \frac{1}{b}\left(\frac{\partial \gamma}{\partial x}\right), \tag{I.2}$$

where *b* is the Burgers vector, and γ is the shear in the slip system.
This quantity enters the classical Taylor relation:

$$\tau = \alpha G b \sqrt{\rho_S + \rho_G}\ , \tag{I.3}$$

where τ is the flow stress, α a numerical constant in the order of 0.5, *G* the shear modulus, and ρ_S the density of statistically stored dislocations.

Based on this idea, several formulations of this strain gradient theory were developed to describe the influence of strain gradients to the experimentally observed size effects under non-homogenous loading [9, 13, 15, 16]. Generally, the influence of a strain gradient χ present in the deformation field on the flow stress σ can be expressed by the following equation [13]:

$$\left(\frac{\sigma}{\sigma_0}\right) = 1 + l_0 \chi \,, \tag{I.4}$$

where σ_0 is the flow stress in the absence of a gradient and l_0 is a characteristic material length scale.

1.3 Size effects due to geometrical limitations of the external length scale

The characterization of mechanical properties in small dimensions is a major topic when considering the ongoing trend in miniaturization and the need for proper material characteristics for engineering applications in this regime. Nanoindentation is the technique commonly applied for this kind of problems, as it offers sufficiently high resolution in determining load and displacement and works almost non-destructive. Nevertheless, it suffers from the built-up of a strain gradient inherent to the method.

Recently, a novel method was developed where miniaturized compression samples are machined using focused ion beam (FIB) milling and loaded in a nanoindenter system equipped with a flat diamond punch [17]. This method removes most of the constraints present in other techniques and is able to probe mechanical properties on the micrometer and sub-micrometer scale under nominally uniaxial loading and therefore in the absence of strain gradients. Therefore, it was quite unexpected that these micro-compression specimens exhibited a strong geometrical size effect in terms of an increased flow stress with reduced sample dimensions. This observation has drawn considerable interest in the scientific community, and several groups developed similar methods and reported comparable results [17-24].

Recently, several models were formulated to explain the observed size effect. One assumption made to predict the high observed flow stresses compared to bulk single crystals is a lack in dislocation multiplication events during deformation, resulting in a dislocation free test structure and correspondingly a high flow stress necessary for dislocation nucleation. The theory governing this aspect is termed dislocation starvation theory [25]. On the other hand, cutting of pre-existing dislocations during FIB machining can reduce the average dislocation length present in the micro-compression specimen compared to the bulk crystal it was

fabricated from and introduce single-ended dislocation sources. The distribution of this arm lengths gives rise to truncation hardening [26]. Furthermore, due to the limited number of dislocations in these small structures, a statistical aspect enters the scene along with the question of correlation lengths in these miniaturized specimen [26-28].

Quite some effort was put on modeling this kind of experiments with various methods, on the one hand to examine the influence of misalignment and specimen geometry on the determined data [29-31], on the other hand to identify the mechanisms governing deformation in miniaturized compression samples [27, 32-35].

At the moment, no clear mechanism explaining the compression size effect is identified. While on the one hand *in-situ* compression tests in a transmission electron microscope (TEM) show no dislocation storage for specimen with diameters below 300 nm, *in-situ* white beam Laue diffraction during micro-compression [36] as well as post compression investigation using electron backscatter diffraction (EBSD) [37] present distinct crystal rotations due to the storage of dislocations for samples ranging from 2 µm to 8 µm in diameter.

Further questions rise by the fabrication method itself, as the ion damage during machining might influence the determined material properties [38]. Bei et al. [39] performed micro-compression experiments on whisker-like structures and reported size-independent flow stresses in the order of the theoretical shear stress, which was not observed for FIB fabricated specimen. Furthermore, they found changes of the indentation behavior due to FIB milling [40].

2. Aims and main tasks of the thesis

The aim of this thesis is to identify the mechanisms governing or contributing to the size effect observed in micro-compression experiments in order to understand small scale crystal plasticity.

Therefore, we built up a system allowing to machine micro-compression samples and perform the loading experiments *in-situ* in a scanning electron microscope (SEM) to ensure proper alignment and gain insight into the deformation process. Applying this setup, the influence of initial crystal orientation and specimen geometry on the deformation behavior and the size effect observed in single

crystal copper specimen is investigated. Characterization of the local crystal rotations during deformation is performed after loading using EBSD. The size-dependent flow stress results are compared to data obtained for copper using other miniaturized testing techniques to demonstrate the validity of the compression studies. Additionally, the mechanisms governing the flow stress of copper over several orders of magnitude in length scale are interpreted by including a source term into the Hall – Petch relation. In order to circumvent some limitations present in micro-compression testing, for example friction between sample and tip, limitations in aspect ratio, and an additional compliance at the sample base, a new method allowing to load miniaturized specimen in tension is developed. Using this method, the size-dependent properties of miniaturized single crystal copper tensile samples were characterized and compared to the results from micro-compression.

Parallel to this mechanical characterization, the ion damage due to FIB milling and its influence on the mechanical properties has to be characterized employing TEM and Auger electron spectroscopy (AES).

The new findings are summarized after the individual publications at the end of this thesis.

References

[1] J. P. Hirth and J. Lothe, *Theory of Dislocations* (Wiley, New York, 1982).

[2] N. J. Petch, J. Iron Steel 1953; 174: 25.

[3] E. O. Hall, Proc. R. Soc. Lond. 1951; B64: 747.

[4] G. Saada, Mater. Sci. Eng. A 2005; 400-401: 146.

[5] R. Armstrong, R. M. Douthwaite, I. Codd, and N. J. Petch, Phil. Mag. 1962; 7: 45.

[6] L. H. Friedman and D. C. Chrzan, Phil. Mag. A 1998; 77: 1185.

[7] A. J. E. Foreman, Phil. Mag. 1967; 15: 1011.

[8] E. Arzt, Acta Mater. 1998; 46: 5611.

[9] N. A. Fleck, G. M. Muller, M. F. Ashby, and J. W. Hutchinson, Acta Met. Mater. 1994; 42: 475.

[10] J. S. Stölken and A. G. Evans, Acta Mater. 1998; 46: 5109.

[11] Q. Ma and D. R. Clarke, J. Mater. Res. 1995; 10: 853.

[12] W. J. Poole, M. F. Ashby, and N. A. Fleck, Scripta Mater. 1996; 34: 559.

[13] W. D. Nix and H. Gao, J. Mech. Phys. Solids 1998; 46: 411.

[14] M. F. Ashby, Phil. Mag. A 1970; 21: 399.

[15] N. A. Fleck and J. W. Hutchinson, J. Mech. Phys. Solids 2001; 49: 2245.

[16] H. Gao, Y. Huang, W. D. Nix, and J. W. Hutchinson, J. Mech. Phys. Solids 1999; 47: 1239.

[17] M. D. Uchic, D. M. Dimiduk, J. N. Florando, and W. D. Nix, Science 2004; 305: 986.

[18] D. M. Dimiduk, M. D. Uchic, and T. A. Parthasarathy, Acta Mater. 2005; 53: 4065.

[19] J. R. Greer, W. C. Oliver, and W. D. Nix, Acta Mater. 2005; 53: 1821.

[20] J. R. Greer, W. C. Oliver, and W. D. Nix, Acta Mater. 2006; 54: 1705 [Corrigendum].

[21] C. A. Volkert and E. T. Lilleodden, Phil. Mag. 2006; 86: 5567.

[22] D. Kiener, C. Motz, T. Schöberl, M. Jenko, and G. Dehm, Adv. Eng. Mater. 2006; 8: 1119.

[23] B. Moser, K. Wasmer, L. Barbieri, and J. Michler, J. Mater. Res. 2007; 22: 1004.

[24] C. P. Frick, S. Orso, and E. Arzt, Acta Mater. 2007; 55: 3845.

[25] W. D. Nix, J. R. Greer, G. Feng, and E. T. Lilleodden, Thin Solid Films 2007; 515: 3152.

[26] T. A. Parthasarathy, S. I. Rao, D. M. Dimiduk, M. D. Uchic, and D. R. Trinkle, Scripta Mater. 2007; 56: 313.

[27] A. H. W. Ngan, L. Zuo, and P. C. Wo, Scripta Mater. 2006; 54: 589.

[28] J. Gil Sevillano, I. Ocana Arizcorreta, and L. P. Kubin, Mater. Sci. Eng. A 2001; 309-310: 393.

[29] H. Zhang, B. E. Schuster, Q. Wei, and K. T. Ramesh, Scripta Mater. 2006; 54: 181.

[30] D. Raabe, D. Ma, and F. Roters, Acta Mater. 2007; 55: 4567.

[31] Y. S. Choi, M. D. Uchic, T. A. Parthasarathy, and D. M. Dimiduk, Scripta Mater. 2007; 57: 849.

[32] L. Zuo and A. H. W. Ngan, Phil. Mag. Lett. 2006; 86: 355.

[33] H. Tang, K. W. Schwarz, and H. D. Espinosa, Acta Mater. 2007; 55: 16071616.

[34] L. A. Zepeda-Ruiz, B. Sadigh, J. Biener, A. M. Hodge, and A. V. Hamza, App. Phys. Lett. 2007; 91: 1.

[35] V. S. Deshpande, A. Needleman, and E. Van der Giessen, J. Mech. Phys. Solids 2005; 53: 2661.

[36] R. Maaß, S. Van Petegem, H. Van Swygenhoven, P. M. Derlet, C. A. Volkert, and D. Grolimund, Phys. Rev. Lett. 2007.

[37] D. Kiener, C. Motz, and G. Dehm, manuscript under preparation.

[38] D. Kiener, C. Motz, M. Rester, and G. Dehm, Mater. Sci. Eng. A 2007; 459: 262.

[39] H. Bei, S. Shim, E. P. George, M. K. Miller, E. G. Herbert, and G. M. Pharr, Scripta Mater. 2007; 57: 397.

[40] H. Bei, S. Shim, M. K. Miller, G. M. Pharr, and E. P. George, App. Phys. Lett. 2007; 91: 1.

II Determining Mechanical Properties of Copper at the Micron Scale (Publication A)

D. Kiener, C. Motz, T. Schöberl, M. Jenko, and G. Dehm

Advanced Engineering Materials (2006) Vol. 8; Issue 11; 1119-1125.

ABSTRACT

Using a focused ion beam workstation, micron-sized bending and compression samples were fabricated from a pure copper single crystal. Loading of the miniaturized specimens was performed either *ex-situ* or *in-situ* in a scanning electron microscope. The bending and compression experiments exhibited a strong size effect on the flow stress of copper, reaching values in the order of 1 GPa for the smallest test structures. Conventional strain gradient plasticity approaches are not capable of explaining this behaviour. The surface damage introduced by Ga^+ ion implantation during focused ion beam preparation was investigated using Auger electron spectroscopy and its consequence on the mechanical response of the miniaturized test samples is addressed.

1. Introduction

The ongoing trend in miniaturization of micro-electro-mechanical systems (MEMS), medical devices (e.g. STENTs), and microelectronic devices leads to structural elements with one or more dimensions in the range of a few tens of nanometres to a few hundred microns. This requires novel techniques to determine the mechanical properties of materials at this small length scale.

The most frequently used method is the nanoindentation technique [1-4]. It is usually straightforward to apply to a wide range of materials, is essentially non-destructive, and material properties like hardness and reduced elastic modulus can be deduced from such experiments. With some additional efforts attributes like yield strength, creep behaviour and fracture toughness can be determined. However, several problems arise when performing indentation experiments. The shape of the indenter tip is usually not exactly known, but it strongly influences the actual contact area and therefore the calculated values of hardness and stiffness at very shallow indentation depths. Furthermore, one has to deal with a complex stress and strain field beneath the indenter tip, which makes it difficult to directly compare indentation data to material properties obtained from tension, compression or bending tests, which all possess a well defined stress and strain distribution.

To overcome the problems of indentation tests, efforts were undertaken to adapt conventional material test methods to micron-sized samples. Fleck et al. [5] performed torsion tests on copper wires and reported increasing torsional resistance when the wire diameter was reduced from 170 to 12 µm. Stölken and Evans [6] performed bending tests on nickel foils and observed increasing bending strength as the foil thickness decreased from 50 to 12.5 µm. This increase in yield strength and flow stress was attributed to an increasing strain gradient with decreasing specimen size [5, 7]. Weiss et al. [8] performed tension experiments on free standing thin Cu foils and wires and reported a strong influence of the sample thickness on the fracture strain, with thinner samples exhibiting reduced plasticity.

In recent times, compression tests on micron-sized samples prepared with the focused ion beam (FIB) technique have been reported in the literature [9-12]. For a variety of materials a strong size effect in flow stress was found, if the diameter of the so-called “micro-pillars” was reduced from 10 to 0.2 µm. This size effect

obtained by micro-compression tests can not be explained by strain gradient plasticity approaches. To elucidate the influence of a strain gradient on the deformation behaviour at the micrometer scale, micron-sized compression (no strain gradient present) and bending (strain gradient present) tests were performed. The results are compared and discussed in this paper. Furthermore, quantitative Auger electron spectroscopy (AES) was performed on the damaged zone at the surface of FIB designed miniaturized samples. The results obtained will be used in the interpretation of the mechanical tests.

2. Experimental procedure

All mechanical tests were performed on copper single crystals with a <110>{111} orientation. In a first step the single crystal was cut with a diamond saw to obtain a {111} sample surface, with a {110} side face along a <112> edge for the micro-compression samples and a {112} side face along a <110> edge for the micro-bending samples, respectively. Subsequently, both perpendicular planes were electro-polished to remove the deformation layer produced by the cutting process. Additionally, the side faces were carefully polished using an alumina suspension with a grain size of 1 µm in order to achieve a sharp edge to minimize the milling time with the FIB. The deformation layer due to the final polishing step had a thickness of about 5 µm and was removed by FIB milling (LEO XB 1540) with 30 keV Ga^+ ions. This procedure produces a specimen with a sharp edge between the {111} top surface and the {110} or {112} side surface. Micron-sized bending and compression samples were prepared along this edge, with the correlation between the specimen orientation and the crystal directions schematically shown in Fig. 1. The orientation of the specimen with respect to the copper substrate is also indicated in Fig. 1.

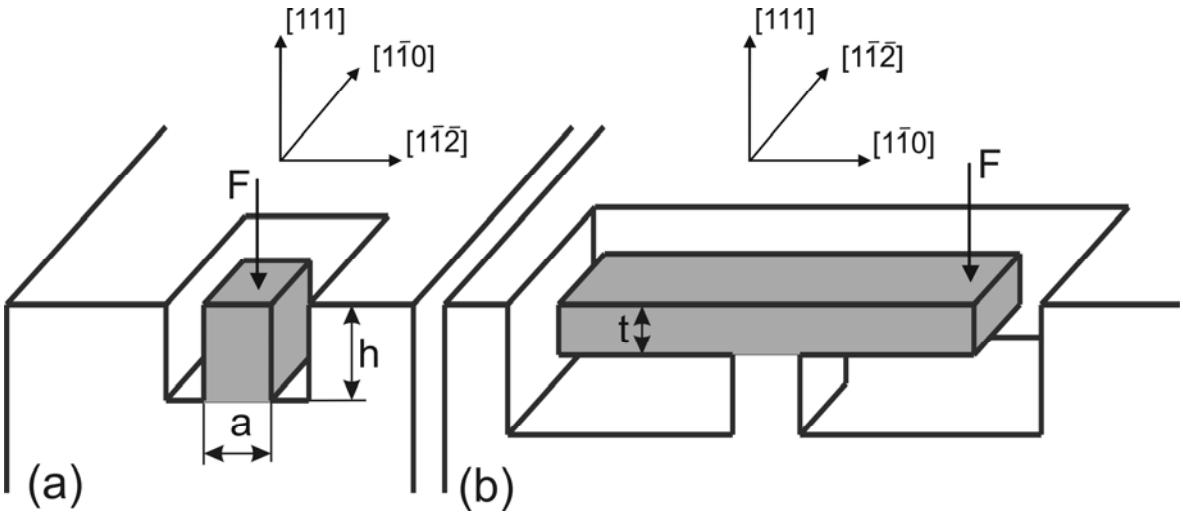

Fig. 1: Correlation between the sample dimensions and the crystal directions for (a) micro-compression samples, (b) micro-bending beams, and the corresponding orientation of the copper single crystal.

2.1 Fabrication of the micro-compression samples

For the compression samples, an 800 nm thick TiN coating was sputter-deposited on the single crystal copper sample to protect the surface from ion damage during the first milling step. A pre-form of the pillar with a side length a = 10 µm and a height h = 15 µm was FIB milled under perpendicular ion impact, using an ion current of 1 nA. Fig. 2a shows the plan-view FIB image of a pre-form. The bright contrast fringe around the pillar indicates the broadening of the column with depth, which is typical of this milling setup. Depending on the material the taper can vary between 0.5° for fluorine assisted etching of silicon to several degrees for refractory metals like tungsten. This broadening can be compensated for by tilting the sample a few degrees [13]. Another possibility, which we employed in this study, is to tilt the sample by 54° and to perform milling using grazing incident ions. The benefit of this method is that the side planes are parallel to the specimen axis and no tapering occurs. Slight deviations from the rectangular shape occurred for the largest samples investigated as a consequence of the milling procedure. However, this can be taken into account in the evaluation of the stress-strain data, as the deviations remain constant over the whole height of the specimen.

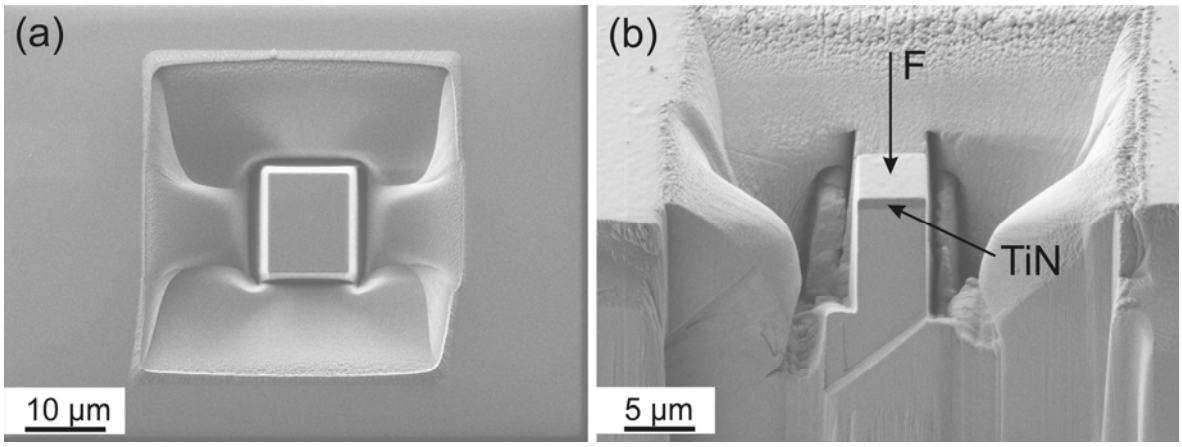

Fig. 2: FIB-fabricated micro-compression samples: (a) FIB image of the top view of a pre-form with a side length of 10 µm, milled with perpendicular ion impact. (b) Tilted SEM view of a pillar after the final milling with grazing ion impact. The TiN top layer is marked by an arrow.

For the final milling step an ion current of 100 pA was used to reduce the ion damage. Fig. 2b shows a tilted scanning electron microscope (SEM) image of a pillar along the sample edge with a side length *a* of 5 µm after the final milling.
For the present work square-shaped pillars with nominal side lengths *a* of 8, 5, 3, 2, and 1 µm were fabricated. The aspect ratio of the micro-compression samples was in the range of 1.5 to 2 as suggested by Zhang et al. [14].

2.2 Loading of the micro-compression samples

The compression tests were carried out *in-situ* using a nanoindenter (ASMEC UNAT) that was mounted inside the SEM chamber (LEO Stereoscan 440). This setup allows accurate positioning of the sample and indenter due to the superior resolution of *in-situ* SEM imaging compared to nanoindenters equipped with a conventional optical microscope. Furthermore, it is possible to record micrographs during the loading experiment. Instead of a common sharp indenter a flat punch, cut with the FIB from a tungsten needle with approximately 100 µm diameter, was used. The size of the rectangular flat punch was 10x10 μm^2 and thus larger than the side lengths of the compression samples. During compression testing of the micro-pillars force and displacement were recorded.

2.3 Fabrication of the micro-bending beams

In the vicinity of the <110> edge a free standing lamella with a length of about 100 µm, 50 µm in height and 15 µm in width was milled using Ga^+ ion currents of 10 - 20 nA. After tilting the sample by 90° the “T-shape” of a double bending beam was produced. Fig. 3a shows two micron-sized bending beams after a final Ga^+ polishing with ion currents decreasing from 1 nA to 200 pA. This reduction of the milling current was chosen in order to minimize the Ga^+ implantation in the surface of the test structures. Bending beams with thicknesses of t = 7.5, 5, 3.5, 2.5, and 1 µm were prepared. The widths ranged between w = 2.5 and 7.5 µm, and the bending lengths were l_b = 20 to 25 µm. Further details are reported in [15].

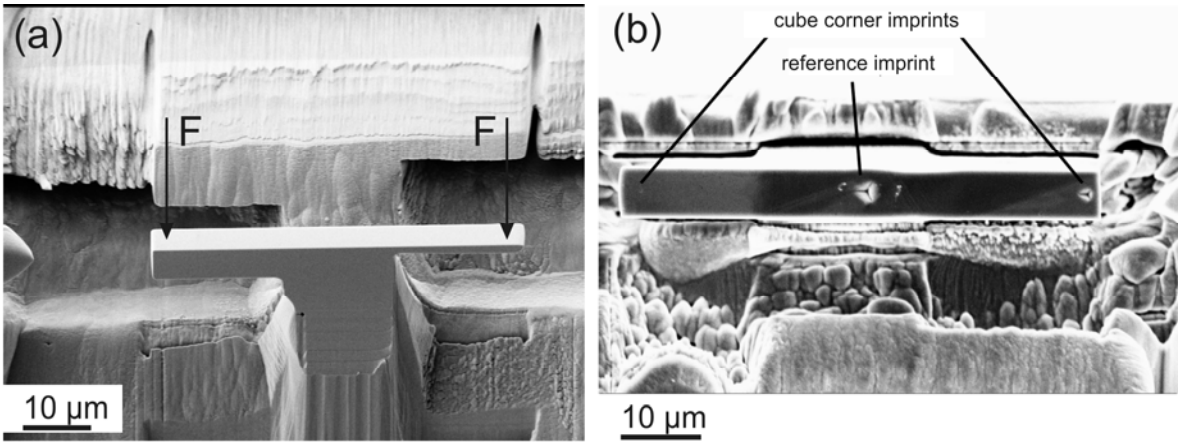

Fig. 3: (a) Micro-bending beams fabricated using the FIB-technique. First a free-standing lamella in the vicinity of the sample edge is milled, subsequently bending beams were cut out of this lamella. (b) SEM top view of the beams after bending reveals the imprints caused by the cube corner tip. See text for details.

2.4 Loading of the micro-bending beams

The micro-bending beams were loaded with a nanoindenter (Hysitron Triboscope) attached to an atomic force microscope (Digital Instruments DI 3100). This setup provides the possibility to scan the sample surface with the same cube corner tip, which is subsequently used for the loading experiment. All micro-bending beams were imaged prior to loading, which assured an accurate positioning of the indenter on the bending beam. During the experiments force and displacement were recorded. Finally, to differentiate between displacements contributing to

bending and indentation a reference imprint was made at the centre of the beam support, to correct for the additional displacement caused by the imprinting of the indenter into the bending beam. The correct positioning of the indenter tip was verified after testing by measuring the position of the residual imprint in a SEM (see Fig. 3b).

2.5 Auger electron spectroscopy (AES)

In order to analyse the damage induced by the Ga^+ ion bombardment, pure copper specimens were electro-polished and subsequently damaged by perpendicular ion impact at different ion currents. Areas of 50x50 μm^2 were sputtered by Ga^+ ions with a kinetic energy of 30 keV for 1000 s and ion currents of 0.5 nA, 1 nA and 10 nA, respectively. The employed dual-beam workstation allows selection of the milling regions in the SEM view, thus avoiding any unwanted Ga^+ ion implantation. From the damaged regions the surface concentration of Ga was measured using AES.

The investigations were carried out using a VG-Scientific Microlab 310-F field emission instrument with a thermally assisted Schottky field emission source at an accelerating voltage of 10 kV. The use of a field emission source in conjunction with an efficient electron spectrometer (energy resolution below 2 %) enabled operation at a beam diameter of 10 nm at a beam current of 10 nA. Imaging of the Ga implanted regions was performed using secondary electrons. This allowed accurate positioning of the region of interest for the AES measurement. AES depth profiles were obtained by subsequent Ar^+ sputtering at 3 keV, resulting in a sputtering rate of 0.017 nm per second.

3. Results

3.1 Micro-compression tests

Fig. 4a shows the force - displacement response of a micro-pillar with a cross-section of 3x3 μm^2. The curve exhibits the typical behaviour of a compression sample with no peak force but a constant rise of the force due to work hardening and deformation of the specimen. In order to calculate true stress versus true strain curves, we assume perfect cuboids and the volume of the pillar being

conserved during uniaxial compression. The side length and height were determined in the SEM prior to testing with an accuracy of ±0.1 µm, the initial cross-sectional area was measured with an accuracy better than ±0.1 µm^2. The procedure used to analyse the force - displacement data is similar to that described by Greer et al. [9].

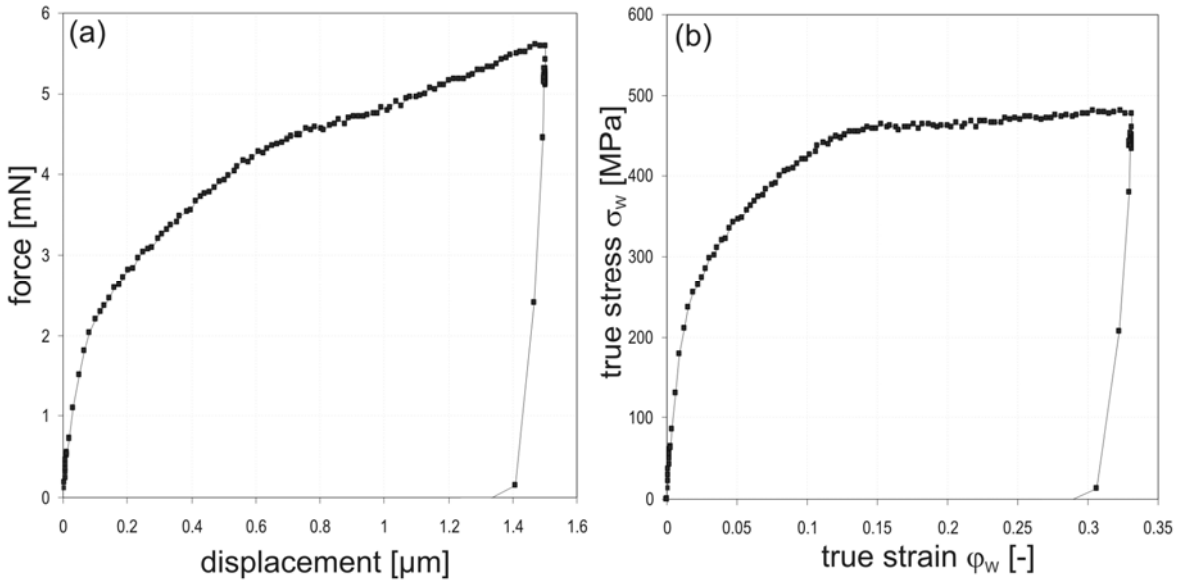

Fig. 4: (a) Recorded force - displacement response of a 3x3 µm^2 micro-compression sample and (b) the calculated true stress - true strain curve.

3.2 Micro-bending samples

Fig. 5 shows a typical force versus displacement response of a micro-bending beam with a thickness of 5 µm. The initial rise with increasing force is followed by a force plateau, which was typical for all tested beams. An accurate determination of the yield force F_y, which is the force where the first plastification occurs, is difficult due to the slight non-linear force response in the initial deformation regime. Thus, the plateau force F_{max} was used for the evaluation of the flow stress. It is assumed that in the force plateau regime the deformed region is fully plastic and no significant work hardening occurred at this stage.

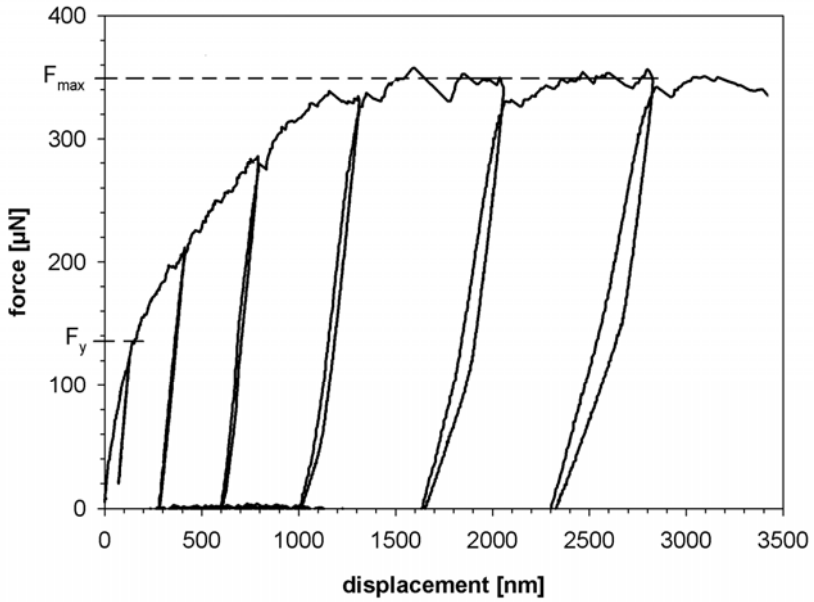

Fig. 5: Force - displacement response of a micro-beam with *w* = 5 µm, *t* = 5 µm and l_b = 20 µm.

Applying the moment of equilibrium one can calculate the corresponding flow stress σ_f with:

$$\sigma_f = 4\frac{F_{\max} l_b}{w \cdot t^2}, \tag{II.1}$$

where F_{max} is the maximum force, w the beam width, t the beam thickness and l_b is the bending length determined after loading using the SEM (e.g. see Fig. 3b). Further details are reported in [15].

3.3 Comparing micro-bending and micro-compression results

For the bending beams the average strain in the plastically deformed region is in the order of 0.2 to 0.25 when the force plateau is reached. All tested compression pillars reached a stress plateau at a true strain φ_W of about 0.1 and were compressed to values larger than 0.25. Therefore, to compare the data obtained from the bending and compression experiments, the flow stress values at a true strain φ_W = 0.2 were taken. All flow stress results are summarized in Fig. 6. Due to the cross-over in stress from tension to compression at the neutral axis of the bending beams only half the beam thickness is considered in Fig. 6.

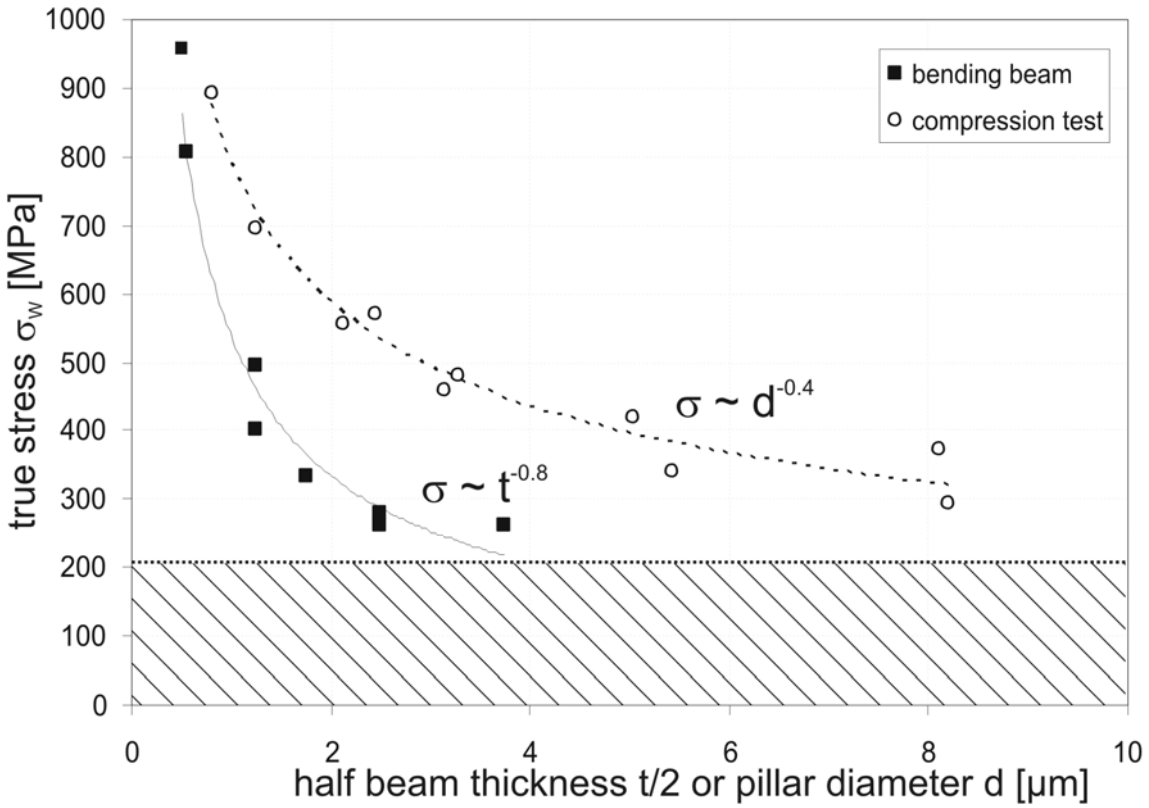

Fig. 6: Dependence of the flow stress on the sample dimension for micro-bending and micro-compression specimens at a true strain φ_W = 0.2. *t* is the bending beam thickness, and d the equivalent circle diameter of the nearly square shaped pillars. The dashed line indicates the bulk flow stress at 20 % tensile strain for high purity Cu with a grain size of 10 µm [16].

Both specimen types show a pronounced rise of the flow stress with decreasing sample dimension. The maximum stresses exceed 900 MPa. Even the largest samples show flow stresses of more than 250 MPa. For comparison, the flow stress of high purity bulk Cu with a grain size of 10 µm determined in a conventional tensile test is indicated in Fig. 6 [16]. This grain size corresponds to the largest investigated dimensions of our micron-sized samples. The value of 210 MPa can be regarded as an upper limit for Cu single crystals, even lower values are reported in the literature [17]. When assuming a power law for the observed size effect in Fig. 6, the exponents are -0.8 for the micro-bending samples and -0.4 for the micro-compression tests with the correlation coefficient being 0.97 and 0.98, respectively.

3.4 Auger electron spectroscopy measurements

It is known that surface layers (e.g. oxide and/or passivation layers) alter dislocation mechanisms compared to crystals with a “free” surface [18], thus influencing the mechanical properties. Similarly, Ga^+ ion bombardment during the FIB preparation is expected to cause a modification of the surface structure, however little is known about the damage. Most of the data reported in the literature concerns transmission electron microscopy (TEM) investigations of the thickness of the amorphous layer caused by Ga implantation [13, 19]. The thickness of this layer is in the order of several tens of nanometres, depending mainly on the ion energy, the material, the incident angle of the ions and whether a protection layer was used or not. Since the FIB has been used in the semiconductor industry for several years as a fabrication and repairing tool before it entered the general material science community some years ago, these investigations focus mainly on Si and partly GaAs. Marien et al. [20] performed TEM investigations of a Cu metallization layer, prepared using Ga^+ ions, and reported strong strain contrast variations within single grains. The authors concluded that these variations originate from defects or defect agglomerations causing strain contrast in the film.

For a first estimation of the penetration depth of the Ga^+ ions the SRIM (Stopping Range of Ions in Matter) code [21] may be used. This delivers a penetration depth for Ga^+ ion bombardment with a kinetic energy of 30 keV in copper of about 30 nm for perpendicular and about 18 nm for grazing incident ions. To verify this simulation data AES investigations were performed on different FIB prepared copper surfaces. The measured Ga concentrations at the surface are given in Table 1. It can be seen that lower milling currents reduce the surface concentration. This effect is caused by a lower ion dose.

Table 1: Surface concentration of Ga for different milling currents. The milling time was kept constant at 1000 s.

Milling current [nA]	0.5	1	10
Surface concentration of Ga [at%]	5.5±0.6	8.7±0.9	18.6±1.9

Apart from the obtained Ga surface concentration listed in Table 1 a depth profile of the Ga concentration was measured for a sample that was exposed to the 10 nA ion current. The result is shown in Fig. 7.

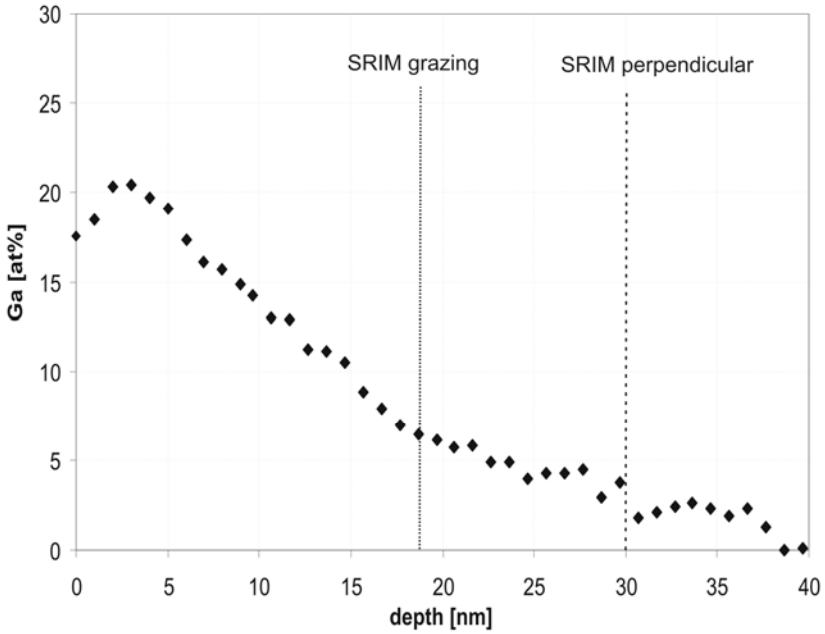

Fig. 7: AES depth profile of the Ga concentration for a copper sample damaged by perpendicular Ga^+ ion bombardment at 30 keV kinetic energy and an ion current of 10 nA. The maximum concentration of about 20 at% Ga near the surface decreases to values below 1 at% over a depth of about 35 nm. SRIM predictions for perpendicular and grazing incident are 30 nm and 18 nm, respectively.

A maximum Ga concentration of 20 at% was found about 3 nm beneath the initial sample surface. However, only at a depth of more than 35 nm does the Ga concentration decrease below 1 at%. The depth profile is in agreement with the SRIM calculations.

4. Discussion

4.1 Mechanical properties

A popular explanation for size effects in mechanical properties is strain gradient plasticity [4, 5, 22, 23]. Strain gradient plasticity models may be applicable for the micro-bending samples, as there is a size dependent strain gradient present in the

deformation field. However, as has been shown by Motz et al. [15], the predicted rise in flow stress caused by the strain gradient cannot explain the experimentally observed values. In the present case of the micro-compression samples no strain gradient is present. Thus, the strain gradient plasticity model can be neglected, indicating that other constraints must impose the observed size effects. Several alternative explanations are currently discussed in the literature. The three most promising models are (i) dislocation starvation [9], (ii) dislocation nucleation [24], and (iii) dislocation pile-up [25]:

(i) dislocation starvation

When decreasing the size of the specimen, one automatically increases the surface to volume ratio. This is obvious for the tested pillars, as the surface to volume ratio equals the inverse pillar diameter plus a constant, which depends on the exact geometry. In the initial deformation existing dislocations leave the micron-sized crystal before they can multiply by cross-slip or dislocation interactions. Consequently, the dislocation density decreases through out the deformation process, as their ability to multiply is reduced. Further plastic deformation requires therefore high stress levels for the repeated generation of new dislocations. As a consequence, the deformation behaviour may finally become comparable to whisker crystals. Up to now no mathematical description of this model is available in the literature. Furthermore, it remains questionable how many dislocations are initially present and glissile in such micron-sized samples with a Burgers vector in the direction of slip. Assuming an initial dislocation density of $\rho_d = 10^{10}$ m^{-2} [26], only a single dislocation would be present in a volume of 10 µm^3.

(ii) dislocation nucleation

Dislocation sources are required to generate the dislocations necessary for plastic slip. If the number of dislocation sources is limited (e.g. in small sample volumes or single crystal whiskers), sources which are either located on unfavourable glide systems or of unfavourable size have to be activated. This leads to high flow stresses. Von Blanckenhagen et al. [24] showed, that the critical stress to bow out a dislocation segment for a given source size is given by

$$\tau_{source} = \frac{\mu b}{2\pi} \cdot \frac{1}{s} \cdot \ln\left(\frac{\alpha s}{b}\right), \qquad \text{(II.2)}$$

where μ is the shear modulus, *b* the Burgers vector, *s* the source size and α a numerical constant. It was found that the optimum source size, in terms of operating the source at low stress levels, is between 1/3 and 1/4 of the limiting dimension, i.e. pillar diameter or half the beam thickness. Thus, this model predicts an inverse scaling of the flow stress with the pillar diameter or the beam thickness for miniaturized test samples.

(iii) dislocation pile-up

Obstacles that can cause dislocation pile-ups include: Interfaces, surface layers induced by FIB milling, passivation layers or surface oxides, but also regions of high internal stress gradients like across the neutral axis in a bending beam. Due to the limited number of dislocation sources as the specimen size decreases, the dislocations are concentrated on few glide systems. Consequently, dislocation pile-ups will affect the dislocation sources by strong back stresses. Friedman and Chrzan [27] considered a double-ended pile-up and incorporated a critical source strength in their model. The necessary stress to operate a dislocation source was found to be

$$\sigma_A = \left(\frac{4\mu b \sigma_i}{\pi d} + \sigma_S^2 \right)^{1/2}, \qquad \text{(II.3)}$$

where σ_A is the applied stress, μ the shear modulus, σ_i the strength of the interface, *d* the critical length scale, and σ_S the source strength. The back-stress resulting from the dislocation pile-up leads to an increased flow stress scaling inverse with the square root of the critical length scale [27-29].

Quantitative measurements from the micro-bending tests agree with the model of Sedlacek [25], which considers the increase in flow stress due to the pile-up of dislocations at the neutral axis of a bending beam (see Motz et al. [15]). Therefore, half of the beam thickness was applied as the characteristic length scale for the bending beams in Fig. 6.

However, up to now all models suffer from a lack in experimental verification of the proposed deformation mechanisms. Another aspect that has not been fully considered and analysed is the possible influence of damage, introduced by FIB preparation, on the mechanical response. Although being a well known problem, previous examinations [9-11] have often neglected the effect of FIB damage.

4.2 FIB induced surface damage

From the AES measurements it is clear that under unfavourable conditions the Ga concentration at FIB prepared surfaces can be as high as 20 at% (at 3 nm) with a maximum depth of about 35 nm. For smaller ion currents and grazing incident, which is the common milling condition for the final polishing step, the Ga contamination is expected to be smaller. However, the general influence on the mechanical properties is still unclear.

If the damaged surface acts as a barrier for dislocations, it can influence the mechanical response of the sample. Such a surface may hinder dislocations from leaving the crystal and cause pile-up at the surface. If the deformed volume is large, there will be many dislocation sources and the emitted dislocations will be uniformly distributed over the sample volume. However, if the deformed volume is small only a few dislocation sources are available and the deformation is concentrated on a few slip systems. If there is a surface that causes dislocation pile-ups, the back stresses may even deactivate dislocation sources. Thus, a higher stress level is needed to activate other sources or to break the surface layer. This mechanism may dominate or at least contribute to the observed size effect in flow stress. Similar effects are reported for submicron thin metal films on substrates, where a surface passivation layer doubles the flow stress compared to the unpassivated films [30, 31]. Furthermore, one may have to consider internal stresses caused by the ion implantation [32] and for very small samples (100 nm and below) the mechanical properties of the damaged surface itself will play an important role. The higher exponent of -0.8 for the micro-bending specimen compared to -0.4 for the micro-compression samples may be explained by the additional pile-up at the neutral axis (stress sign reversal) and the strain gradient present in these specimens.

It was shown that a high concentration of Ga contamination can occur on FIB prepared surfaces. The influence of this modified surface on the mechanical properties is not yet clear. However, it is not appropriate to neglect this, especially if the sample size reaches submicron dimensions. Further investigations are being performed on the structure and the mechanical properties of this damaged surface.

5. Conclusions

Micro-bending and micro-compression experiments were conducted on single crystal {111} oriented copper specimens. Both kinds of experiments exhibited a strong size effect on the flow stress with decreasing sample size. The exponents of a power-law fitted to the experimental data were found to be -0.8 for the micro-bending specimen and -0.4 for the micro-compression specimen. Conventional strain gradient plasticity approaches are not capable of explaining this behaviour. Models proposed in the literature dealing with dislocation starvation, dislocation nucleation, and dislocation pile-up were discussed. The damaged surface due to the Ga^+ ion bombardment during FIB preparation was investigated using Auger electron spectroscopy. The substantial depth of implantation up to 35 nm and Ga content reaching 20 at% may cause dislocation pile-ups, which in turn would alter the deformation behaviour expected compared to undamaged Cu.

References

[1] W. C. Oliver and G. M. Pharr, J. Mater. Res. 1992; 7: 1564.

[2] J. G. Swadener and G. M. Pharr, Phil. Mag. A 2001; 81: 447.

[3] A. E. Giannakopoulos and S. Suresh, Scripta Mater. 1999; 40: 1191.

[4] W. D. Nix and H. Gao, J. Mech. Phys. Solids 1998; 46: 411.

[5] N. A. Fleck, G. M. Muller, M. F. Ashby, and J. W. Hutchinson, Acta Met. Mater. 1994; 42: 475.

[6] J. S. Stölken and A. G. Evans, Acta Mater. 1998; 46: 5109.

[7] N. A. Fleck and J. W. Hutchinson, J. Mech. Phys. Solids 2001; 49: 2245.

[8] B. Weiss, V. Groger, G. Khatibi, A. Kotas, P. Zimprich, R. Stickler, and B. Zagar, Sensors Actuators A 2002; 99: 172.

[9] J. R. Greer, W. C. Oliver, and W. D. Nix, Acta Mater. 2005; 53: 1821.

[10] D. M. Dimiduk, M. D. Uchic, and T. A. Parthasarathy, Acta Mater. 2005; 53: 4065.

[11] M. D. Uchic, D. M. Dimiduk, J. N. Florando, and W. D. Nix, Science 2004; 305: 986.

[12] C. A. Volkert and E. T. Lilleodden, Phil. Mag. 2006; 86: 5567.

[13] H.-J. Engelmann, Prakt. Met. 2003; 40: 163.

[14] H. Zhang, B. E. Schuster, Q. Wei, and K. T. Ramesh, Scripta Mater. 2006; 54: 181.

[15] C. Motz, T. Schöberl, and R. Pippan, Acta Mater. 2005; 53: 4269.

[16] S. Scheriau, Diploma Thesis, Institute of Metal Physics, University of Leoben 2006.

[17] G. Gottstein, *Physikalische Grundlagen der Materialkunde* (Springer, Berlin, 2001).

[18] W. W. Gerberich, S. K. Venkataraman, H. Huang, S. E. Harvey, and D. L. Kohlstedt, Acta Met. Mater. 1995; 43: 1569.

[19] Z. Wang, T. Kato, T. Hirayama, N. Kato, K. Sasaki, and H. Saka, App. Surf. Sci. 2005; 241: 80.

[20] J. Marien, J. M. Plitzko, R. Spolenak, R.-M. Keller, and J. Mayer, J Microscopy 1998; 194: 71.

[21] J. F. Ziegler, J. P. Biersack, and U. Littmark, *The Stopping Range of Ions in Matter* (Pergamon Press, New York, 1985).

[22] H. Gao, Y. Huang, W. D. Nix, and J. W. Hutchinson, J. Mech. Phys. Solids 1999; 47: 1239.

[23] H. Mughrabi, Mater. Sci. Eng. A 2004; 387-389: 209.

[24] B. von Blanckenhagen, P. Gumbsch, and E. Arzt, Phil. Mag. Lett. 2003; 83: 1.

[25] R. Sedlacek, Mater. Sci. Eng. A 2005; 393: 387.

[26] D. Hull and D. Bacon, *Introduction to Dislocations* (Elsevier Butterworth-Heinemann, Oxford, 2004).

[27] L. H. Friedman and D. C. Chrzan, Phil. Mag. A 1998; 77: 1185.

[28] E. O. Hall, Proc. R. Soc. Lond. 1951; B64: 747.

[29] N. J. Petch, J. Iron Steel 1953; 174: 25.

[30] E. Arzt, G. Dehm, P. Gumbsch, O. Kraft, and D. Weiss, Prog. Mater. Sci. 2001; 46: 283.

[31] S. P. Baker, A. Kretschmann, and E. Arzt, Acta Mater. 2001; 49: 2145.

[32] N. Kalyanasundaram, M. C. Moore, J. B. Freund, and H. T. Johnson, Acta Mater. 2006; 54: 483.

III Influence of external and internal length scale on the flow stress of copper (Publication B)

D. Kiener, M. Rester, S. Scheriau, B. Yang, R. Pippan, and G. Dehm

International Journal of Materials Research (2007) Vol. 98; Issue 11; in press.

Abstract

The flow stress of bulk specimens is known to depend on the microstructure. With a reduction of specimen dimensions into the micrometer and nanometer regime, specimen size-effects also influence the mechanical properties. We characterized the size-dependent flow stress of copper over more than three orders of magnitude, starting from several tens of micrometers down to a few tens of nanometers. For this purpose nanoindentation, micro-compression, and tensile testing experiments were performed. Additionally, different grain sizes were generated by severe plastic deformation. The observed increase in flow stress with reduced critical dimension is discussed with respect to the different stress states and microstructures present in the reported experiments. The mechanism controlling deformation changes from dislocation pile-up for critical dimensions > 1 μm via a transition regime (1 μm > critical dimensions > 100 nm) to dislocation nucleation for critical dimensions < 100 nm.

1. Introduction

With the ongoing miniaturization, the lateral dimensions of structural components are reduced in a way that continuum concepts using material properties of bulk specimen fail to describe the mechanical properties. Structural features like grain boundaries are well known to influence the stress–strain behavior, which can be understood, for example, in terms of the Hall–Petch effect [1, 2]. A comprehensive treatment of the Hall–Petch behavior of bulk Cu can be found in [3, 4]. On the other hand, the finite sample size itself also influences the material properties [5]. This requires reliable methods, able to probe a representative volume in order to characterize mechanical properties in the micrometer and sub-micrometer regime. Four methods, nanoindendation, micro-compression, fiber-tension, and severe plastic deformation (SPD), were applied to high purity Cu.

Indentation techniques [6, 7] are frequently used to determine the local mechanical properties of a large variety of materials. Nanoindenter systems offer a very high resolution in measuring penetration depth and load [8]. The local positioning is accomplished using either an optical or a scanning probe microscopy system. The method can be applied to every polished flat surface and works almost non-destructively. Nevertheless, there are several complications when trying to extract mechanical properties such as yield stress and hardening exponent from indentation data [9, 10]. This is mainly a consequence of the complex stress and strain state beneath the indenter and the indentation size effect (ISE) [6, 11].

The experimental setup typically used for micro-compression testing [12, 13] is a nanoindenter system equipped with a flat punch instead of a sharp indenter. Therefore, many advantages of indentation techniques, like high resolution in the determination of load and displacement, hold true for column testing as well. A disadvantage lies in the tedious sample preparation, which usually requires a focussed ion beam (FIB) workstation. Nevertheless, it is possible to mill almost every material using a FIB. A benefit of this method lies in the nominally uniaxial stress state, making the flow stress evaluation from micro-compression tests much simpler than from indentation data.

Fiber tensile testing requires the preparation of the sample in the form of a fiber, which can become quite difficult, especially if electrochemical methods are not applicable. As with the micro-compression testing, the subsequent data treatment

to obtain, for example, the flow stress at a certain strain is mathematically straightforward. However, the accuracy of cross-sectional dimensions over the gauge length and the large gauge length in the order of millimeters compared to an elongation to fracture in the order of micrometers are challenging.

SPD in combination with thermal heat treatment offers a way for a significant grain refinement in bulk crystalline metals and alloys, leading to a microstructure with enhanced strength and hardness. The processing technique applied in this study was high pressure torsion (HPT), where the deformation takes place by simple shear [14]. The applied high hydrostatic pressure prevents crack generation, which allows obtaining very large strains of several thousand percent, even in brittle materials. HPT provides millimeter sized specimen with well-defined grain sizes down to the submicrometer regime, which can be mechanically tested using standardized methods.

With this approach, critical dimensions ranging from several tens of micrometers down to only a few tens of nanometers can be analyzed. The first three methods are capable of probing small volumes; while SPD offers the possibility to probe macroscopic samples with various grain sizes. Table 1 compares the load–displacement regime, the corresponding resolution, and the probed sample volume for the experimental setups used in the current study.

Table 1: Load–displacement regimes and corresponding resolution for the employed setups. Additionally, the probed volume is estimated.

Method	Max. load (mN)	Load res. (µN)	Max. displ. (µm)	Displ. res. (nm)	Probed volume (μm^3)
Nanoindentation*	12	1	5	0.1	$> 10^{-4}$
Micro-compression	350	50	50	10	$1 – 10^3$
Fiber-tensile testing	$2 \cdot 10^3$	10	$3 \cdot 10^3$	70	$10^5 – 10^7$
SPD tensile testing	10^7	10^5	$3 \cdot 10^3$	100	10^{10}

* The volume probed by nanoindentation can be calculated from the plastic zone, as suggested in [6].

Furthermore, deformation experiments *in-situ* in a scanning electron microscope (SEM) give insight in the deformation mechanisms.

The aim of this work is twofold: Firstly, to examine the influence of the microstructure on the size-dependent flow stress by comparing polycrystalline and single crystalline Cu, and secondly to compare the influence of a strain gradient versus a nominally uniaxial stress state on the flow stress.

2. Deformation Techniques

2.1 Nanoindentation

A single crystal of Cu with a <111> surface normal was cut with a wire saw and prepared by wet grinding and mechanical polishing. A final electro-polishing step was applied to achieve a surface suitable for nanoindentation and to remove any existing deformation layer from prior polishing steps. Indentations were placed on this polished surface using two indenter systems, both fitted with a cube corner indenter and operated in load control mode. A nanoindenter (Hysitron TriboScope®) with testing conditions as in [15] was applied for loads ranging from 40 µN to 10 mN, leading to indentation depths between 35 nm and 1800 nm. To increase the investigated range of penetration depths, larger indents were subsequently placed on the same sample using an *in-situ* microindenter (ASMEC UNAT), where applied loads of 200 mN and 300 mN led to penetration depths of 9.2 µm and 11.35 µm, respectively. During the indentation experiments force and penetration depth were recorded and used to determine hardness and indentation modulus. Subsequently, atomic force microscopy (AFM) scans (Digital Instruments Dimension 3100) were performed to image selected indents. The surface topography of an imprint made with a maximum load of 280 µN is included in Fig. 1.

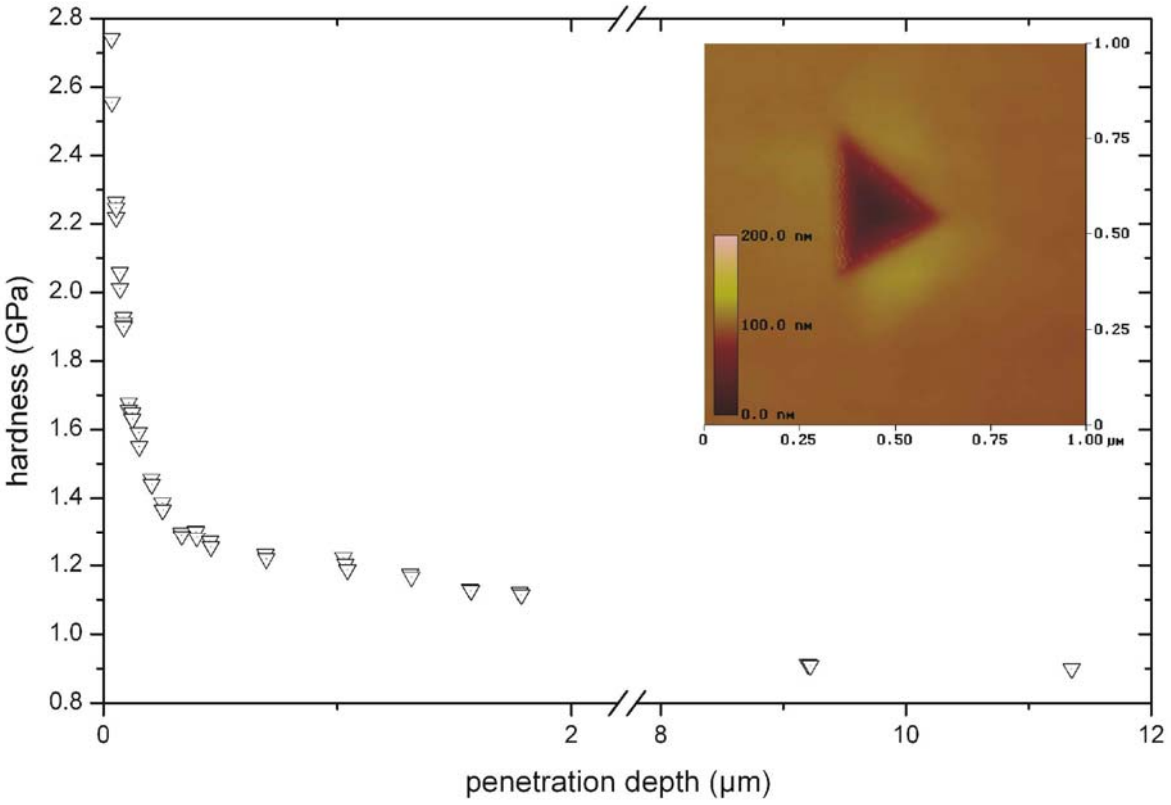

Fig. 1: Hardness versus penetration depth for various indents in single crystal Cu with a <111> surface normal. A pronounced indentation size effect showing increased hardness for reduced penetration depth was observed. The inset shows an AFM image of an indent into single crystal Cu with a <111> surface normal using a cube corner indenter and a maximum force of 280 µN.

Accurate hardness values can only be obtained if a calibrated area function and a correct value for the machine compliance are used. At the indenter flanks material piles up (see AFM image in Fig. 1), making an accurate determination of the actual contact area by subsequent imaging methods rather difficult, which in turn results in errors in the determination of hardness and modulus [16–18]. To avoid these problems, the procedure outlined by Oliver and Pharr [7] was applied. The results of the hardness measurement accomplished on a <111> surface of a Cu single crystal are presented in Fig. 1. A rise in hardness from 0.9 GPa to 2.75 GPa is observed when decreasing the penetration depth from 11.35 µm to 35 nm. This well-known ISE is recently extensively discussed in literature, e.g. [6, 7, 19].

2.2 Micro-compression

A Cu single crystal with a <111> surface normal, prepared in the same way as described above, was covered with a protective 1.2 µm thick TiN coating. This sample was carefully polished using an alumina suspension with a grain size of 1 µm perpendicular to the electro-polished and coated surface to achieve a sharp edge. The deformation layer due to this process had a thickness of ~5 µm and was totally removed by FIB milling (LEO 1540 XB). Along the edge compression samples with a square cross-section and a side length *a* between 1 µm and 8 µm and an aspect ratio between 1.5 and 2 were milled (inset Fig. 2). The loading of the compression columns was performed *in-situ* in an SEM (LEO Stereoscan 440) using a microindenter (ASMEC UNAT) equipped with a flat diamond punch. The tests were performed displacement controlled and all samples were compressed to strains larger than 0.3. Force and displacement data were collected during the experiment. The inset in Fig. 2 shows an SEM image of the inclined view of a Cu single crystal column with a side length a = 8 µm and a <111> surface normal after compression testing. The protective TiN coating is marked with an arrow. Glidesteps originating from the compressive loading to a strain of 0.32 are observed on the sample surface. For details on sample fabrication, ion beam damage, and testing refer to [20, 21].

Engineering stress versus engineering strain curves were calculated from the recorded load–displacement data and the known sample dimensions. The flow stress data $\sigma_{0.05}$ at a strain of 5 % are shown in Fig. 2 as a function of the column diameter, representing the diameter of a circle with the same cross-sectional area as the tested column. A rise of the flow stress with decreased column diameter, as first reported by Uchic et al. [12], was also observed in these experiments. The largest samples with a diameter of 8 µm exhibited flow stresses of ~300 MPa, while for the smallest samples with diameters of 1 µm flow stresses of ~500 MPa were measured.

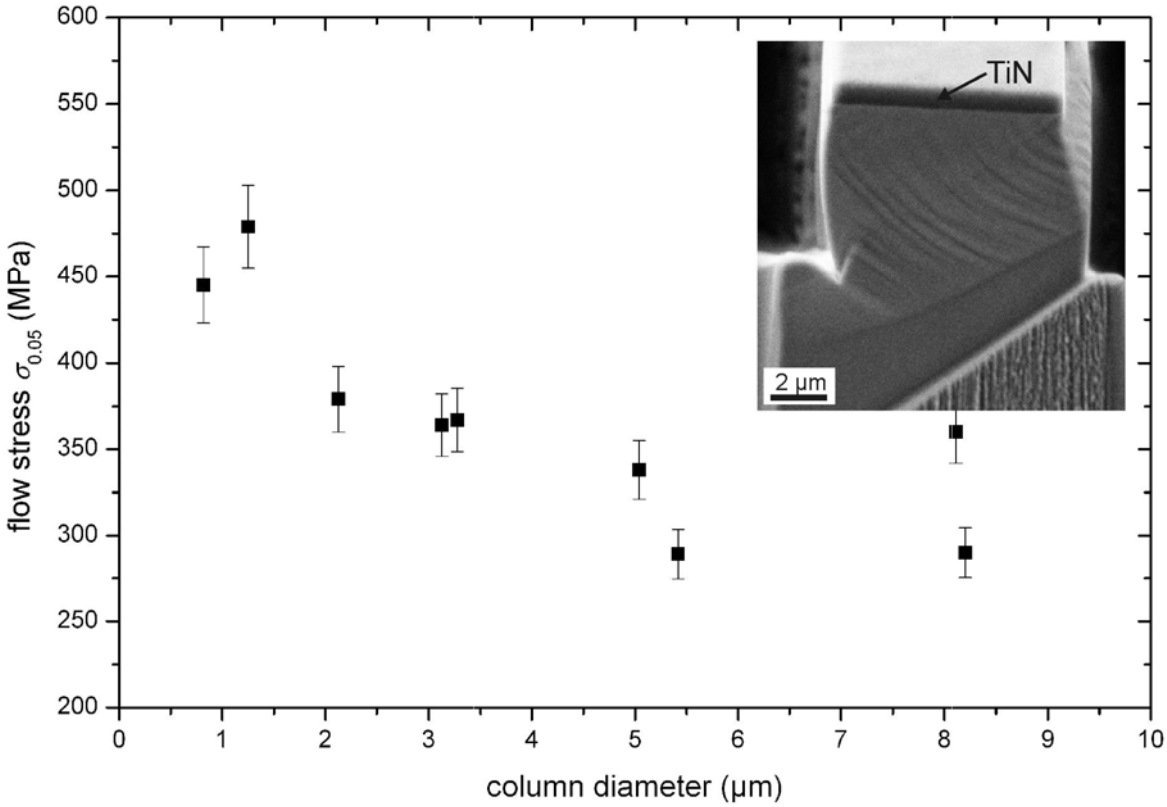

Fig. 2: Technical flow stress $\sigma_{0.05}$ at 5 % technical strain as a function of the column diameter for Cu columns with a square cross-section and a <111> surface normal. The inset SEM image shows the inclined view of a single crystal Cu column with a <111> surface normal and a side length *a* = 8 µm after compression testing. The protective TiN coating is marked.

2.3 Fiber tensile testing

Polycrystalline Cu wires (99.99 % Cu) with as-received diameters of 50 µm and 25 µm were heat treated in a vacuum furnace for 2 hours at 600 °C to remove internal stresses and microstructural defects from the fabrication process. This resulted in a recrystallized bamboo structure. The 50 µm wires were electrolytically thinned to diameters of 40 µm and 25 µm. Thinner wires of 20 µm and 15 µm were fabricated by electrolytic polishing of the heat treated 25 µm wires. Samples with a gauge length of 2 mm were mounted on a sample stage and tested *in-situ* inside an SEM (LEO 1525) using a novel fiber-tension module (Kammrath & Weiss). The tests were conducted load controlled with a strain rate of $2.5 \cdot 10^{-3}$ s^{-1} until the specimen fractured. Force and displacement data were recorded during the experiment. Figure 3a shows a polycrystalline Cu wire with a diameter of 25 µm during loading,

the load is applied via the micro-tweezers. The inset shows a detail of the deformed wire, where individual slip steps can be observed on the surface of several grains with an inclination angle of about 45° to the loading direction. For further experimental details refer to [22].

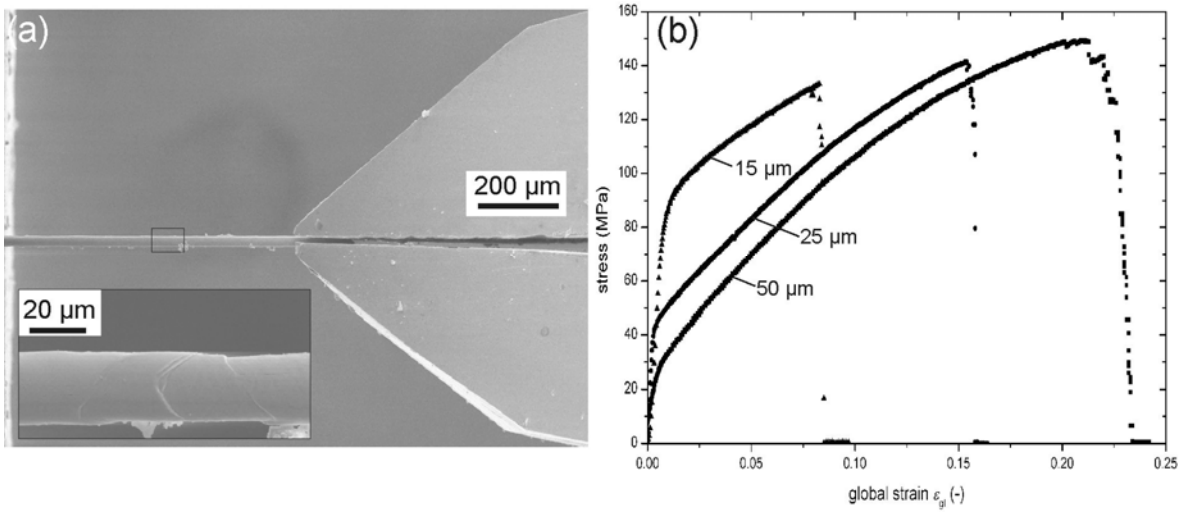

Fig. 3: (a) SEM image of a polycrystalline Cu wire with a diameter of 25 µm during loading via micro-tweezers. The inset shows a detail of the deformed specimen with glide steps inclined by about 45° to the loading direction. (b) Determined technical stress–strain curves for polycrystalline Cu wires with diameters of 50 µm, 25 µm, and 15 µm.

Engineering stress versus global strain curves were calculated from the force–displacement data. Therefore, it was assumed that the samples posses a circular cross-section. The curves obtained for samples with wire diameters of 50 µm, 25 µm, and 15 µm are shown in Fig. 3b. A rise in flow stress $\sigma_{0.05}$ at a global strain of 5 % from ~90 MPa for a wire diameter of 50 µm to ~130 MPa for 15 µm diameter, along with a reduction in fracture strain, was observed.

2.4 HPT tensile testing

The principle of SPD using HPT is depicted in Fig. 4a. The disk-like sample with a diameter of 14 mm and a thickness of 2 mm machined from a larger oxygen-free high clean Cu sample is placed between the two anvils of the HPT-tool and loaded with a high hydrostatic pressure of 4 GPa. The sample is then deformed in simple shear by rotating one of the anvils with respect to the other. HPT was applied to

single crystal Cu up to a van Mises equivalent strain ε_{vM} > 6400 %. The deformed samples show a polycrystalline microstructure with a weak shear texture [23] and possess an average grain size of ~200 ± 100 nm. Heat treatments in a vacuum furnace were applied to adjust the grain size to average diameters of 1, 10, and 100 µm. Tension specimen with a gauge length of 8 mm and a cross-section of 1.2 mm × 1 mm were machined from these disks (see Fig. 4b).

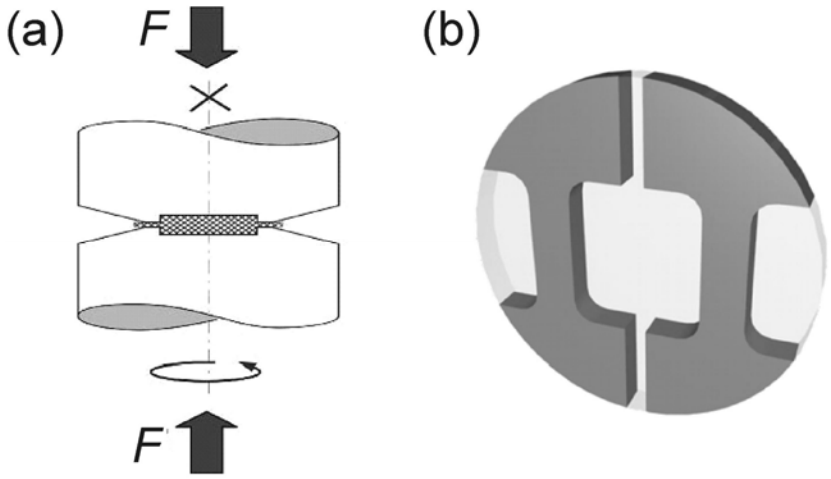

Fig. 4: (a) Working principle of high pressure torsion (HPT) with the sample between the upper and the lower anvil. After deformation and heat treatment tension specimens with a gauge length of 8 millimeter were machined as depicted in (b). See text for details.

These tensile test samples were loaded *in-situ* in an SEM (LEO 1525) using a tension module (Kammrath & Weiss). All specimens were loaded until fracture; in a cross-head displacement controlled experiment the load versus displacement data was recorded. The oxygen-free highly clean samples are identical in saturation grain size, texture, misorientation, and hardening behavior to HPT samples fabricated from high purity Cu single crystals [24]. Furthermore, the lower purity improves the thermal stability of the microstructure.

Figure 5a shows an SEM image of the constricted zone of a Cu tension specimen with an average grain size of 100 µm just before fracture. Crack initiation from the top of the sample becomes visible.

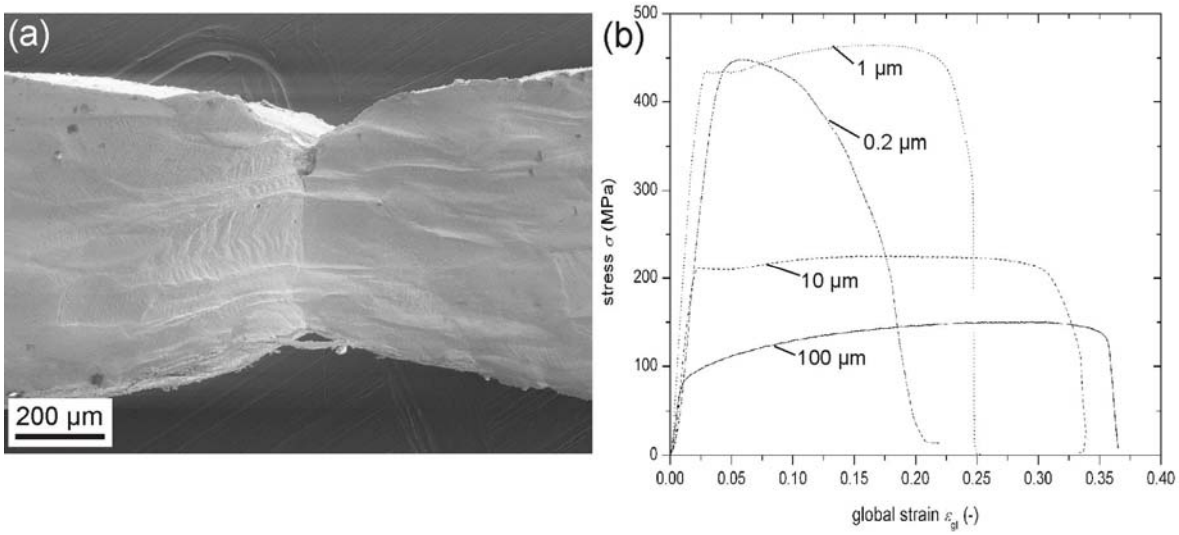

Fig. 5: (a) SEM image of a Cu tension specimen with a grain size of 100 µm close to fracture. Glide steps are visible across the constricted zone. (b) Calculated technical stress versus global strain curves for tension samples fabricated from HPT deformed and subsequently annealed Cu with average grain sizes of 1, 10, and 100 µm. Note that the sample with 0.2 µm grain size was not annealed after HPT.

The engineering stress versus global strain curves calculated from the sample dimensions and the data collected during the tension tests performed on HPT Cu are shown in Fig. 5b for the four investigated grain sizes indicating a Hall–Petch-like behavior with an increase in flow stress with reduced grain size. The ultimate tensile strain depends significantly on the grain size. The sample with 0.2 µm grain size shows a reduced fracture strain compared to the 1 µm specimen, but a comparable flow stress of about 450 MPa. For the samples with a mean grain size of 100 µm and 10 µm, clearly divergent flow stress levels of about 80 MPa and about 220 MPa were observed. The deformation structure evolving during tensile testing [25] was investigated by electron backscatter diffraction (EBSD) scans. The specimens with 100 µm and 10 µm grains show a distinctive formation of subgrains resulting from dislocation–dislocation interactions. The specimen with 1 µm grain size is predominantly devoid of internal dislocation cell structures (substructures). Therefore, only a minor amount of dislocation interactions took place and consequently only weak hardening, caused by dislocation pile-up at grain boundaries, was observed. In contrast to the above discussed recrystallized HPT specimen, the tensile samples with an average grain size of 0.2 µm have a

recovered severe plastic deformation structure with a high dislocation density and a high amount of low angle boundaries (about 25 %). The dislocation generation and absorption in these boundaries could be easier than in the well-defined recrystallized grain boundaries. Therefore, it is expected that the deformation process in the unannealed HPT samples are different compared to the recrystallized ones.

3. Discussion

To compare the different results in a consistent manner, some data processing as outlined below was carried out.

In Fig. 6 the flow stress of Cu determined by the different applied methods is plotted versus the *critical dimension*, i.e. average grain size (HPT tensile testing), fiber diameter (fiber tensile testing), column diameter (micro-compression), and the indenter side length *s* at the corresponding penetration depth *h* (nanoindentation). This side length *s* can be calculated, taking into account the area function of an ideal cube corner, with $s = 2.45 \cdot h$. The side length of the cube corner indenter impressed in the material is a more meaningful characteristic length when talking of dislocation activities, e.g. the emission of prismatic dislocation loops [6], than the penetration depth.

All flow stresses from compression and tension experiments were determined at an engineering strain ε = 0.05. The hardness results from the nanoindentation experiments were converted to a yield strength using the Tabor approximation $H \approx 3 \cdot \sigma_y$ [6]. Any additional hardening between this calculated yield strength σ_y and the flow stress at a strain of 0.05 was neglected. The model by Dao et al. [10] for calculating yield strength values from indentation data led in our case to unreasonable results for the small indentation depths, as the ratio between elastic and plastic work is significantly higher than in their continuum mechanics considerations for relatively large indents.

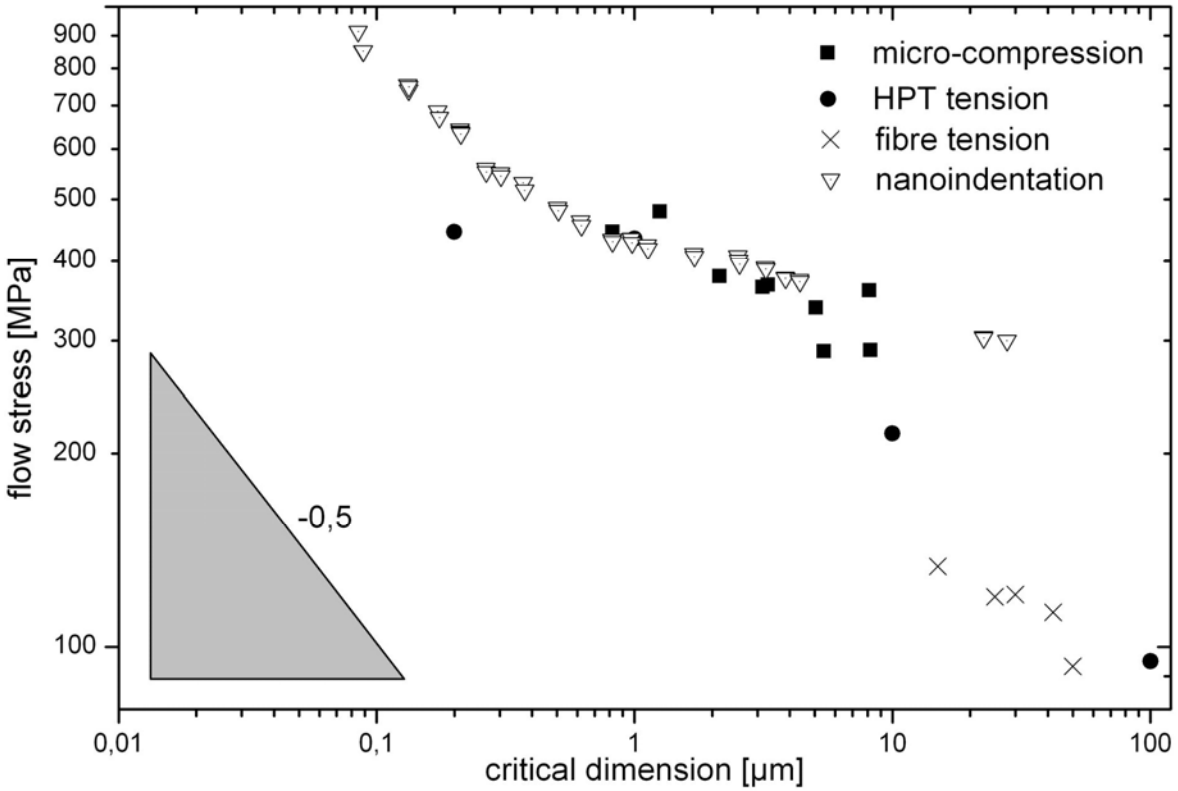

Fig. 6: Comparison of the size-dependent stress values of Cu determined by four different methods. For the compression and tension experiments the flow stress at a strain of 0.05 is plotted. The nanoindentation results are shown using the Tabor approximation ($H \approx 3 \cdot \sigma_y$ [6]).

There are several differences in the crystal orientation as well as the stress state of the samples leading to different stress levels for the various tests summarized in Fig. 6. Since plastic deformation is controlled by the motion of dislocations under an applied shear stress, it is more appropriate to compare the results using the resolved shear stress (Fig. 7). In order to convert normal stress (Fig. 6) to shear stress (Fig. 7), a Schmid factor m_{111} = 0.278 was used for the micro-compression samples, corresponding to the (111) crystal orientation and <111> loading direction. The polycrystalline HPT tension samples with their nearly random texture and the large number of grains in the tested volume can be considered as bulk samples. Therefore, a Taylor factor M_T = 3.06 [26] was applied. The same Taylor factor was used in the case of the nanoindentation results, as the complex stress and strain state beneath an indenter requires the activation of multiple glide systems, similar to the deformation of a polycrystal. In the case of the fiber tensile testing specimen a Schmid factor m_{fiber} = 0.5 was considered, assuming that due to the long gauge length, and the large number of individual grains within this

length (at least ~40 grains for the thickest tested sample), always one or more grains are oriented in or close to the direction of the highest possible Schmid factor. This assumption is supported by the inclination angle of the slip planes (e.g. inset of Fig. 3a), and by other findings in literature [27]. For all experiments, any change of the Schmid factor due to a rotation of the glide planes with ongoing plastic deformation was neglected. The results for micro-compression, HPT tension, fiber-tension, and nanoindentation with a critical dimension smaller than 1 µm fall together on a line with a slope of –0.3 (Fig. 7). For larger indents there is a deviation from this line, which is usually interpreted in terms of a constant hardness in the limit of infinite depth [6]. For the present indentation depths of several µm a constant hardness value is not yet reached. One might expect this shear stress to correspond to the critical shear stress exhibited by a single crystal under multiple slip conditions.

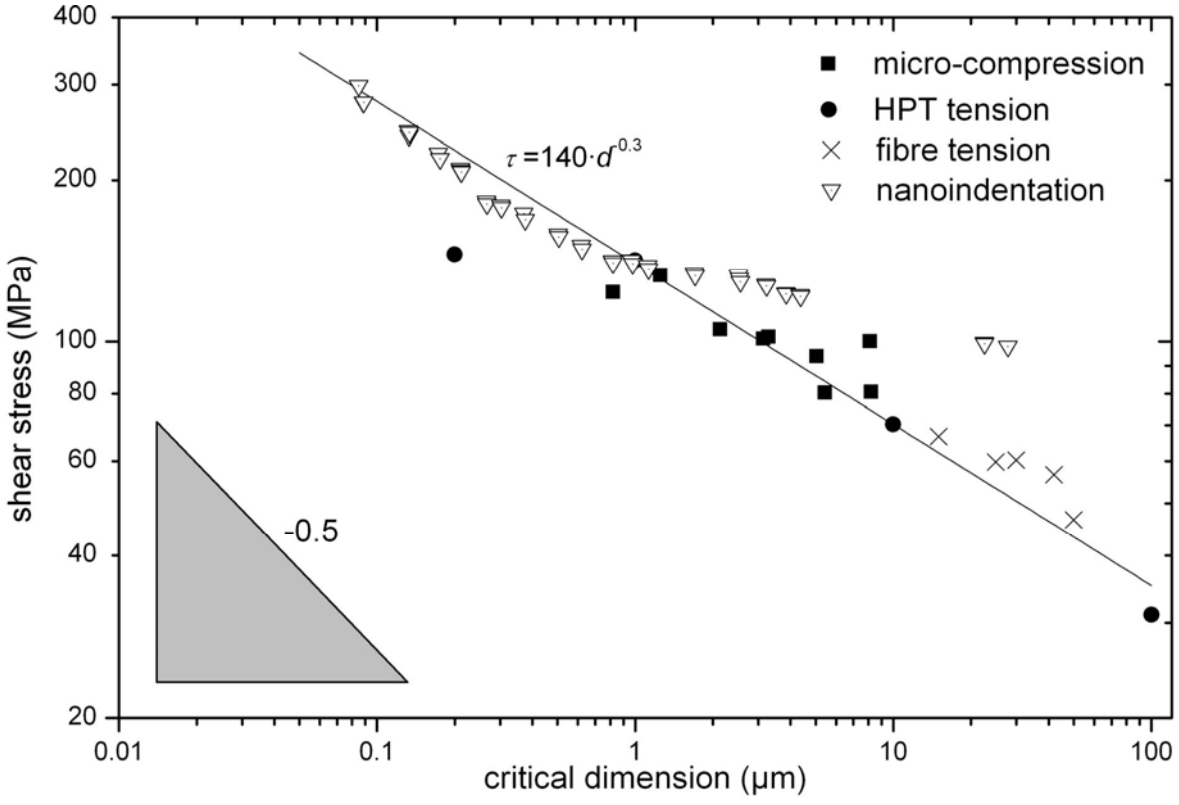

Fig. 7: Resolved shear stress versus the critical dimension of the individual tests. For the compression and tension experiments the shear stress at a strain of 0.05 is plotted. The nanoindentation results are plotted applying Tabors rule.

To gain more insight into the mechanisms controlling deformation at the different length scales, we plotted the data of Fig. 7 in terms of a Hall–Petch plot (Fig. 8).

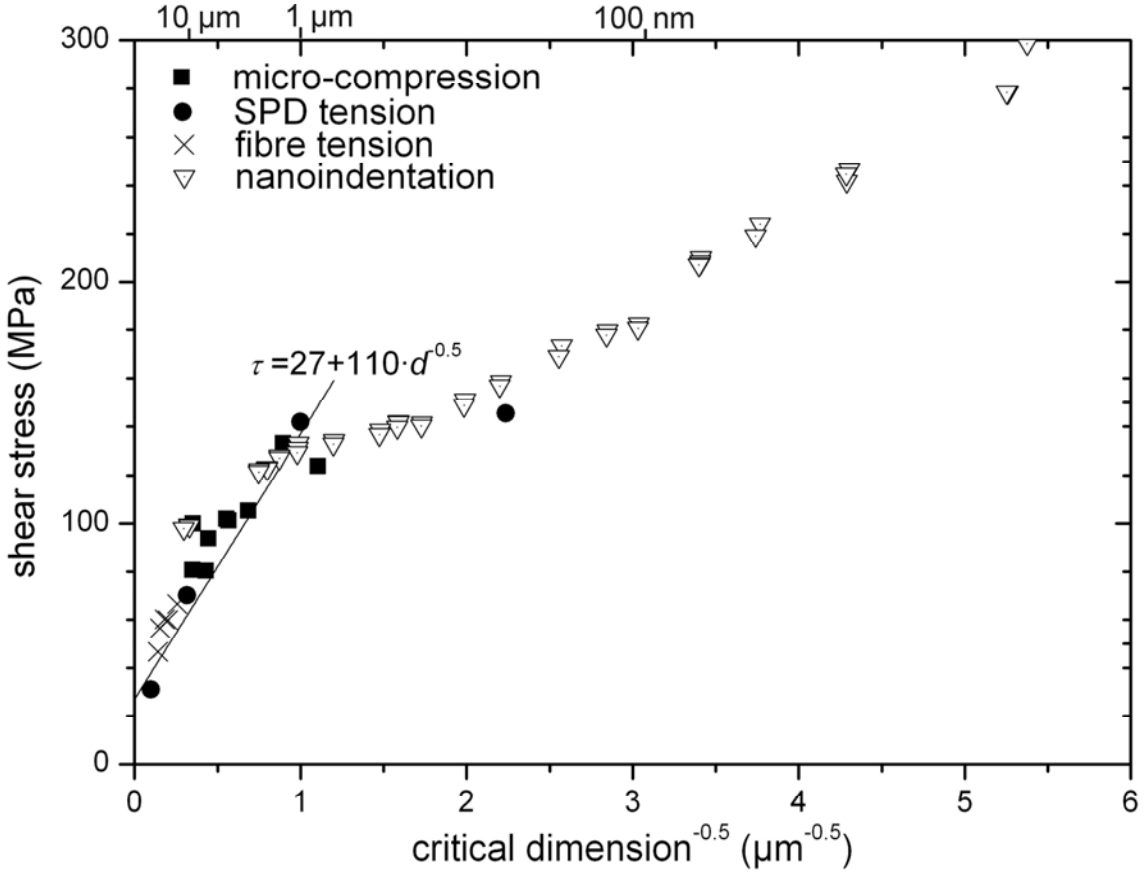

Fig. 8: Hall–Petch plot of the resolved shear stress for the different individual tests, evaluated at 5 % strain for the compression and tension experiments and by applying Tabors rule for the nanoindentation results. A mechanism change at a critical dimension of about 1 µm can be seen.

Again, two regimes can be deduced. In the regime with critical dimensions larger than about 1 µm a linear fit of the data leads to an axis intercept of τ_0 = 27 MPa and a slope K_{HP} = 110 MPa µm$^{0.5}$. The deduced values are in agreement with σ_0 = 26 MPa and K_{HP} = 112 MPa µm$^{0.5}$ published by Armstrong et al. [28]. They determined macroscopically σ_0 at a strain of ε = 0.005 compared to ε = 0.05 for τ_0 in our case. The testing temperature of 300 K and the strain rate $\dot{\varepsilon} = 2 \cdot 10^{-4}$ were comparable to our experiments. The behavior in this regime can be explained in terms of dislocation interaction and pile up as analyzed in a very comprehensive way by Conrad [3, 4]. The regime with critical dimensions smaller than about 1 µm can not be fitted reasonably well using a linear function. For polycrystalline

samples with grain sizes in this regime Conrad suggested pile up induced grain boundary shear to control the deformation behavior. In the case of micro-compression and nanoindentation, no grain boundaries are present. Therefore, we assume dislocation sources to play a more dominant role in the sub-micrometer regime. Following the work of Friedman & Chrzan [29] and von Blanckenhagen et al. [30], one can expand the Hall–Petch relation [1, 2]:

$$\tau_{\mathrm{app}} = \tau_0 + K_{\mathrm{HP}} \cdot \frac{1}{\sqrt{d}} \tag{III.1}$$

to include a source term in the following form:

$$\tau_{\mathrm{app}} = \sqrt{\frac{(1-\nu) \cdot K_{\mathrm{HP}}^2}{d} + \tau_{\mathrm{source}}^2}\ , \tag{III.2}$$

where the Poisson ratio ν = 0.34 and the source strength τ_{source} is given by:

$$\tau_{\mathrm{source}} = \frac{Gb}{2\pi} \cdot \frac{1}{S} \cdot \ln\left(\frac{\alpha \cdot S}{b}\right). \tag{III.3}$$

G = 47 GPa is the polycrystalline shear modulus, *b* = 0.256 nm the Burgers vector, *S* the source size, which was assumed to be half the critical dimension, and α is a numerical constant in the order of unity.

A plot of the difference between the squares of applied stress and source strength versus the inverse critical dimension should lead to a straight line with the slope proportional to $(1\text{-}\nu) \cdot K_{\mathrm{HP}}^2$, if the deformation behavior is controlled by a dislocation pile up. Figure 9 shows this plot for the experiments discussed in this manuscript. Three regimes can be distinguished. For dimensions larger than about 1 µm a linear dislocation pile up behavior is found (regime I) and we evaluated K_{HP} = 114 MPa µm$^{0.5}$ in agreement with results derived above. This reveals that the included source term plays only a minor role for length scales larger than 1 µm. With decreasing critical dimension an increasing influence of this source term leads to a deviation from the linear behavior (regime II) and finally becomes dominant for the smallest indents (regime III).

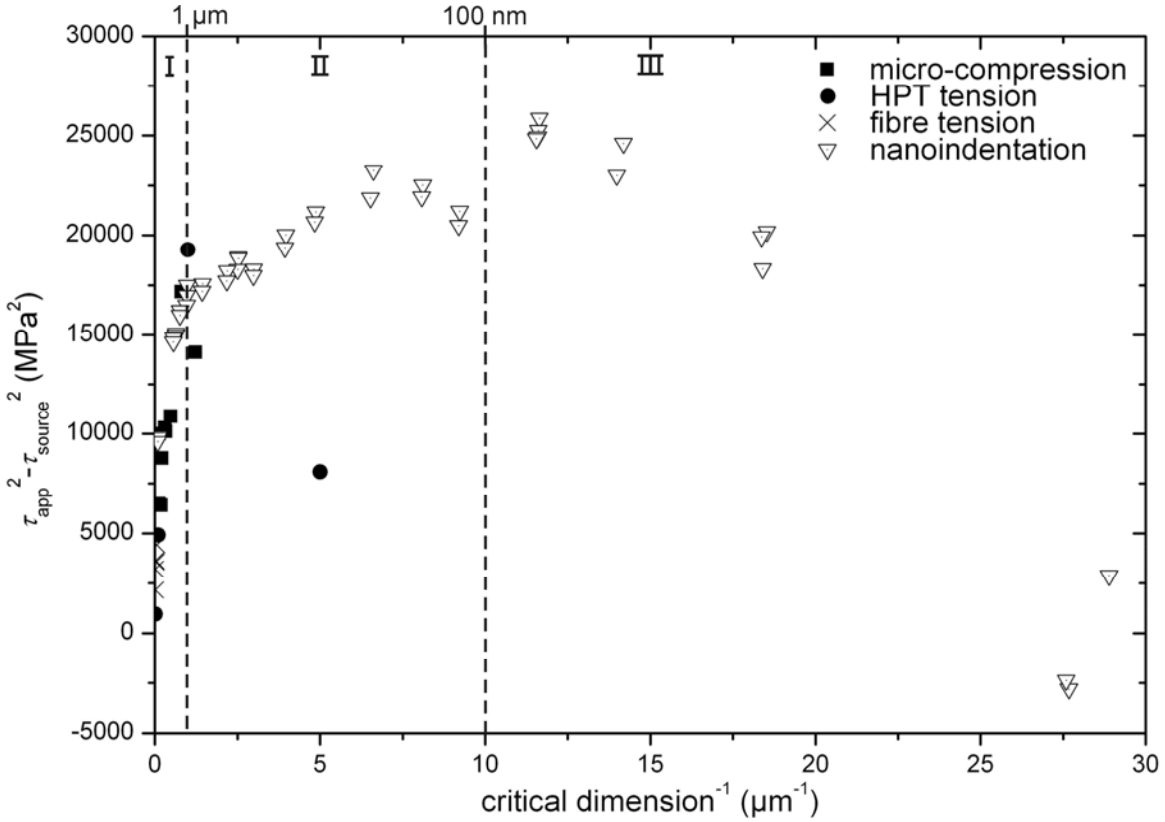

Fig. 9: Modified Hall–Petch plot with a source strength term included, showing the classical pile-up behavior for large critical dimensions (regime I) and the increased influence of the source strength for critical dimensions between ~1 µm and ~100 nm (regime II). Regime III is controlled by dislocation nucleation, the dimensions are too small for significant pile-ups.

The physically meaningless negative ($\tau_{app}^2 - \tau_{source}^2$) values for the smallest indents are a result of the increase in errors with decreasing length scale. The calculated source sizes for the smallest indents are in the order of several Burgers vectors, a length scale where the present approach may be to simplistic since effects like surface roughness [31] or partial dislocation nucleation [32] may alter the nucleation stress. It is also worth noting that the unannealed 0.2 µm HPT sample clearly falls off the trend exhibited by the other results, indicating, for example, differences in generation/annihilation of dislocations like disintegration of grain boundaries. This discrepancy was not rationalized in the classical Hall–Petch plot of Fig. 8 and only became evident when considering the competition between dislocation pile-up and nucleation.

The analyses of our data indicates that regime I is controlled by dislocation pile-up (d > 1 μm), regime II shows a competition between pile-up and nucleation (100 nm < d < 1 μm), and regime III (d < 100 nm) is finally dominated by dislocation nucleation.

4. Conclusions

We applied four different methods to investigate the size-dependent flow stress of Cu from critical dimension of several tens of micrometers down to several tens of nanometers. An increased flow stress with reduced critical dimension was observed. It was shown that the different stress levels for the individual experiments result from the different loading conditions and can be interpreted conclusive in terms of the resolved shear stress. For critical dimensions below 1 μm the activation of sources controls the deformation behavior, which can be accounted for by including a source term into the classical Hall–Petch relation.

References

[1] E. O. Hall, Proc. R. Soc. Lond. 1951; B64: 747.

[2] N. J. Petch, J. Iron Steel 1953; 174: 25.

[3] H. Conrad, Metall. Mater. Trans. A 2004; 35A: 2681.

[4] H. Conrad, Mater. Sci. Eng. A 2003; 341: 216.

[5] E. Arzt, Acta Mater. 1998; 46: 5611.

[6] W. D. Nix and H. Gao, J. Mech. Phys. Solids 1998; 46: 411.

[7] W. C. Oliver and G. M. Pharr, J. Mater. Res. 1992; 7: 1564.

[8] S. Vadalakonda, R. Banerjee, A. Puthcode, and R. Mirshams, Mater. Sci. Eng. A 2006; 426: 208.

[9] A. E. Giannakopoulos and S. Suresh, Scripta Mater. 1999; 40: 1191.

[10] M. Dao, N. Chollacoop, K. J. Van Vliet, T. A. Venkatesh, and S. Suresh, Acta Mater. 2001; 49: 3899.

[11] J. G. Swadener, E. P. George, and G. M. Pharr, J. Mech. Phys. Solids 2002; 50: 681.

[12] M. D. Uchic, D. M. Dimiduk, J. N. Florando, and W. D. Nix, Science 2004; 305: 986.

[13] D. M. Dimiduk, M. D. Uchic, and T. A. Parthasarathy, Acta Mater. 2005; 53: 4065.

[14] R. Pippan, F. Wetscher, M. Hafok, A. Vorhauer, and I. Sabirov, Adv. Eng. Mater. 2006; 8: 1046.

[15] M. Rester, C. Motz, and R. Pippan, Acta Mater. 2007; accepted.

[16] K. W. McElhaney, J. J. Vlassak, and W. D. Nix, J. Mater. Res. 1998; 13: 1300.

[17] A. Bolshakov and G. M. Pharr, J. Mater. Res. 1998; 13: 1049.

[18] B. Taljat and G. M. Pharr, Int. J. Solids & Struct. 2004; 41: 3891.

[19] N. A. Fleck and J. W. Hutchinson, J. Mech. Phys. Solids 2001; 49: 2245.

[20] D. Kiener, C. Motz, T. Schöberl, M. Jenko, and G. Dehm, Adv. Eng. Mater. 2006; 8: 1119.

[21] D. Kiener, C. Motz, M. Rester, and G. Dehm, Mater. Sci. Eng. A 2007; 459: 262.

[22] B. Yang, C. Motz, W. Grosinger, W. Kammrath, and G. Dehm, unpublished.

[23] T. Hebesberger, H. P. Stüwe, A. Vorhauer, F. Wetscher, and R. Pippan, Acta Mater. 2005; 53: 393.

[24] M. Hafok, A. Vorhauer, J. Keckes, and R. Pippan, Mater. Sci. Forum 2006; 503-504: 621.

[25] S. Scheriau, Diploma Thesis, Institute of Metal Physics, University of Leoben 2006.

[26] D. Hull and D. Bacon, *Introduction to Dislocations* (Elsevier Butterworth-Heinemann, Oxford, 2004).

[27] G. Khatibi, A. Betzwar-Kotas, V. Gröger, and B. Weiss, Fatigue Fract. Eng. Mater. Struct. 2005; 28: 723.

[28] R. Armstrong, R. M. Douthwaite, I. Codd, and N. J. Petch, Phil. Mag. 1962; 7: 45.

[29] L. H. Friedman and D. C. Chrzan, Phil. Mag. A 1998; 77: 1185.

[30] B. von Blanckenhagen, E. Arzt, and P. Gumbsch, Acta Mater. 2004; 52: 773.

[31] R. V. Kukta, A. Peralta, and D. Kouris, Phys. Rev. Lett. 2002; 88: 186102.

[32] H. Van Swygenhoven, P. M. Derlet, and A. G. Froseth, Acta Mater. 2006; 54: 1975.

IV On the role of stress concentrations for single crystal copper tested by micro-compression (Publication C)

D. Kiener, C. Motz, and G. Dehm

Manuscript under preparation.

Abstract

To investigate the origin of the specimen size effect observed in miniaturized compression experiments, *in-situ* deformation inside a scanning electron microscope was performed on focussed ion beam fabricated Cu single crystal columns. It is demonstrated that stress concentrations at the column base can be so strong that the size effect on the flow stress can disappear. This behaviour is analyzed for (100) and (111) oriented Cu columns with two different specimen shapes. In contrast to theoretical predictions of dislocation starvation, local misorientations close to the surface of deformed columns measured by electron backscatter diffraction indicate substantial dislocation pile-ups. This behaviour is explained by a two-dimensional dislocation model and may explain the origin of the geometrical site effect.

1. Introduction

An increased flow stress with reduced sample size for compression samples with dimensions of several μm was first reported by Uchic et al. [1]. This observation has drawn considerable interest and stimulated several research groups to analyze different metals [2-6] in order to develop a basic understanding of the processes governing deformation at small length scales. Several models were proposed to explain this size effect under uniaxial loading, where nominally no strain gradients are present [3, 5, 7, 8]. Greer et al. [3] proposed a dislocation-starvation model, Volkert and Lilleodden [5] argued that surface image stresses lead to a loss of dislocations. Zuo and Ngan [7] gave a probability based criterion for the yield strength of micron-sized columns depending on their volume. Parthasarathy et al. [8] considered the stochastic of single-ended dislocation source lengths in finite volumes to explain the observed size effect in the concept of dislocation starvation. The last two models fit the available data reasonably well, however it remains unclear whether the proposed dislocation starvation stems from a lack of nucleation/multiplication events or generally from a lack of available sources.

In the present work we experimentally investigate the deformation behaviour of micron-sized Cu compression samples with two different crystallographic orientations. Additionally, we analyze the deformed samples by electron backscatter diffraction (EBSD) to detect local changes in crystal orientation.

2. Experimental

Differently oriented columns, either with a (100) or a (111) surface (hereafter named Cu(100) or Cu(111)) were investigated. The samples were cut from two Cu single crystals using a diamond wire saw, subsequently mechanically ground and electro-polished to remove the deformation layer from the cutting process. The Cu(111) samples were then covered with a protective TiN coating. Further details of the sample preparation are reported in [6]. For the usually investigated geometry, pre-forms with a square cross-section of 10 μm × 10 μm were milled under perpendicular Ga^+ ion impact with an ion current of 1 nA. For the final shaping the sample was tilted 54° with respect to the ion beam and milling was performed under grazing ion incident with a final milling current of 100 pA to

reduce the ion damage [9]. This approach also provides a constant sample cross-section over the whole sample height. All Cu(100) and Cu(111) micro-compression samples had a square cross-section with side-lengths *d* between 1 µm and 8 µm and height/side-length aspect ratios of 1.75 ± 0.25 [10].

For the Cu(100) samples additionally a cylindrical geometry, following the approach of Volkert and Lilleodden [5], was fabricated. These columns with a circular cross-section were milled using perpendicular ion impact and again a final milling current of 100 pA. These samples possess an unavoidable taper in the order of several degrees. They will be entitled cylindrical samples, although they actually possess the shape of a truncated cone.

The sample testing was performed *in-situ* in a scanning electron microscope (SEM) using a micro-indenter (UNAT ASMEC) equipped with a flat diamond or tungsten tip. The loading was accomplished in displacement controlled open loop mode applying strain rates in the order of $2 \cdot 10^{-3}$ s^{-1}. Samples were typically compressed to true strains $\varphi > 0.2$, and the force-displacement data was recorded. From the force-displacement data true stress (σ_f) versus true strain (φ) curves were calculated, assuming the volume to be conserved during plastic deformation. Further details are reported in [6]. To evaluate the flow stress data for the cylindrical columns, the sample diameter was measured at top and bottom of the column prior to deformation and the average value was used for data processing.

3. Results

The true stress versus true strain curves of three specimens with comparable dimensions representing the individual geometries are depicted in Fig. 1. To represent the columns with square cross-section by a single parameter, the diameter *d* of a circle with the equal cross-section was chosen. This diameter is also indicated in Fig. 1. There are certain differences in the deformation behaviour of the investigated geometries and orientations. When comparing the two specimens with square cross-section, it is obvious that the Cu(111) sample exhibits several distinct load drops associated with only minor elongation. Contrary, the Cu(100) specimen depicts only minor load drops but substantially large elongations between them. The cylindrical specimen shows no distinct load

drops and a monotone rise of the true stress with true strains up to ~20 % and subsequently some softening.

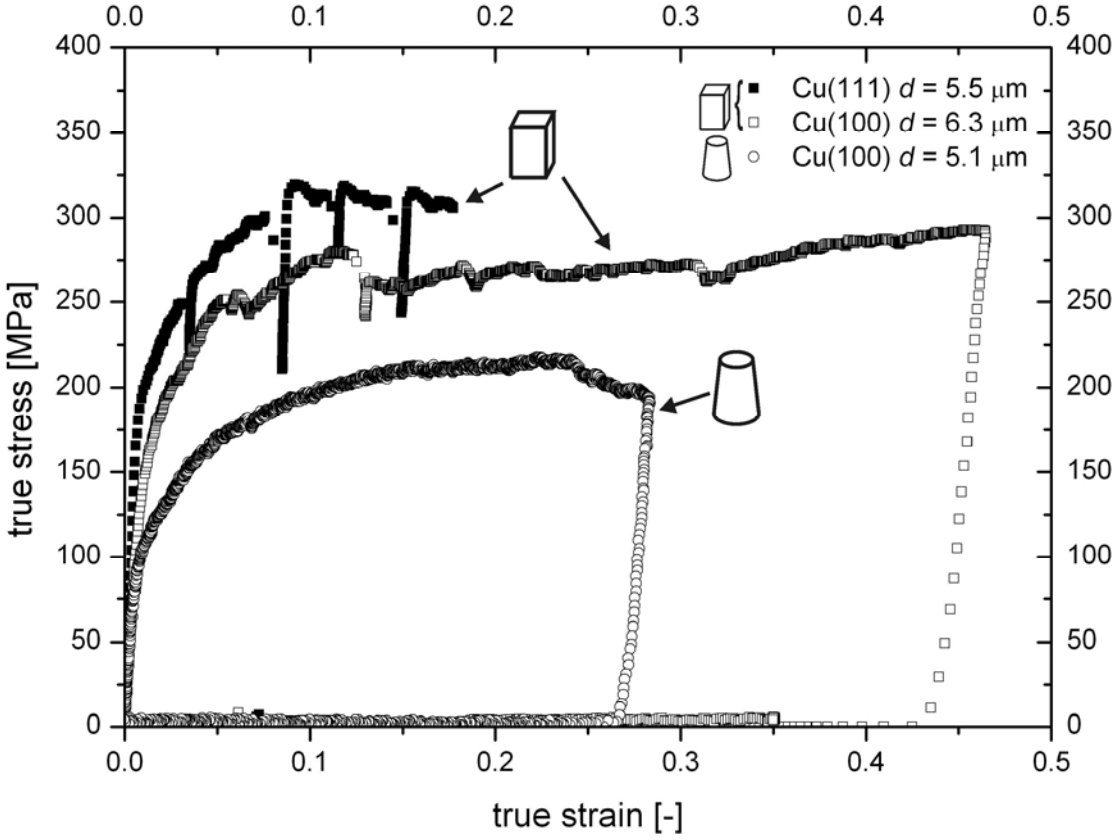

Fig. 1: True stress versus true strain curves observed for three specimens with comparable diameter representing the different investigated geometries and orientations. The Cu(111) specimen with square cross-section (full squares) presents distinct load drops accompanied by minor elongation. The Cu(100) sample with square cross-section (open squares) displays only minor load drops succeeded by very large elongation. The cylindrical Cu(100) specimen (open circles) depicts no distinct load drops and hardening to true strains larger than 20% and subsequently some softening.

To investigate the size dependence of the observed differences in the deformation behaviour, the flow stresses at φ = 0.2 for all samples with square cross-section loaded to strains larger than φ = 0.2 are summarized in Fig. 2. A remarkable difference between the two investigated crystal orientations is evident. While the Cu(111) samples exhibit a distinctive size effect with an increase in σ_f from ~300 MPa to 880 MPa (Fig. 2), a size-independent flow stress of 220 ± 60 MPa was

observed for the Cu(100) columns. For comparison, the tensile data of high purity bulk Cu with an average grain size of 10 µm [11] reveals a flow stress of 210 MPa at 20% tensile strain (dotted line in Fig. 2).

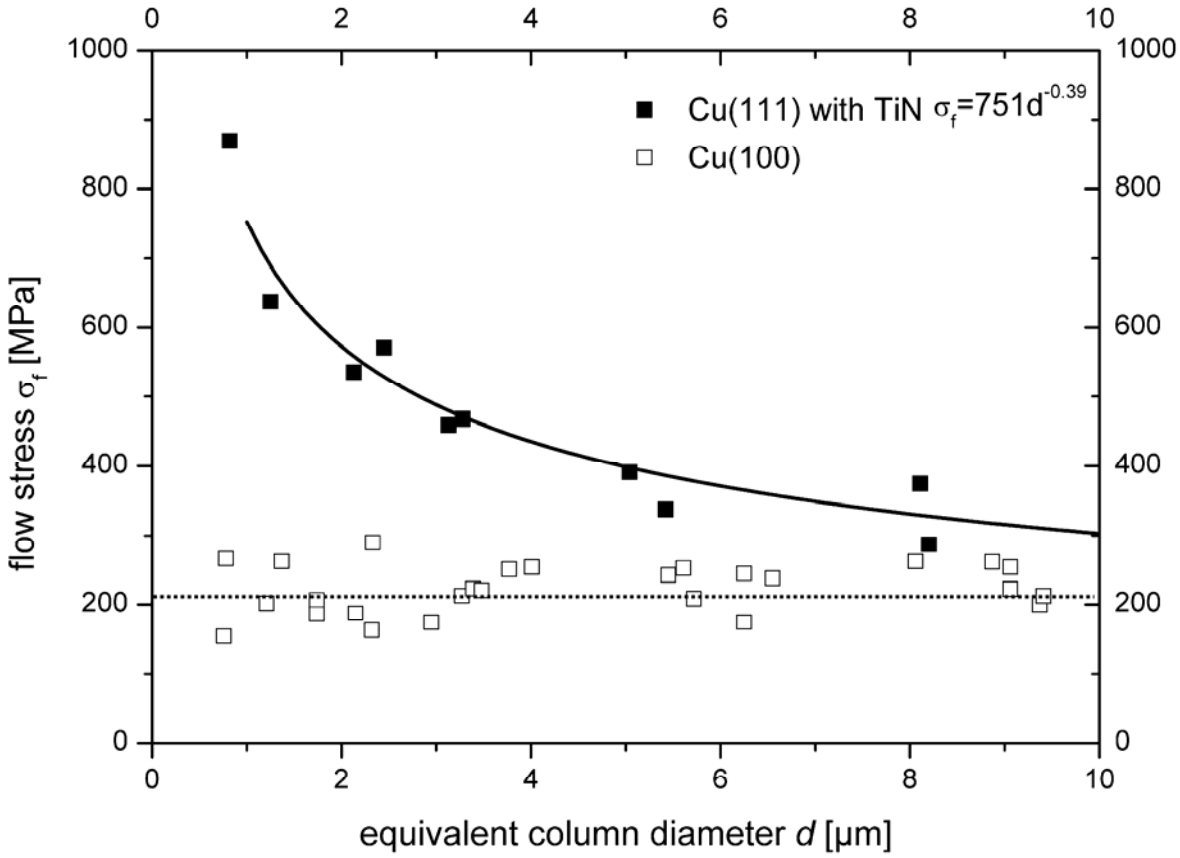

Fig. 2: Flow stress σ_f at a true strain φ = 0.2 observed for specimen with a square cross-section and different column diameters *d*. *d* equals the diameter of a circle with the same area as the square-shaped cross-section. The Cu(111) columns exhibit a remarkable size effect, while the Cu(100) samples show a size-independent flow stress. The dotted line indicates the flow stress at 20% tensile strain for high purity bulk Cu with an average grain size of 10 µm [11].

In-situ SEM observations provided insight in the deformation process and the order of acting glide planes as indicated in Fig. 3a. Using the FIB, cross-sections of several deformed columns were prepared and subsequently analyzed by EBSD. Fig. 3b shows the misorientation angle map of the deformed Cu(100) column shown in Fig. 3a, calculated from the local crystal orientations with respect to the initial crystal orientation. This initial orientation was determined by averaging the

crystal orientation of more than 100 measured points in the undeformed crystal. Most of the column remains within 0.5° to the original orientation, which is the accuracy of the EBSD system. Areas of about 5° misorientation are found at the edges of the sample. The (100) pole figure of the whole sample using the same colour coding is presented in the inset at the right bottom of Fig. 3b. The two insets at the top right and left display a detail of the pole figure for the two corners with the colour coding from green to red representing 0° to 5° misorientation from the crystal orientation at the corner. These regions are tilted about 5° from the initial crystal orientation in opposite directions, as can be seen by comparing the two pole figures. The area of larger misorientations of about 10° at the lower left corner of the compressed sample results from a contact of the slipped part of the column with the specimen base.

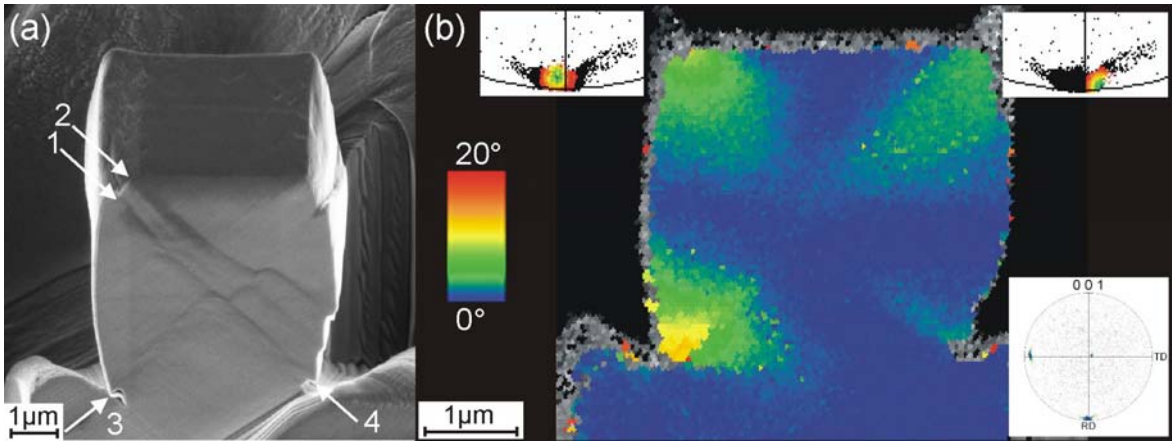

Fig. 3: (a) Inclined SEM image of a Cu(100) column with *d* = 5 µm after 20% compression. The numbered arrows indicate the acting glide plane and their order of activation as observed during the *in-situ* compression experiment. (b) Colour coded misorientations measured by EBSD on a cross-section of the compressed column (a) prepared by FIB milling. See text for details.

Significantly different flow stresses are observed for cylindrical Cu(100) samples. These samples exhibited a size-dependent flow stress ranging from 250 MPa for *d* = 6.7 µm to 470 MPa for *d* = 1.1 µm. All flow stress values of the cylindrical Cu(100) columns were converted to resolved shear stresses τ_{res} and compared with the Cu(111) samples (Fig. 4). The highest Schmid factors for the two orientations are m_{111} = 0.408 and m_{100} = 0.278. A change of the Schmid factor due to a rotation of the glide planes during ongoing plastic deformation is not

considered here. The cylindrical Cu(100) samples show an increase in τ_{res} with decreasing diameter, while no size effect was observed for the Cu(100) columns with the square cross-section. The dotted line depicts the resolved shear stress for the tensile tested bulk Cu with an average grain size of 10 µm at 20% tensile strain. Due to the polycrystalline microstructure [12], a Taylor factor M_T = 3.06 was applied to convert flow stress to shear stress.

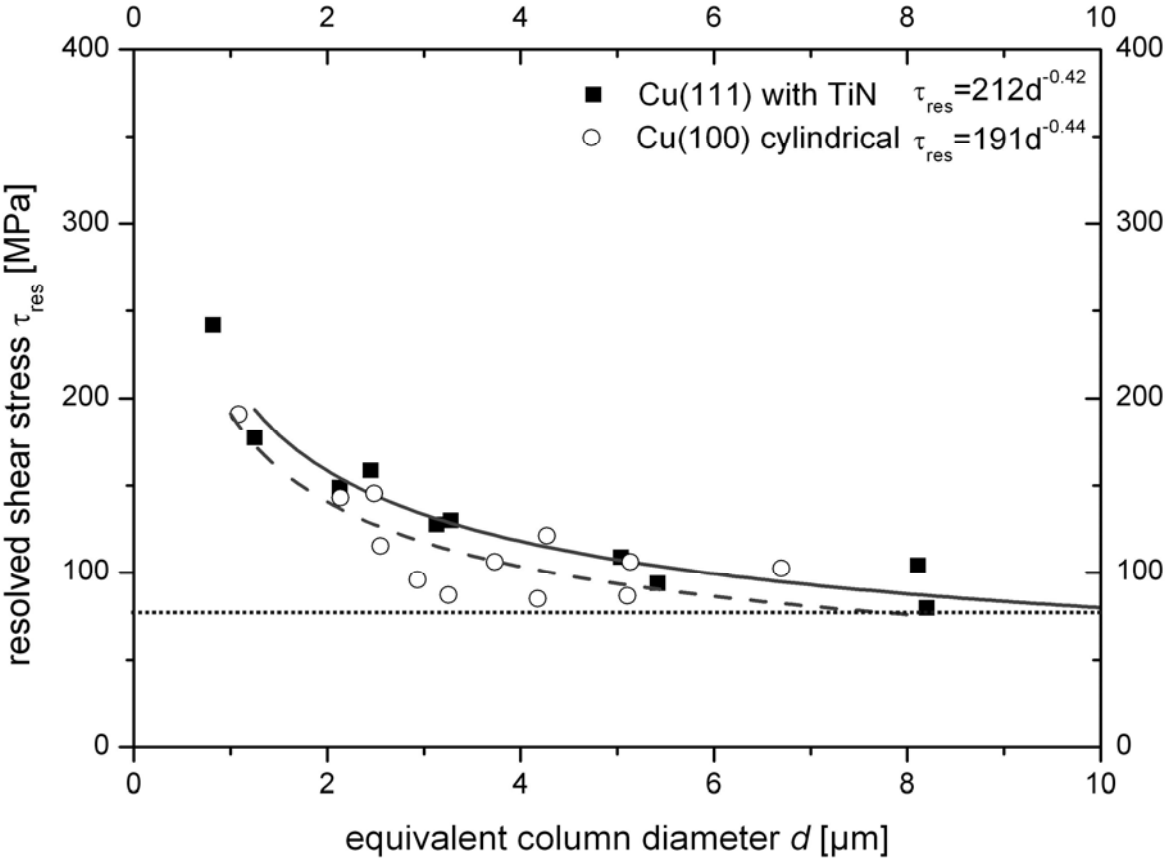

Fig. 4: Size-dependent resolved shear stress τ_{res} for Cu(111) samples with a square cross-section and cylindrical Cu(100) samples at φ = 0.2. Both curves reveal higher shear stresses for smaller sample sizes. The dotted line denotes the resolved shear stress (applying a Taylor-factor M_T = 3.06) for the tensile tested bulk Cu with an average grain size of 10 µm at 20% tensile strain [11].

4. Discussion

In contrast to the work of Uchic et al. [1] and Dimiduk et al. [2], a multiple slip orientation with 8 equivalent slip systems for Cu(100) and 6 for Cu(111) was chosen in this study. Consequently, multiple slip was observed for all columns (see Fig. 3a). The observed different size-dependent stress-strain behaviour of the samples with square cross-section and different crystal orientations is believed to result from constraints present at the sample top and base, as outlined below.

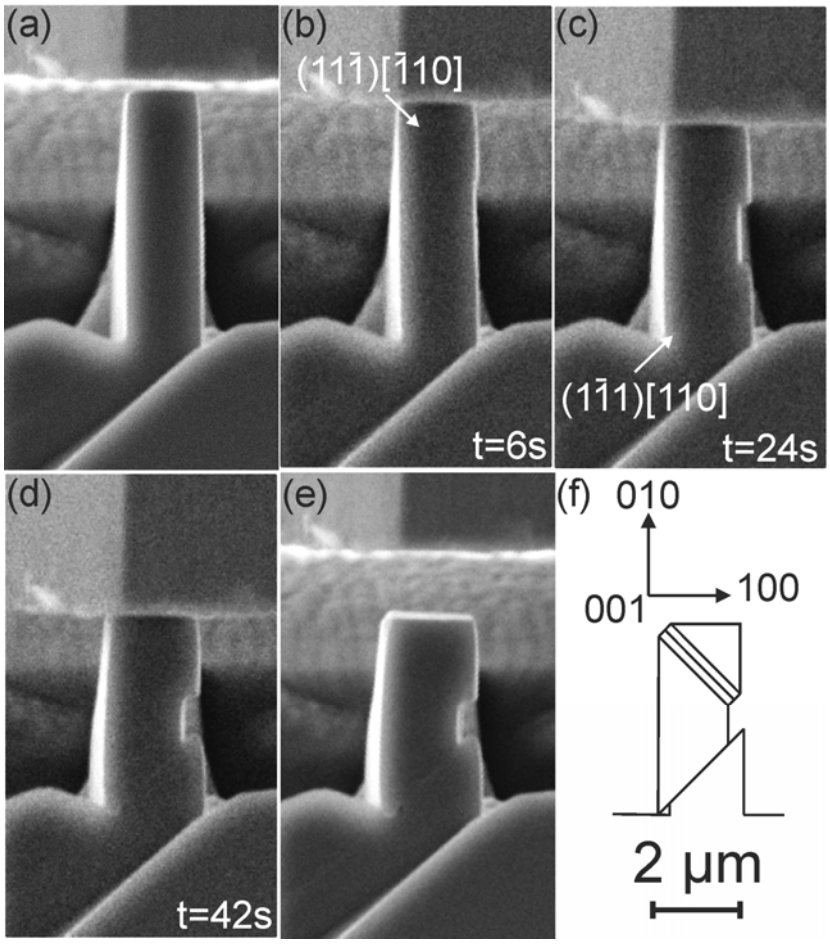

Fig. 5: (a)-(e) SEM images of a Cu(100) column taken *in-situ* (a) before, after (b) 6s, (c) 24s, (d) 42s of loading, and (e) after unloading. (f) Schematic of the initial crystal orientation and active glide planes during deformation.

Firstly, there is a constraint due to friction between the flat diamond tip and the sample top. It was pointed out by Raabe et al. [13] that an increased friction coefficient has a stabilizing effect on the compression sample. Nevertheless, this friction leads to a multi-axial stress state and higher shear stresses at the sample top. This constraint was further increased for the Cu(111) samples by a stiff TiN

coating, which is atomically bound to the Cu surface. Therefore, the deformation usually starts at the column top, as revealed experimentally. This is shown for a Cu(100) column with SEM images recorded during deformation (Fig. 5a-e). The schematic in Fig. 5f indicates the active glide systems and the crystallographic orientation of the crystal.

Secondly, there are constrictions to the glide of dislocations. Due to the small aspect ratio of the tested columns, it is likely that dislocations emitted from inside the volume glide to the sample top or bottom and pile-up as indicated in Fig. 6a for a two-dimensional dislocation model of a Cu(100) sample. The pile-up at the sample top is caused by the close contact formed with the flat punch, while at the bottom of the column the infinite crystal acts as a rigid plate. The pile-up at the specimen top causes the lattice rotation of 5° of the compressed column detected by EBSD (see Fig. 3b). The formation of a small angle grain boundary can be excluded, since the change in orientation is gradually. A quantitative evaluation of this model is outlined in the following paragraph.

Assume a homogenous distribution of dislocation sources over the sample volume with the projected glide systems indicated in the 2-dimensional sketch in Fig. 6a. A source situated in the shaded area 2 can emit a dislocation of type 2 into the grey area, while for glide system 1 this can only be achieved by sources in the shaded area 1. Therefore, the probability of type 2 dislocations to be injected into the grey area is, according to their area fraction, a factor 3 higher than for type 1 dislocations. If the experimental reduction in height for the specimen shown in Fig. 3b is accomplished by the two sets of slip planes of Fig. 6a, the net Burgers vector $\underline{B} = n_1 \cdot \underline{b_1} + n_2 \cdot \underline{b_2}$ in the shaded area is given by the number n_i of dislocations with the magnitude of their Burgers vector b_i for the dislocation system 1 and 2 (Fig. 6b). This calculation implies that the deformation is accomplished by equal activation of all available sources. $\underline{B}$ can be decomposed into a vertical component leading to a reduction of the specimen height, and a horizontal component, that would shift the loading axis of the sample (Fig. 6b). The stiff indenter system is expected to prevent this lateral displacement. Furthermore, the flat punch prevents the dislocations from leaving the sample. Therefore, dislocations can pile-up at the interface between sample top and flat punch, causing local rotations of the crystal

lattice. Consistently, the increase in stress with decreasing diameter follows a Hall – Petch behaviour [14, 15] (Fig. 4 and [16]).

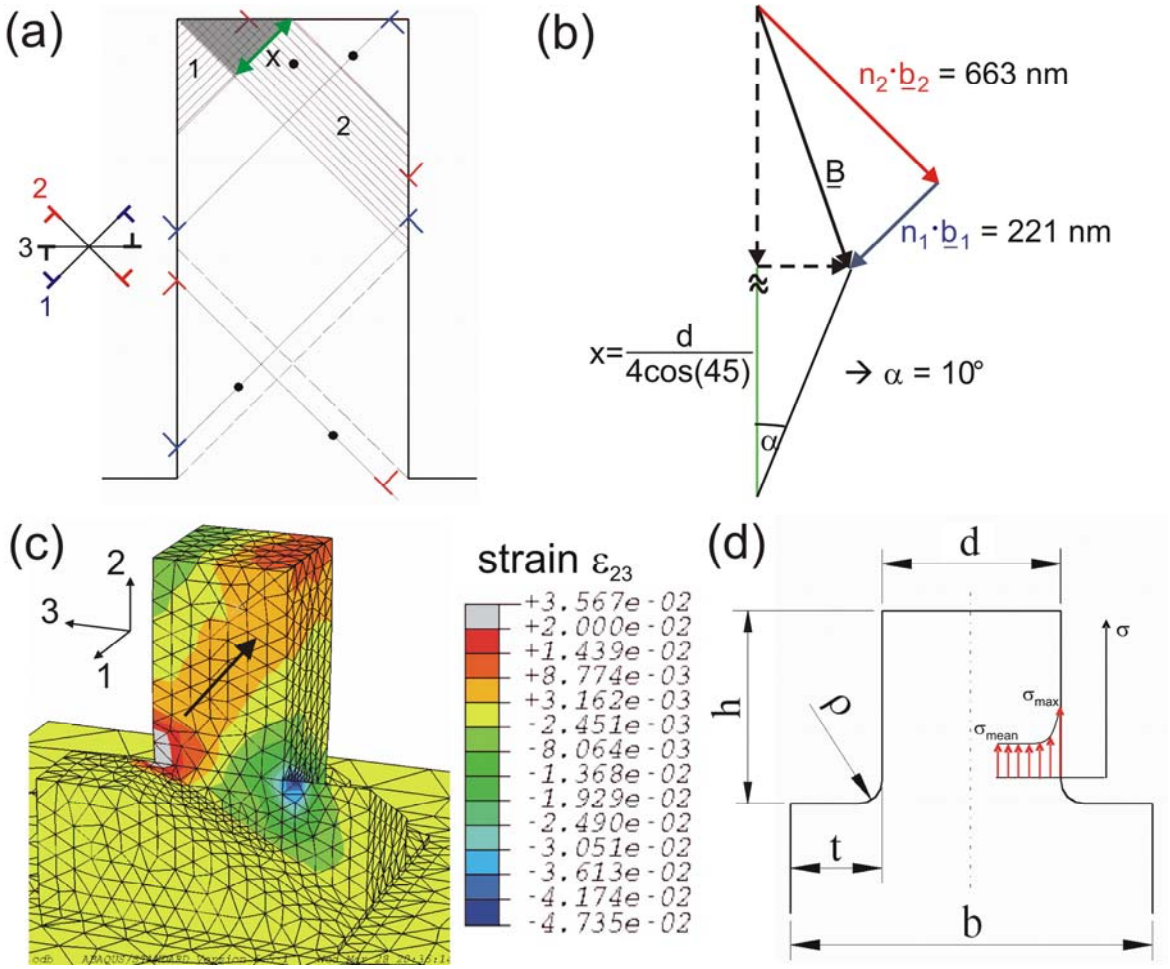

Fig. 6: (a) Two-dimensional model with two sets of glide systems (system 1 with n_1 dislocations with Burgers vector $\underline{b}_1$ and system 2 with n_2 dislocations with $\underline{b}_2$). (b) Net Burgers vector $\underline{B} = n_1 \cdot \underline{b}_1 + n_2 \cdot \underline{b}_2$ leading to a lattice rotation α in the shaded area (along *x* in (a)). See text for details. (c) Linear elastic-plastic three-dimensional FEM calculation of a column with square cross-section. The plastic strain map at φ = 0.2 depicts a zone of strain localization (arrow). (d) Definition of the geometrical quantities influencing the stress concentration factor α_K [19].

Assuming the average length of the pile-up to be *x* (see Fig. 6a), this results in a local lattice rotation of $\alpha \sim 10°$. For symmetry reasons, these dislocation pile-ups are present in each corner, leading to lattice rotations of equal amount but in opposite directions, as observed in the EBSD measurements. The rotation angle

of α ~ 10° is an upper limit compared to the experimentally deduced misorientations of about 5°, since the two-dimensional analogy neglects any dislocation escape, for example during unloading. Additionally, bending stresses evolving during the constrained deformation can activate the horizontal glide system 3, hence reducing the resulting lattice rotations. Furthermore, the dislocation pile-ups exert an increasing back-stress on the operating source, thus increasing the stress necessary to nucleate additional dislocations, until the source is deactivated [17]. At this point of the experiment the deformation is carried on by dislocations emitted from other dislocation sources located close to the bottom of the column (see Fig. 3a and Fig. 5c). In the case of Cu(111) this pile-up situation gets even worse due to the higher inclination angle of the slip planes with the highest Schmid-factor. In principle this effect could be minimized for very long columns, however, this is prevented by buckling. Nevertheless, this constraint can be removed in the future by micro-tension experiments.

Thirdly, the geometry of the columns with square cross-section induces local variations in the specimen stiffness. This is depicted using three-dimensional finite element modelling (FEM) of the investigated geometry with an isotropic linear elastic material with low linear plastic hardening, using J_2 flow theory (neglecting plastic anisotropy). The simulation shows a zone of strain localization at an inclination angle of about 45° with local strains twice the global strain (see Fig. 6c), caused by the specimen geometry, coinciding with a slip plane in the case of Cu(100) columns, but not for Cu(111). Note that no crystal plasticity was applied for this simulation.

Fourthly, there is a constraint due to local stress concentrations present at the edges at the sample base formed during final shaping. These local stresses can be calculated using FEM modelling, but this would require the exact knowledge of the base radius at every position. Due to beam broadening and redeposition inherent to the FIB fabrication method [18], this parameter can only be approximated. Therefore, to estimate the influence of this bottom rounding, the engineering concept of stress concentrations, describing the local stress close to an edge, is used. Solutions for the stress concentration factor α_K depending on

geometry and loading condition are reported in mechanical engineering textbooks, e.g. [19]:

$$\alpha_K = \frac{\sigma_{max}}{\sigma_{mean}} = 1 + \frac{1}{\sqrt{\frac{A}{\left(\frac{t}{\rho}\right)^k} + B\left[\frac{1+\frac{d}{2\rho}}{\frac{d}{2\rho}\sqrt{\frac{d}{2\rho}}}\right]^l + C\frac{\frac{d}{2\rho}}{\left(\frac{d}{2\rho}+\frac{t}{\rho}\right)\left(\frac{t}{\rho}\right)^m}}}. \quad \text{(IV.1)}$$

The maximum local stress σ_{max}, the average global stress σ_{mean}, and the geometry dependent variables *d*, *b*, *t*, and ρ are indicated in Fig. 5d. The constants in Equation (1) depend on the loading condition, and values of A = 0.44, B = 2.0, C = 0.3, k = 0.6, l = 2.2, and m = 1.6 [19]. As already mentioned, sample fabrication started with a pre-form of 10 µm × 10 µm. Therefore, a value of b = 10 µm was chosen, while d was varied between 1 µm and 10 µm. Equation (1) provides an elastic solution for the rotation-symmetric geometry indicated in Fig. 6d. This simple approach provides an estimate of the unwanted edge rounding effect at the base of the pillars with the current sample geometry. Of course, only qualitative conclusions can be drawn. α_K is for the given geometry mainly dominated by the radius of the edge ρ, which is expected to be in the order of several nm, corresponding to the diameter of the ion beam used to shape the micron-sized specimen. For ρ = 10 nm the local stress at the column base can be one order of magnitude higher than the average global stress. The radius of this edge might increase with ongoing plastic deformation or due to a broader ion beam, but even for ρ = 100 nm a stress concentration by a factor four is obtained.

This stress concentration at the sample base in conjunction with the strain localization leads to the different deformation behaviour between rectangular Cu(100) and rectangular Cu(111) compression samples. The stress concentration at the base and the strain localization (Fig. 6c) can be removed by fabricating slightly tapered cylindrical Cu(100) samples. This ensures that the highest stresses occur at the top of the sample, where the cross-section is smallest. However, this increases the aforementioned constraint at the sample top. For the cylindrical Cu(100) samples primary slip was observed to start close to the top of the column, followed by multiple slip at higher strains.

In conclusion, the coinciding resolved shear stresses for Cu(111) and Cu(100) indicate a sufficient amount of available dislocation sources, and the detected misorientations suggest that dislocation pile-up is causing the size effect at this length scale.

5. Summary

The presence of stress concentrations introduced by the specimen geometry in conjunction with the orientation of the single crystal strongly influences the deformation behaviour of miniaturized Cu compression samples. Distinct size effects in the determined flow stress were observed for Cu(111) columns, although a stress concentration is present at the sample base. For Cu(100) samples the size effect vanishes in the presence of a stress concentration at the base, but is observed if these concentrations were minimized by changing the column geometry. A 2-dimensional dislocation model is presented, explaining the experimentally observed lattice rotations. The present study suggests that dislocation pile-up contributes to the compression size effect observed in single crystals.

References

[1] M. D. Uchic, D. M. Dimiduk, J. N. Florando, and W. D. Nix, Science 2004; 305: 986.

[2] D. M. Dimiduk, M. D. Uchic, and T. A. Parthasarathy, Acta Mater. 2005; 53: 4065.

[3] J. R. Greer, W. C. Oliver, and W. D. Nix, Acta Mater. 2005; 53: 1821.

[4] J. R. Greer, W. C. Oliver, and W. D. Nix, Acta Mater. 2006; 54: 1705 [Corrigendum].

[5] C. A. Volkert and E. T. Lilleodden, Phil. Mag. 2006; 86: 5567.

[6] D. Kiener, C. Motz, T. Schöberl, M. Jenko, and G. Dehm, Adv. Eng. Mater. 2006; 8: 1119.

[7] L. Zuo and A. H. W. Ngan, Phil. Mag. Lett. 2006; 86: 355.

[8] T. A. Parthasarathy, S. I. Rao, D. M. Dimiduk, M. D. Uchic, and D. R. Trinkle, Scripta Mater. 2007; 56: 313.

[9] D. Kiener, C. Motz, M. Rester, and G. Dehm, Mater. Sci. Eng. A 2007; 459: 262.

[10] H. Zhang, B. E. Schuster, Q. Wei, and K. T. Ramesh, Scripta Mater. 2006; 54: 181.

[11] S. Scheriau, Diploma Thesis, Institute of Metal Physics, University of Leoben 2006.

[12] T. Hebesberger, H. P. Stüwe, A. Vorhauer, F. Wetscher, and R. Pippan, Acta Mater. 2005; 53: 393.

[13] D. Raabe, D. Ma, and F. Roters, Acta Mater. 2007; 55: 4567.

[14] E. O. Hall, Proc. R. Soc. Lond. 1951; B64: 747.

[15] N. J. Petch, J. Iron Steel 1953; 174: 25.

[16] D. Kiener, M. Rester, S. Scheriau, B. Yang, R. Pippan, and G. Dehm, Int. J. Mat. Res. 2007; 98: in press.

[17] L. H. Friedman and D. C. Chrzan, Phil. Mag. A 1998; 77: 1185.

[18] L. A. Giannuzzi and F. A. Stevie, *Introduction to focused ion beams* (Springer, New York, 2005).

[19] W. Beitz and K.-H. Grote, *Dubbel Taschenbuch für den Maschinenbau* (Springer, Berlin Heidelberg New York, 1997).

V A further step towards an understanding of size-dependent crystal plasticity: *In-situ* tension experiments of miniaturized single crystal copper samples (Publication D)

D. Kiener, W. Grosinger, G. Dehm, and R. Pippan

Acta Materialia (2007), accepted.

ABSTRACT

A method for *in-situ* testing of miniaturized tension specimen was developed. The size effects of the plastic deformation behaviour of copper single crystals loaded along the <-2 3 4> direction were investigated. The diameter was varied between 0.5 µm and 8 µm, and the aspect ratio, gauge length to side length, between 1:1 and 13.5:1. At high aspect ratios hardening was negligible. However, an increase of the flow stress with decreasing diameter was observed. This increase was small for diameters above 2 µm, and somewhat larger below 2 µm. These findings are explained by individual dislocation sources which govern the plastic deformation. For low aspect ratios the behaviour is significantly different. A pronounced hardening and a very strong size effect was observed. Both are a result of dislocation pile-ups due to the constrained glide of the dislocations caused by the sample geometry.

1. Introduction

In the past few years, the deformation of miniaturized single crystal samples is frequently investigated to examine the processes governing deformation on the micrometer and nanometer length scale. The employed testing methods differ significantly in the stress state of the tested volume. Uchic et al. [1] developed a method to fabricate miniaturized compression samples using a focussed ion beam (FIB) microscope and loaded these columns using a nanoindenter equipped with a flat diamond tip. With this approach, most of the constraints present, for example, in nanoindentation experiments, were removed and the sample was exposed to a nominally uniaxial stress and strain state. The key result of these miniaturized compression experiments was an unexpected size effect in terms of an increased flow stress with reduced sample diameter. The nature of this effect is still under discussion. Nevertheless, this method had to deal with problems due to constraints rising from friction, the limited sample aspect ratio in order to prevent buckling, and the compliance of the sample base. Further uncertainties are induced from the alignment between the sample and the indenter [2].

In the macroscopic world, tension experiments offer several benefits when compared to compression tests. For example, there is almost no limitation to high aspect ratios. In the microscopic world, problems arise due to the difficulties of sample fixation. Therefore, we developed a method to fabricate miniaturized tension samples and individually designed indenter tips serving as tensile sample holders using a FIB, giving us the possibility to systematically investigate the origin of mechanical size effects in the micron and sub-micron regime. Furthermore, loading of the tension samples was performed *in-situ* using a microindenter mounted in a scanning electron microscope (SEM). Beside high accuracy in local positioning, this approach also provides insight into the deformation process.

In the present manuscript we investigate the tensile deformation of single crystal copper specimen. The influence of sample size and aspect ratio on the plastic deformation behaviour is observed *in-situ* in the SEM and correlated to the measured stress-strain curves. The aim of this study is to improve knowledge of the geometrical aspects governing mechanical properties in the micrometer and sub-micrometer regime.

2. Experimental

Rods with dimensions of 20 mm × 0.5 mm × 0.5 mm were cut from a copper single crystal using a diamond wire saw, in a way so that the <-2 3 4> crystal direction is aligned with the length axis of the samples. These rods were mounted on copper holders to simplify further handling and to ensure accurate alignment for the FIB shaping and the following mechanical testing. Subsequently, these rods were electrolytic polished in phosphoric acid to remove the deformation layer from the cutting process. Additionally, the sample was shaped in the form of a needle with an opening angle of ~30° and a tip radius in the order of several micrometers. This was achieved by moving the samples periodically in and out of the electrolyte. An example of such a needle is presented in Fig. 1a. Tension specimen were prepared from these needles by ion milling, using a FIB (Zeiss 1540 XB) with a Ga^+ ion source operated at an acceleration voltage of 30 kV under perpendicular ion impact, as displayed in Fig. 1b-d. For this purpose, in a first step two parallel sides were coarse shaped with an ion current of 1 nA (Fig. 1b). Then the sample holder was rotated by 90° around the length axis of the needle and the other two sides were cut from the lamella produced in the first step (Fig. 1c), the applied ion current for coarse milling was again 1 nA. The final shaping to the desired dimensions was performed with an ion current of 100 pA in order to reduce the ion induced damage [3]. Subsequently, the sample was rotated back to the initial orientation for the final shaping of these two sides (Fig. 1d), again using an ion current of 100 pA. This was necessary to ensure that redeposition during the second milling step does not influence the desired sample dimensions or mechanical properties. For the investigated samples, the <-2 3 4> axis of the single crystal was parallel to the loading direction, side lengths, *a,* ranging from 0.5 µm to 8 µm, and aspect ratios defined as gauge length/side length between 1:1 and 13.5:1.

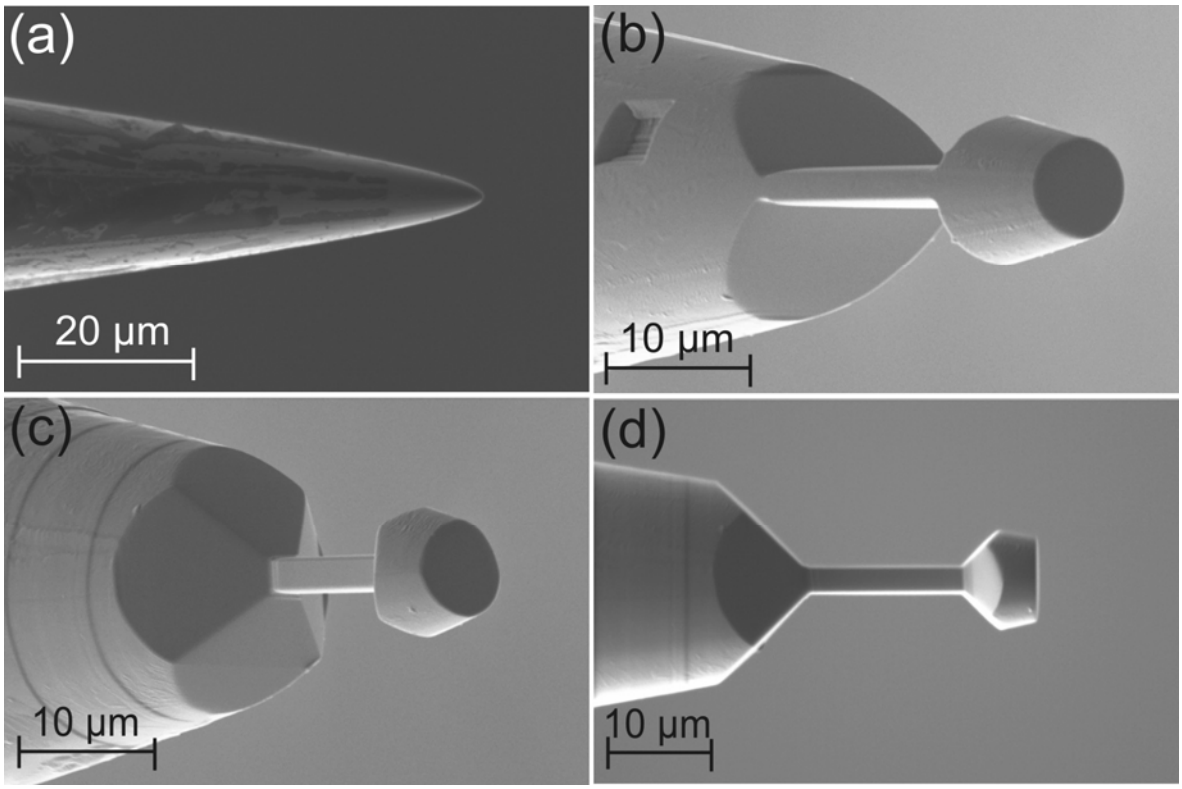

Fig. 1: (a) Single crystal copper needle with <-2 3 4 > crystal direction along the length axis after electrolytic thinning. (b) FIB milling of first two parallel side planes. (c) Shaping of the other two perpendicular side planes after rotating the sample by 90° around the length axis. (d) Final shape of a tension sample with a side length *a* = 3 µm and an aspect ratio of 5:1. Note that (b, c) are inclined views.

Immediately after FIB milling was finished, tensile testing was conducted under vacuum conditions (vacuum pressure ~$2 \cdot 10^{-6}$ mbar) to avoid the formation of extensive oxide layers on the sample surface. The time the specimens were exposed to humid air was kept below a few minutes. This time was necessary to vent the FIB chamber, manipulate and transport the specimen between the different devices, and evacuate the SEM chamber. The samples were loaded using a microindenter (ASMEC UNAT) mounted inside an SEM (LEO Stereoscan 440). This indenter was equipped with special dove tail shaped tips serving as sample gripper to ensure form-closed connection between sample and indenter. These grippers were fabricated from polycrystalline tungsten needles, which are usually employed in micromanipulators, again by FIB machining. Differently sized grippers were used for the differently sized tension samples to ensure that there is sufficient contact area between sample head and sample gripper when using self-

similar specimen. An example is shown in Fig. 2a, presenting an SEM image of the same sample as shown in Fig. 1 along with the corresponding sample gripper. A major advantage of the employed *in-situ* setup is the highly precise alignment, enabled by direct visual control. Otherwise it would be impossible to perform the 4-axis operations necessary to position the tension sample in a way that the flanks of the sample head are parallel and equally spaced from the flanks of the sample gripper, as illustrated in Fig. 2b. It is acknowledged that there is an uncertainty in the alignment of the rotation axis of sample and gripper in the z-direction. By knowing the dimensions of the gripper, this can be adjusted with an accuracy of ±1 µm. Therefore, we do not expect that out-of plane loading of our specimen will influence our results.

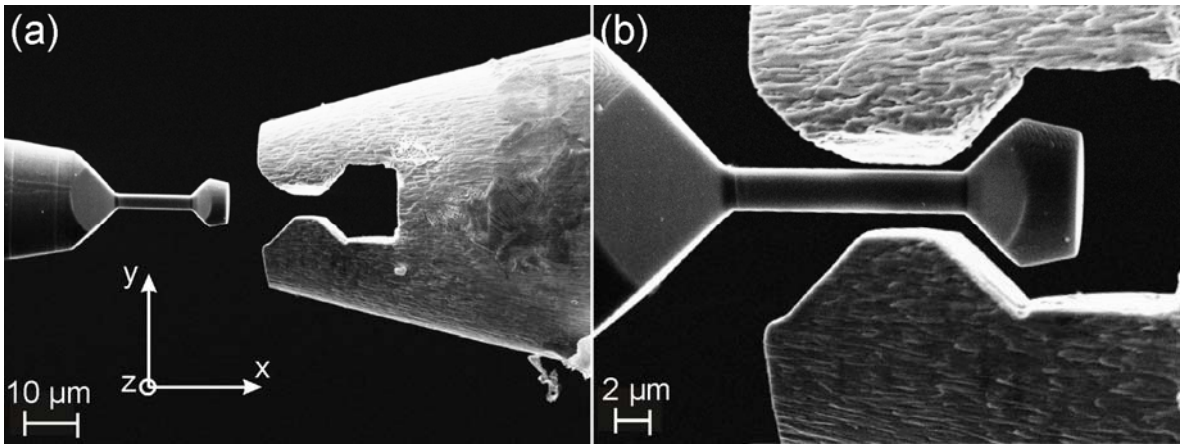

Fig. 2: (a) SEM image showing a single crystal copper tension sample and the corresponding tungsten sample gripper before the test at a low magnification. (b) Sample and gripper aligned prior to loading. The loading direction is along <-2 3 4>.

The samples were loaded in open displacement controlled mode to engineering strains larger than 15%. During tensile testing, load and displacement were measured. Furthermore, sequences of SEM images were recorded and analyzed together with the load-displacement data.

3. Results

3.1 Method

Fig. 3a shows the load-displacement data collected for the tension sample with *a* = 3 µm and an aspect ratio of 5:1. Positioning of the tension sample was conducted in a way such that there was always a small slit in the order of one micron between the flanks of sample and the gripper. This is to prevent any contact before loading. Therefore, the graph shows a regime without load where the sample gripper approaches the sample. The noise present in this regime gets significantly reduced once the sample and the gripper are in full contact in the regime of linear loading, as can be seen in the inset in Fig. 3a. Beside a serration like behaviour, the load-displacement curve exhibits several pronounced load drops, corresponding to the appearance of distinct glide steps during *in-situ* monitoring. Furthermore, it is obvious from this data as well as the *in-situ* observation that despite all taken effort the contact between the sample and the gripper flanks is not perfect and there is a region of surface adaptation before the linear loading regime.

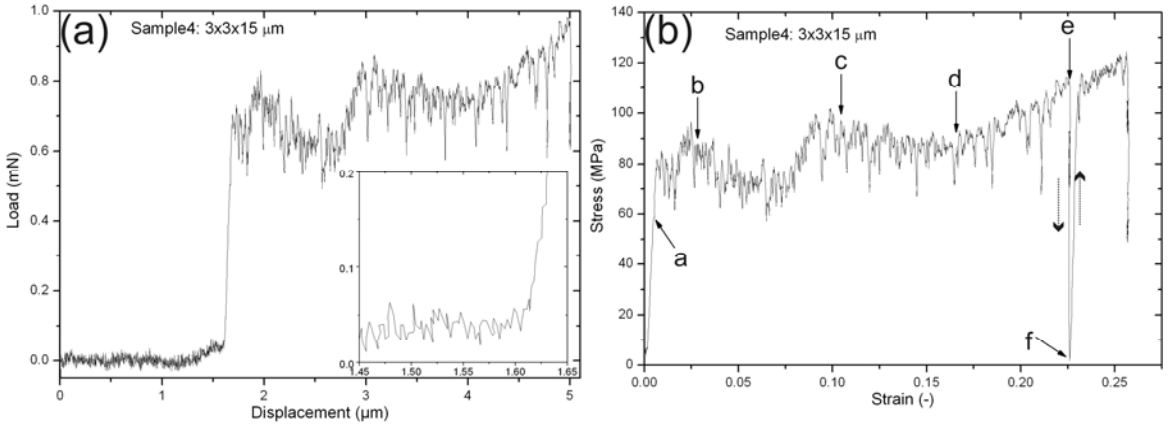

Fig. 3: (a) Load-displacement curve measured for the first loading of the sample depicted in Fig. 2. The inset shows details of the measured curve just before full contact between the sample and the gripper is established. (b) Stress-strain curve calculated from the load-displacement data. A second loading step (indicated by dotted arrows) performed for this sample is included in the graph but not shown in Fig. 3a. See text for details.

To calculate technical stress-strain curves from the load-displacement data, the load was simply divided by the initial cross-section determined after final shaping of the sample in the FIB. To calculate strains, the linear loading regime was extrapolated to intersect the axis of abscissae and the contact-free part of the load-displacement curve (including the surface adaptation regime) was omitted. The corresponding stress-strain curve calculated from the load-displacement data of Fig. 3a is presented in Fig. 3b. After unloading, this sample was reloaded a second time (dotted arrows in Fig. 3b). Two important aspects shall be mentioned. First, the reload starts with a linear regime. Second, upon reloading the flow curve continues from the stress level where it ended before unloading. This statement holds true for the load-displacement curves of all further loading steps, indicating that the contact sites were already adapted after the first loading.

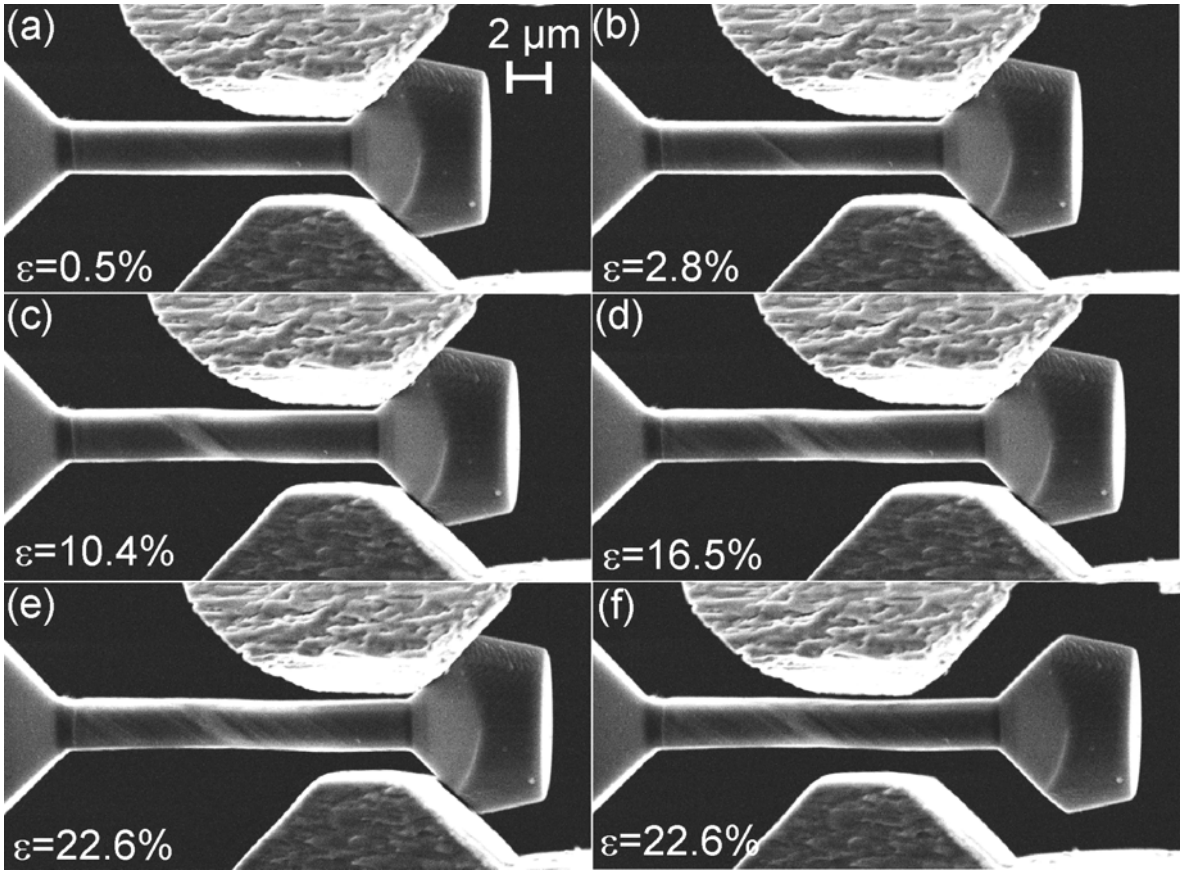

Fig. 4: SEM images of the sample shown in Fig. 2 taken during *in-situ* tensile testing (a-e) and after unloading (f). The corresponding positions along the stress-strain curve are indicated by arrows in Fig. 3b.

Fig. 4 shows in a series of SEM images the formation of distinct glide steps first in the centre of the sample (Fig. 4b), and finally along the whole gauge length (Fig. 4c-e). The corresponding positions along the stress-strain curve are indicated by arrows in Fig. 3b. Fig. 4f shows the sample and the gripper after unloading.

3.2 Geometrical constraints

To investigate the influence of the gauge length, we fabricated samples with *a* = 3 µm and an aspect ratio of 5:1. These were confined in the middle of the gauge length to dimensions of 1.5×1.5×8 µm, 1.5×1.5×1.5 µm with an opening angle of the flanks of 45°, and 1.5×1.5×1.5 µm with an opening angle of 90°, respectively. SEM images of these samples taken during *in-situ* tensile testing are shown in Fig. 5.

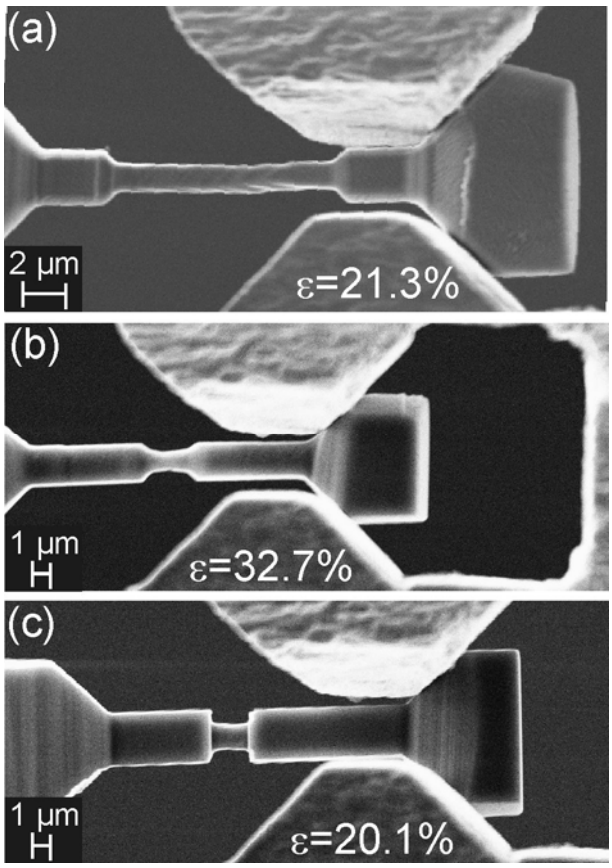

Fig. 5: SEM images taken during *in-situ* loading of miniaturized copper tension samples with *a* = 1.5 µm and aspect ratios of (a) 5:1 and (b, c) 1:1, respectively. To further constrict deformation for the samples with an aspect ratio of 1:1, the flank angle was changed from (b) 45° to (c) 90°.

While the unconfined sample with the high aspect ratio of 5:1 (Fig. 5a) shows pronounced glide steps distributed over the whole sample length, these features are strongly reduced in the case of the confined samples with an aspect ratio of 1:1. Whereas in the case of the 45° flanks (Fig. 5b) some glide steps are visible, they are even less distinct for the sample with the 90° flanks (Fig. 5c).

The corresponding stress-strain curves shown in Fig. 6 reflect this observation, with the flow stresses of the confined samples being significantly higher than the unconfined one (roughly by a factor between 2 and 3). Furthermore, the confined sample with the 90° flanks displays higher stress levels than the confined sample with the 45° flanks. It is acknowledged that the initial loading slopes of the three samples are different, with the most constrained sample having the lowest slope. This aspect will be further discussed in the Appendix.

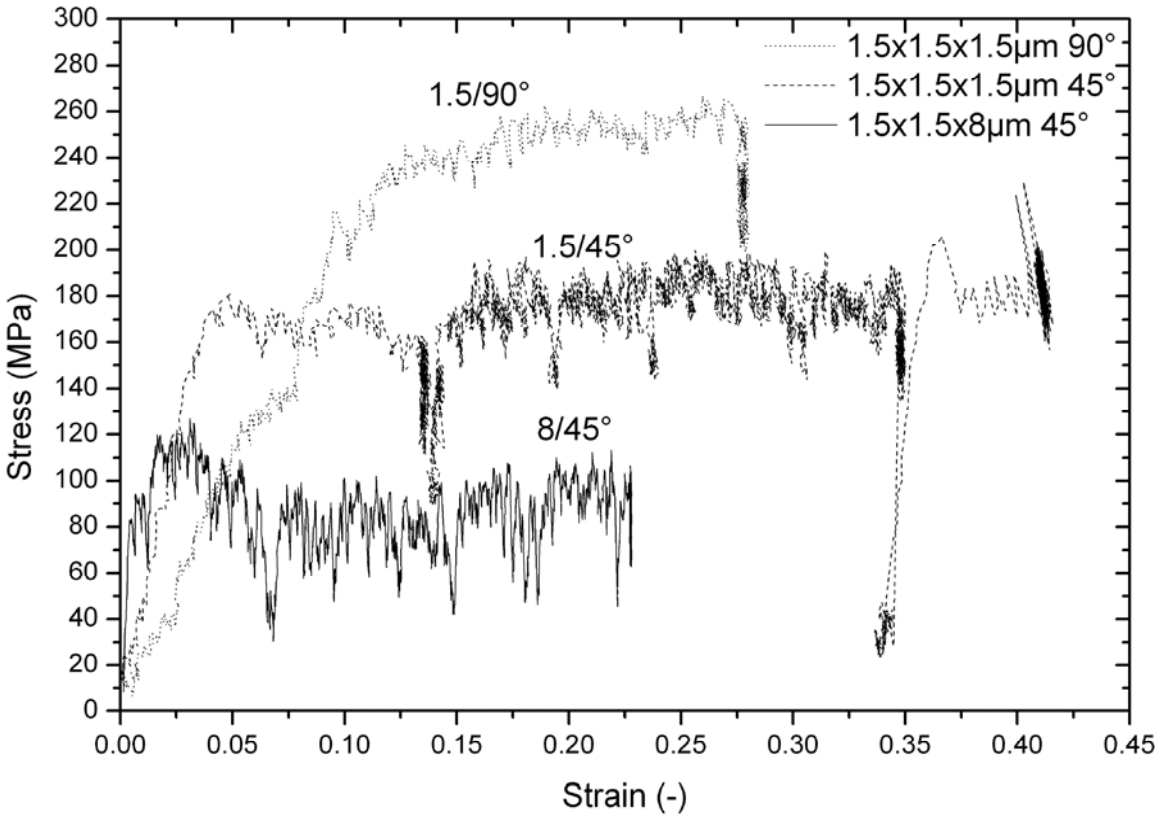

Fig. 6: Stress-strain curves measured for the samples displayed in Fig. 5. Strong influence of the geometrical confinement on the mechanical behaviour is present, with the geometrically more constricted samples showing significantly higher flow stresses.

3.3 Pre-straining

The influence of pre-straining on the mechanical response was investigated in a further experiment. Therefore, a sample with *a* = 8 µm and an aspect ratio of 5:1 was strained to 5.4 % (Fig. 7a, b). Subsequently, the specimen was reduced by FIB milling to *a* = 3 µm over the whole sample length, resulting in an aspect ratio of 13.5:1. This sample was afterwards again loaded to strains above 10 %.

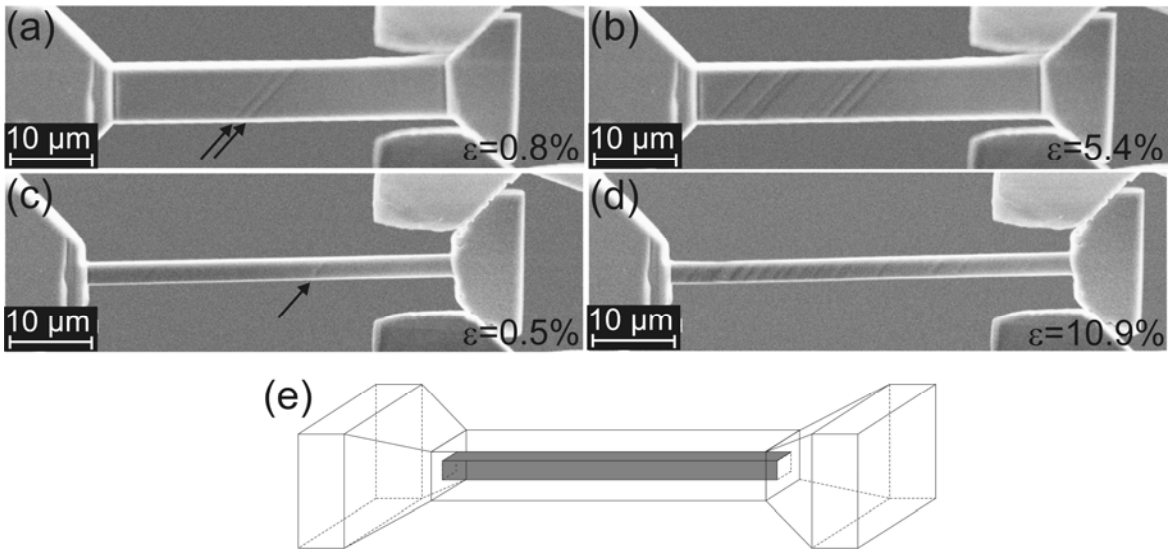

Fig. 7: SEM images taken during *in-situ* tensile testing of a sample with *a* = 8 µm (a, b). After straining to 5.5 %, this sample was FIB machined to *a* = 3 µm and loaded again (c, d). First emerging glide planes are indicated by arrows. A schematic of the specimen reduction is presented in (e).

The stress-strain curves of these two samples are shown in Fig. 8. The smaller, pre-strained sample exhibits a higher stress to initiate deformation. At higher strains, the stress levels are not far apart. In both cases, deformation in terms of visible glide steps started near the sample centre (see arrows in Fig. 7a, c) and expanded along the gauge length.

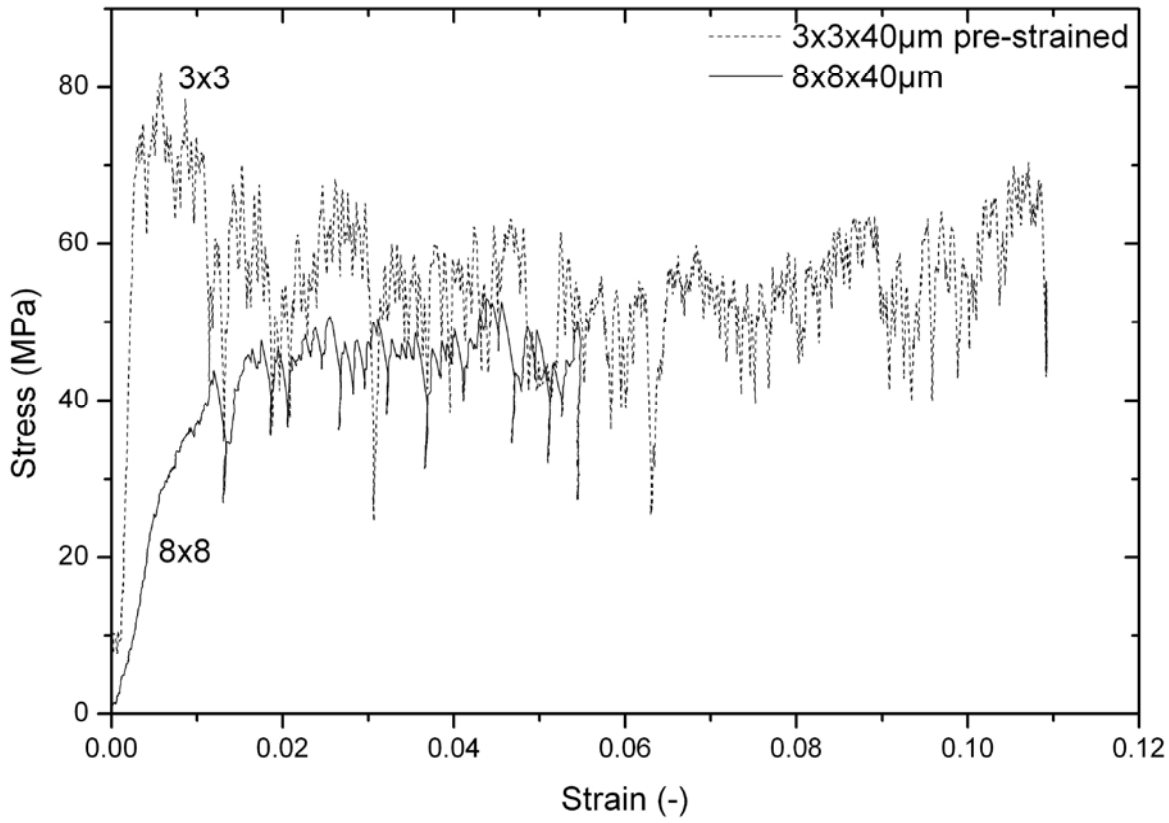

Fig. 8: Stress-strain curves of the 8×8×40 µm sample depicted in Fig. 7a, b, and the 3×3×40 µm sample FIB milled from this already strained specimen, depicted in Fig. 7c, d.

3.4 Size effects

Finally, the technical stress-strain curves of all samples discussed in this investigation are shown in Fig. 9. There is no significant hardening found for the samples with an aspect ratio of 5:1 or higher, while the sample with a = 8 and an aspect ratio of 1:1 exhibits significant hardening.

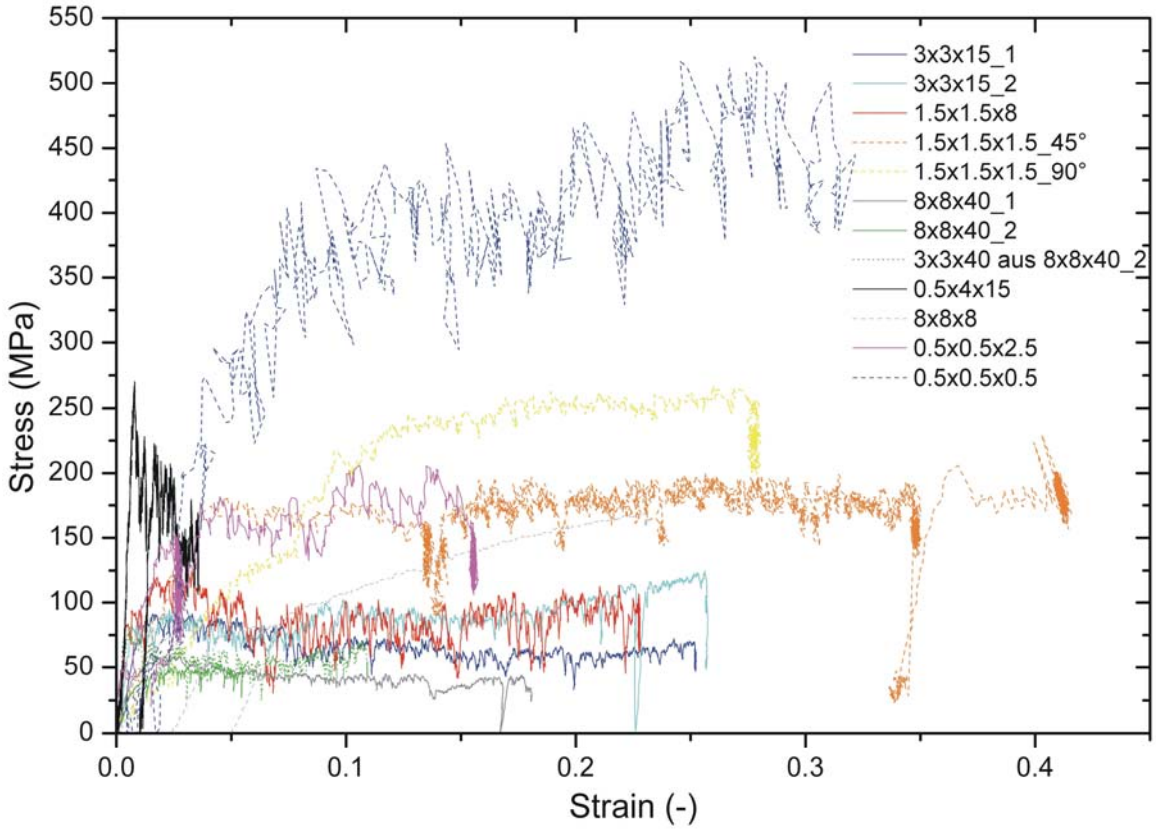

Fig. 9: Technical stress-strain curves of miniaturized single crystal copper tension samples loaded along the <-2 3 4> crystal direction. Full lines indicate an aspect ratio of 5:1, dashed lines reflect an aspect ratio of 1:1, and a dotted line indicates a pre-strained specimen.

In order to give an overview and ease comparison to other investigations, the size-dependent flow stress at 10 % strain is shown in Fig. 10. The open symbols reflect samples with an aspect ratio of 5:1, while the filled symbols correspond to samples with an aspect ratio of 1:1. As indicated in Fig. 7e the pre-strained sample with a = 3 µm and an aspect ratio of 13.5:1 was fabricated from a tested sample with a = 8 µm and an aspect ratio of 5:1. The two corresponding data points are marked by an arrow. Furthermore, this thicker sample serving as pre-form was strained to only 5.5 % (Fig. 8). Therefore, the stress at 5 % strain is included in Fig. 10. The magnitude of the error bars will be discussed in the Appendix.

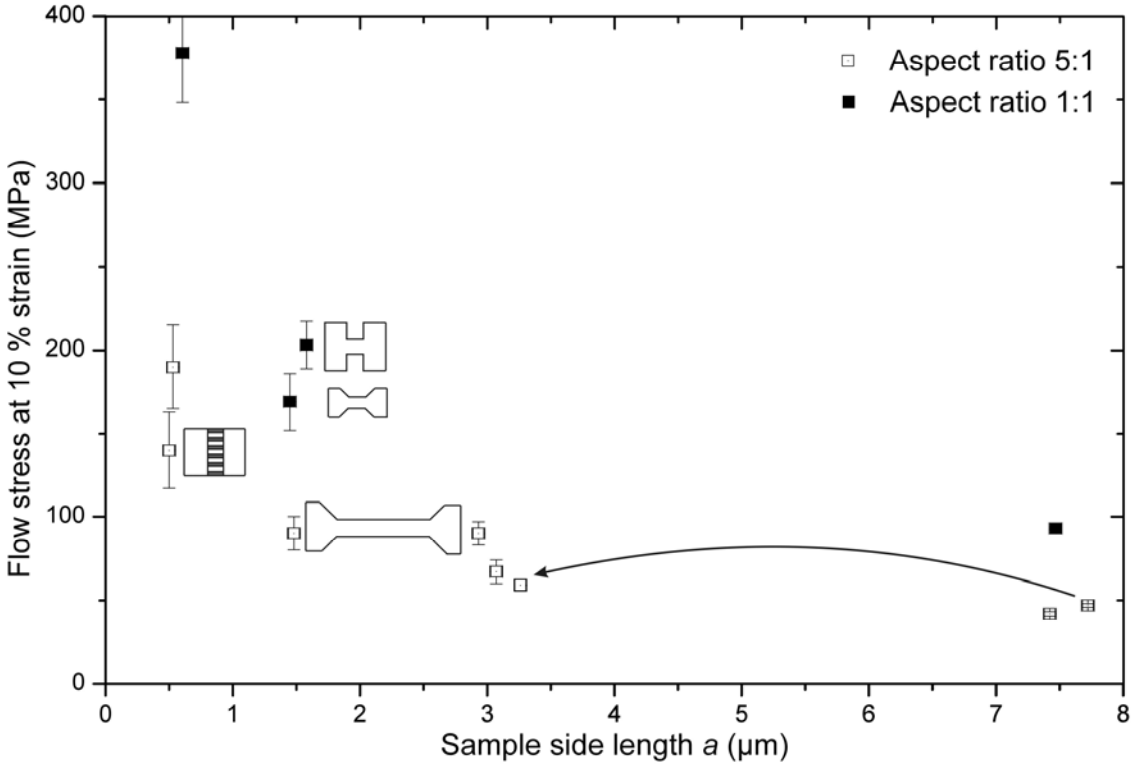

Fig. 10: Size-dependent technical flow stress of miniaturized copper tension specimen loaded along the <-2 3 4> direction at a strain of 10 % extracted from Fig. 9. For several samples the error bars are smaller than the used symbol. See text for details.

4. Discussion

The experimental challenges and factors affecting such miniaturized tension experiments are discussed in the Appendix. In this section the attention is mainly focussed on the plastic flow behaviour of the miniaturized single crystal tension samples.

4.1 High aspect ratios (5:1 and higher)

The presented images taken from the *in-situ* experiments showed that slip takes place in clearly defined planes throughout the whole sample. This is also depicted in the high resolution SEM image taken after deformation of the sample displayed in Fig. 4. Despite the high total strain of more than 25 %, there is only one type of glide steps visible on the surface (see Fig. 11a). Furthermore, no indication of necking was found, supporting the assumption of single slip deformation. To

further confirm the finding of single slip, the local crystal orientations were investigated using EBSD.

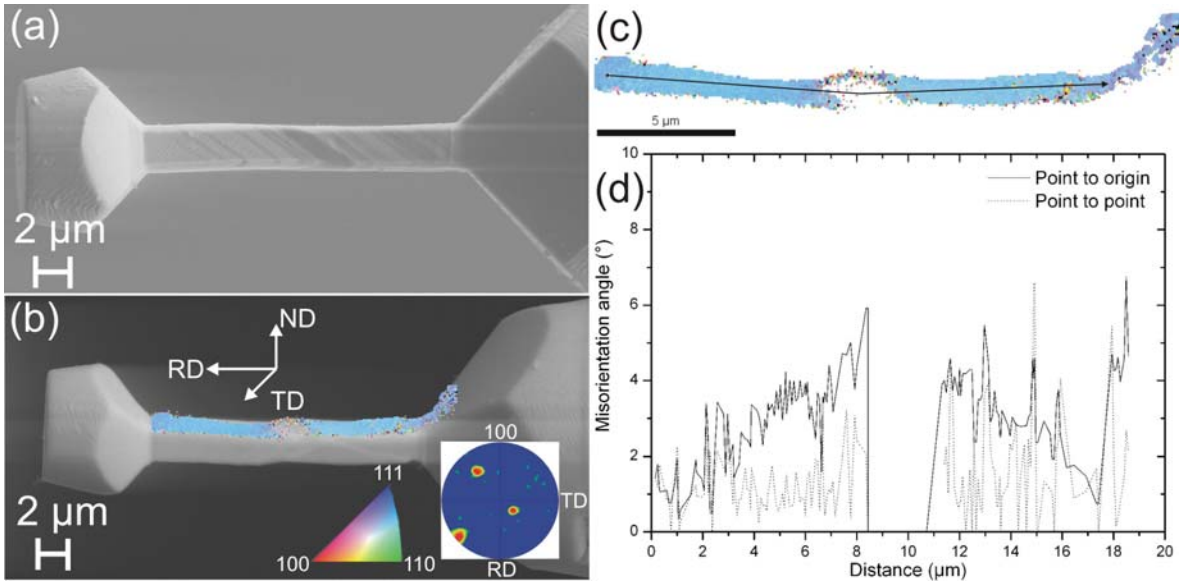

Fig. 11: (a) High resolution SEM image presenting the deformed tension sample of Fig. 4. Only one set of glide steps is visible. (b) EBSD scan indicating the local crystal orientation in transverse direction (TD) along the sample. The insets present the applied colour code and the (1 0 0) pole figure calculated from the EBSD data. (c) Higher magnified EBSD data. (d) Misorientation profile along the path shown in (c). See text for details.

Fig. 11b presents an inclined view of the sample with an overlay indicating the local crystal orientation in transverse direction (TD). The insets represent the applied colour code and the (1 0 0) pole figure calculated from this data, respectively. No peak broadening or streaks were observed. The higher magnified EBSD scan (Fig. 11c) depicts no distinct misorientations. The zone in the centre of the sample could not be measured due to shadowing effects. A misorientation profile along the sample length, calculated with respect to the starting point of the profile, indicated in Fig. 11c, shows a slight rise in misorientation from ~0.5° (which is the accuracy of the system) at the left end of the sample to ~5° at the sample centre. Following the region without measured orientations, this value decreases down to ~0.5° again and rises slightly when approaching the sample flanks. These misorientations stem from the global deformation of the sample. No gradients in misorientation corresponding to a pile-up of dislocations or storage of dislocations during deformation [4] were found in the gauge length.

The fact that single slip takes place over the whole sample length leads to the conclusion that a number of single sources controls the plastic flow. Each source is responsible for a certain plastic deformation or induces an avalanche on the corresponding slip plane, subsequently followed by the activation of the next source. It is supposed that this change takes place as a consequence of the redistribution of local stresses, mainly because the fixed sample ends can cause a local bending stress. No significant hardening except the serration like behaviour was observed. This implies that there is no building up of forest dislocations.

The measured flow stress is significantly lower than in other small scale experiments (compression [1, 5], bending [4, 6], indentation [7, 8] …). Nevertheless, a size-effect is observed with the flow stress at 10 % strain rising from ~40 MPa for a = 8 µm to ~170 MPa for a = 0.5 µm.

Assuming that the source size determines the flow stress, we can calculate this source size from the measured stresses by applying [9]:

$$\tau_{\text{source}} = \frac{Gb}{2\pi} \cdot \frac{1}{S} \cdot \ln\left(\frac{\alpha \cdot S}{b}\right), \tag{V.1}$$

where G = 47 GPa is the bulk modulus, $b = 2.56 \cdot 10^{-10}$ m is the Burgers vector, S is the length of the source, and α is a numerical constant in the order of unity. This equation is valid for a Frank-Read source with size S (the U-mill following the nomenclature by Orowan [10]) or a single ended source with size $S/2$ (the L-mill) [11].

The result of these calculations is depicted in Fig. 12a for an L-mill. τ_{source} was obtained by converting the flow stresses at 1 % strain to shear stresses by assuming glide on the {1 1 1} plane with the highest Schmid factor $m_{\text{-2 3 4}}$ = 0.422 for the given configuration. An increase in source size from S_L ~ 500 nm for a = 0.5 µm to S_L ~ 2000 nm for a = 8 µm is observed (Fig. 12). The effect of image forces from the free surface is negligible in these dimensions and was therefore not taken into account.

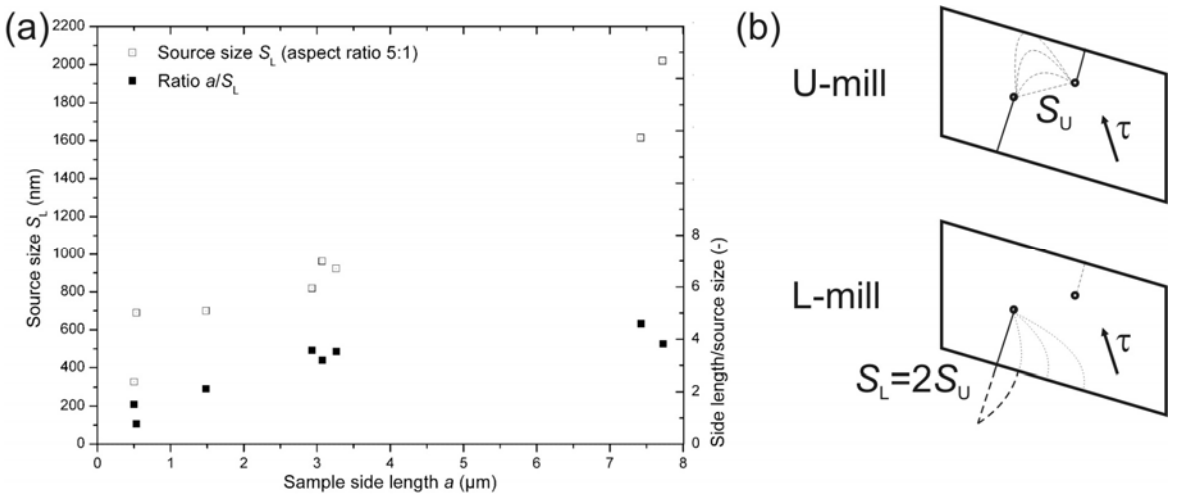

Fig. 12: (a) Calculated dependence of source size S_L and ratio a/S_L on the sample side length a for a L-mill using Equation (2). (b) Schematic view on the glide plane of a tension specimen showing the first operation of a U-mill and the subsequent operation of the longer arm of the generated L-mill.

To understand why the sample size should dominate the source size, one has to consider the glide geometry of the investigated specimen as schematically depicted in Fig. 12b. Every U-mill will end up as two L-mills after first activation [12]. Therefore, we assume this type of dislocation source to be the typical deformation mechanism in our experiments. As our glide planes have a rectangular shape, there is a periodic variation of the source length. The flow stress is hence determined by the minimal source length, which scales with the sample diameter. There must not necessarily be a U-mill present in the sample to generate the L-mill, also the partial removal of an initial dislocation source during FIB milling produces a single dislocation arm, which can operate in the depicted way.

Furthermore, during operation the free dislocation end will periodically not only change in length but also in character between edge and screw. The difference in line energy between screw dislocation and edge dislocation is given by [13]:

$$E_{\mathrm{L,edge}} = \frac{E_{\mathrm{L,screw}}}{1-\nu}. \qquad \text{(V.2)}$$

Additionally, if the penetration point of the dislocation on the surface is of edge character, lattice relaxation takes place in this area, resulting in an additional pinning force on the dislocation end, leading to an extra curvature of the dislocation line.

Finally, there is a stress contribution, σ_{ledge}, due to the ledge formation energy of the screw dislocation emerging on the surface, which is dependent on the sample size in an inverse manner [14]:

$$\sigma_{\text{ledge}} = \frac{1}{m} \cdot \tau_{\text{ledge}} = \frac{1}{m} \cdot \frac{2\gamma}{a}, \tag{V.3}$$

where γ = 1.69 J·m^{-2} is the surface energy of copper [14], m = 0.422 is the Schmid factor, and a is the sample side length.

For sample side lengths of 0.5 µm, 1 µm, and 2 µm this leads to a σ_{ledge} of 16 MPa, 8 MPa, and 4 MPa, respectively. This is a small contribution in the investigated regime, but becomes important upon further decrease of the specimen size.

There are other aspects like the presence of an oxide layer or the FIB damaged layer to be considered. However, we do not expect them to have a significant effect on the plastic flow behaviour, as in that case the stress should drop significantly after this layer is cut by the first emerging glide step. This was not observed in our experiments. Furthermore, if a layer would be present one would expect the deformation to continue on the plane where this layer was broken. Contrary, our samples showed several distinctive glide steps (Fig. 13a). A schematic of this cutting process is presented in Fig. 13b. Note that the thickness of the oxide layer/FIB damaged layer is overdrawn. Detailed investigations on the FIB damaged layer and possible mechanical consequences are reported elsewhere [3]. Fibre tensile testing experiments of electrolytically thinned copper wires with diameters ranging from 50 µm down to 15 µm report flow stresses for the smallest wire which are in good agreement with our data [7].

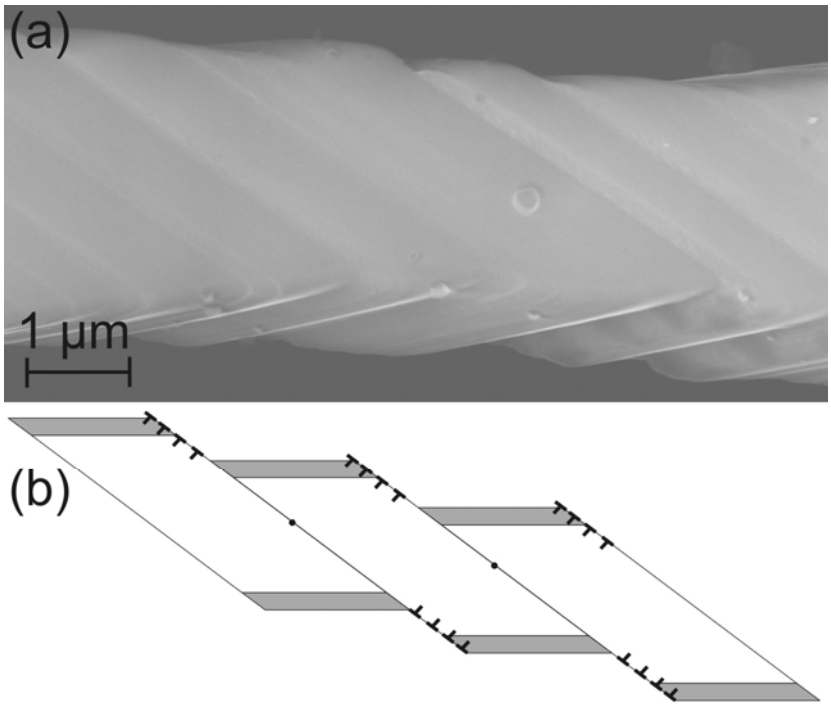

Fig. 13: (a) High resolution SEM image of a tension sample with *a* = 3 µm and an aspect ratio of 5:1 taken after a deformation of 25.1 %. Distinct glide steps are visible on the sample surface. (b) Schematic demonstrating the negligible effect of an oxide or FIB damaged layer on the flow stress after emerging of large glide steps.

Comparison of our results with tension experiments of bulk single crystal copper shows that the observed stresses are higher than the orientation dependent stresses between 1 and 2 MPa reported by Diehl [15] for stage I deformation of macroscopic single crystal copper. Whether this difference stems from different dislocation densities, impurity contents, the presence of pre-existing forest dislocations, or the “constrained” tension experiment (our sample gripper suppresses movement of the tension sample in the y-direction [15]), is not clear and subject to further investigations.

4.2 Low aspect ratio (1:1)

When performing macroscopic tensile tests, a reduction of the aspect ratio causes a small increase of the flow stress due to the development of a multiaxial stress state, like in the neck of a long tensile sample. In the case of the miniaturized tension samples, a significant effect on the flow stress is observed, which is more

pronounced than for the samples with high aspect ratio. Furthermore, these samples exhibit strong hardening contrary to the samples with high aspect ratio.
The inclination angle of the glide plane in combination with the chosen sample geometry prevents simple glide of the dislocations over the sample cross-section (Fig. 14a). Therefore, the dislocations glide into the shoulder of the tension samples (Fig. 14b). The cross-section in this shoulder region increases significantly, reducing the shear stress approximately by an order of magnitude for the sample with 90° shoulders, and by the equations given in Fig. 14b in the case of 45° shoulders. Thus, the shear stress rapidly drops below the level necessary to move dislocations. Consequently, pile-ups form at the end of the tension samples. These pile-ups were confirmed by EBSD scans showing distinct misorientations.

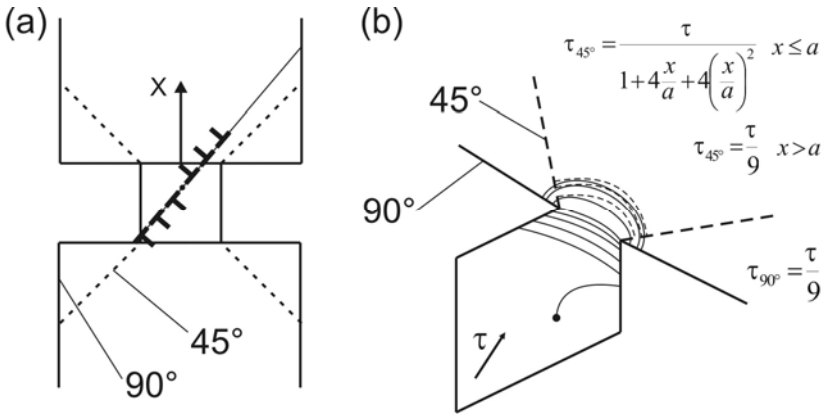

Fig. 14: (a) Schematic of the tension samples indicating that no free glide plane exists. (b) View on the glide plane showing the pile-up emerging for both geometries. The provided equations give the shear stress present in the shoulder part of the tension sample for the 45° geometry ($\tau_{45°}$) and the 90° geometry ($\tau_{90°}$), respectively.

The required number of edge type dislocations Δn in a pile-up to reach the measured stress levels with respect to the sample with an aspect ratio of 5:1 can be estimated as [13]:

$$\Delta n = \frac{L(1-\nu)}{Gb} \cdot \Delta\tau \,, \tag{V.4}$$

where L is the length of the pile-up, which was assumed to be half the glide plane length, ν = 0.28 is Poissons ratio, and $\Delta\tau$ the rise in shear stress.

Regarding the sample with a = 8 µm, taking $\Delta\tau_{8,\,45°}$ ~30 MPa leads to a number of $\Delta n_{8,\,90°}$ ~ 27 dislocations in the pile-up. The sample with a = 1.5 µm and the 45° flanks exhibited $\Delta\tau_{1.5,\,45°}$ ~ 85 MPa, resulting in $\Delta n_{1.5,\,45°}$ ~ 15. At sufficiently high applied stresses, the dislocations can glide through the inclined shoulder part of the tension sample (Fig. 5b) to accomplish the given deformation. To further hinder this deformation, the cross-sectional area of the shoulder part of the sample was increased using the 90° flanks (Fig. 5c), therefore further lowering the stresses present in the sample heads. Consequently, higher flow stresses were determined for this sample. Taking a value of and $\Delta\tau_{1.5,\,90°}$ ~ 160 MPa evaluates $\Delta n_{1.5,\,90°}$ ~ 30. Notably, a similar number of dislocations is required in the pile-up of tension samples with a = 1.5 µm and a = 8 µm, but is confined to a shorter glide plane length for the smaller specimen. This causes an increasing back-stress on the operating sources, explaining the high flow stress values. From the current understanding, this system should exhibit continuous hardening. Nevertheless, in the experiments a plateau value is reached for the small samples. A possible explanation for this behaviour is cross-slip of dislocations [16], but to confirm this assumption, further investigations are required.

It is interesting to compare the present results to micro-compression testing. For example, single crystal copper columns with an <1 1 1> surface normale and a fixed apect ratio of 2:1 have been compressed using the same *in-situ* setup. Flow stresses from ~280 MPa to ~870 MPa were determined for diameters ranging from 8 µm to 1 µm at a strain of 20 % [17]. Similar strong size effects have also been reported for single slip oriented materials, see for example [1]. These values [1, 17] are significantly higher than those found in our miniaturized tensile tests for samples with high aspect ratios. We therefore speculate that the constraints in the deformation by the flat punch and the underlying substrate result in the formation of extensive dislocation pile-ups, which become responsible for the high flow stresses observed in micro-compression testing.

5. Summary & Conclusions

– A method to perform *in-situ* tensile testing of miniaturized specimen was developed. This provides the possibility to remove several dimensional constraints present in miniaturized compression testing.

– Single crystal copper tension samples with diameters ranging from 0.5 µm to 8 µm and aspect ratios between 1:1 and 13.5:1 were loaded along the <-2 3 4> direction and a size dependence of the flow stress was observed.

– Tension samples with high aspect ratios (> 5:1) exhibited single slip deformation, negligible hardening, and a moderate dependence of the flow stress on the sample size.

– Load drops in the stress-strain curve along with the corresponding appearance of distinctive glide steps during *in-situ* monitoring lead to the statement that deformation is controlled by a single source for a certain strain increment. The weak size dependence of the flow stress at constant aspect ratio is attributed to the size of the dislocation sources governing plastic deformation.

– Samples with low aspect ratios (1:1) exhibited a pronounced size-effect on the flow stress and significant hardening. This is explained by the formation of a dislocation pile-up.

References

[1] Uchic MD, Dimiduk DM, Florando JN, Nix WD, Science 2004; 305: 986.

[2] Zhang H, Schuster BE, Wei Q, Ramesh KT, Scripta Mater. 2006; 54: 181.

[3] Kiener D, Motz C, Rester M, Dehm G, Mater. Sci. Eng. A 2007; 459: 262.

[4] Motz C, Schöberl T, Pippan R, Acta Mater. 2005; 53: 4269.

[5] Kiener D, Motz C, Dehm G, manuscript under preparation.

[6] Fleck NA, Muller GM, Ashby MF, Hutchinson JW, Acta Met. Mater. 1994; 42: 475.

[7] Kiener D, Rester M, Scheriau S, Yang B, Pippan R, Dehm G, Int. J. Mat. Res. 2007; 98: in press.

[8] Nix WD, Gao H, J. Mech. Phys. Solids 1998; 46: 411.

[9] Foreman AJE, Phil. Mag. 1967; 15: 1011.

[10] Nabarro FRN. Theory of Crystal Dislocations. Oxford: Clarendon Press, 1967.

[11] Hirth JP, Lothe J. Theory of Dislocations. New York: Wiley, 1982.

[12] Parthasarathy TA, Rao SI, Dimiduk DM, Uchic MD, Trinkle DR, Scripta Mater. 2007; 56: 313.

[13] Hull D, Bacon D. Introduction to Dislocations. Oxford: Elsevier Butterworth-Heinemann, 2004.

[14] Dewald DK, Lee TC, Robertson IM, Birnbaum HK, Scripta Metallurgica 1989; 23: 1307.

[15] Diehl J, Z. Metallkd. 1956; 47: 331.

[16] Kocks UF, Mecking H, Prog. Mater. Sci. 2003; 48: 171.

[17] Kiener D, Motz C, Schöberl T, Jenko M, Dehm G, Adv. Eng. Mater. 2006; 8: 1119.

[18] Frick CP, Orso S, Arzt E, Acta Mater. 2007; 55: 3845.

[19] Bei H, Shim S, George EP, Miller MK, Herbert EG, Pharr GM, Scripta Mater. 2007; 57: 397.

[20] Moser B, Wasmer K, Barbieri L, Michler J, J. Mater. Res. 2007; 22: 1004.

Appendix A – Remarks to the experimental results

The present investigation advances far beyond conventional small-scale tensile testing. As a consequence, several experimental details had to be considered in advance or demand further discussion.

– Does the weight of the sample head influence the experiments?

To avoid any bending of the tension sample due to the weight of the sample head, the bending stresses must not exceed the critical flow stress of single crystal copper, which is in the order of 1 MPa for macro samples [15]. Therefore, the maximum surface stress due to bending for the used sample geometry was calculated. As a worst case approximation, a bending length of 20 times the sample thickness was assumed, which is significantly longer than in our experiments. This results in a maximum stress at the surface of only $1 \cdot 10^{-3}$ MPa. It is acknowledged that this is only a static estimation, and any dynamic effects must be avoided during sample handling and testing.

– Does FIB preparation influence our results?

Previous investigations [3] pointed out the presence of a damaged layer with a thickness of several tens of nanometres on the surface of FIB milled specimen. Frick et al. [18] suggested that with reduced sample size the ratio of damaged material increases, leading to a rise in flow stress. Depending on the thickness of the layer and assuming a simple composite model, the surface layer must be 7 to 12 times stronger than bulk copper to explain our results, which is rather unlikely. Furthermore, in this case the flow stress should drop significantly once the first glide steps occurred, which was not observed in our experiments. On the other hand, Bei et al. [19] argued that dislocations generated close to the surface during FIB milling determine the flow stress. These dislocation sources are small compared to the tested sample size and should lead to a size-independent flow stress given by the Orowan stress (τ_S ~115 MPa and ~300 MPa for source sizes of 100 nm and 30 nm, respectively) to operate these sources. This is also in contradiction to our results.

– Are we able to distinguish between noise and displacement bursts? What about the resulting error bars?

The limit of the sample dimensions that can be tested is given by the noise present in the experiments. It is crucial to ensure that the magnitude of load drops indicating dislocation bursts is significantly larger than the noise present in the measurement. Therefore, the whole SEM was placed on an active damping system. Nevertheless, the indenter is mounded on leaf springs in a vacuum environment, and therefore without air damping. This makes the system very sensitive to any kind of vibrations. In our case they stem from the turbo molecular pump of the SEM, which can not be uncoupled from the actively damped system. The noise of the free moving indenter under vacuum conditions is in the order of 50 µN, but gets significantly reduced when sample and gripper get into contact. Furthermore, to reduce noise for the smallest specimen with an aspect ratio of 5:1, six parallel samples were fabricated and loaded at the same time.

At the end of every loading experiment the displacement was held constant for 30 s. The noise present during this time with sample and gripper being in contact was evaluated to determine the error bars given in Fig. 10. The lateral dimensions of the specimen were determined using the field emission SEM column of the FIB.

Therefore, the sample was not tilted like in the usual dual beam working mode to avoid uncertainties due to the inclined view. Consequently, the error in lateral dimension is below 50 nm.

– What happens at the beginning of the load-displacement curve?

One aspect to be discussed is the initial part of the loading curve. Despite the nonlinear contribution due to surface roughness, it is still questionable what causes a rise in force of 0.04 mN over a length of ~300 nm in Fig. 3a. From visual observation as well as analysis of the noise present in the load-displacement data, it is clear that there was still a slit between sample and gripper. If the approach was aborted and the sample gripper moved back to its initial position, the load also reduced to the starting level. Charging of the gripper causes an electrostatic repel between sample and gripper, moving back the gripper in the x-direction. This causes a deflection of the leaf springs which is detected as load. After the first contact, both parts are at the same potential and no repelling forces are observed. This gets further supported by the fact that the contrast in the SEM changes once contact between the two parts is established. Considering sample and gripper as plate capacitor, a potential of ~40 V would support sufficient energy to explain the observed effect.

– Why are there different initial loading slopes?

There are two mayor issues for different linear loading slopes. It was already mentioned that one can never achieve a perfect fit between the flanks of sample and gripper. Therefore, one can expect a steeper linear loading slope for any reload cycle (see Fig. 3b). This even holds true if the sample was handled and FIB milled between the two loading steps, as can be seen in Fig. 8. The flanks of sample and gripper were already in contact during the loading of the thicker sample, the surfaces are well adapted. Consequently, the pre-strained sample has a steeper, more linear loading slope compared to the unstrained sample. Additionally, one has to mention that the stiffness of the testing machine was not accounted for.

The second aspect is depicted in Fig. 6, which presents a decreasing loading slope for increasingly constrained tension samples. For samples with an aspect ratio of 1:1 dislocation glide is hindered by the sample geometry. Dislocations can

not reach the sample surface as they pile-up at the flanks (see Fig. 14a). This generates a back stress and requires the activation of other sources and probably also glide systems with a smaller Schmid factor. Therefore, the geometrically confined samples have higher flow stresses than the unconstrained samples. This is also observed in Fig. 9 for samples with a = 8 µm.

It is acknowledged that bending of the samples would also decrease the loading slope. This would be more pronounced for samples with low aspect ratios, as the short sample length leads to higher bending angles. As mentioned previously, we leveraged the visual control provided by the *in-situ* setup to carefully align sample and gripper in order to minimize this influence.

– Is the stiffness of all other involved parts sufficient to ensure accurate determination of strains?

The accurate determination of sample strains requires sufficient stiffness of all involved parts (like copper needle or tungsten gripper). Moser et al. [20] showed the difference between strain calculated simply from piezo displacement and determined properly by image correlation for their *in-situ* micro-compression tests. It is also acknowledged that they used a setup with a rather low stiffness. In our case, the displacement is measured at the indenter tip. Furthermore, after unloading (Fig. 4f), the sample stayed in position, indicating that only the tensile sample was uniaxially deformed. No plastic deformation of any other involved part was detected.

VI FIB Damage of Cu and Possible Consequences for Miniaturized Mechanical Tests (Publication E)

D. Kiener, C. Motz, M. Rester, and G. Dehm

Materials Science & Engineering A (2007) Vol. 459; Issue 1-2; 262-272.

Abstract

Cu specimens were exposed to Ga^+ ion bombardment for varying conditions of ion energy, ion dose, and incident angle in a focussed ion beam workstation. Conventional transmission electron microscopy investigations were employed to analyze the Ga^+ ion induced damage. The extent of visible damage was minimized by reducing the ion energy and furthermore by using grazing incident ions. Concentration depth profiles of the implanted Ga were measured by Auger electron spectroscopy. Concentrations of up to 20 at% Ga were found several nanometers below the surface. Ga contents of more than 2 at% were detected within a depth of up to ~50 nm. Mechanical consequences in terms of possible hardening mechanisms are discussed, taking into account the experimental findings along with Monte Carlo simulations. A non-negligible influence of the ion damage is predicted for submicron sized samples.

1. Introduction

From the 1980s onwards the focussed ion beam (FIB) microscope has been mainly used in the semiconductor industry as a tool for device imaging, modification and mask repair. Several years ago, the FIB technique has found a broader variety of applications in material science [1]. This increased use is due to several key factors: (i) site-specific preparation of thin foils for transmission electron microscopy (TEM) investigations, (ii) a strong channelling contrast allowing discrimination of different grain orientations, and (iii) secondary ion mass spectroscopy (SIMS) and/or energy dispersive X-ray (EDX) spectroscopy attached to the FIB workstation for local chemical analyses. Recently, the FIB became popular as a tool for machining miniaturized samples [2-7] to investigate the influence of sample dimensions on mechanical properties. As the surface to volume ratio is large for submicron sized test structures, any surface modifications by ion bombardment and implantation may critically alter the mechanical properties.

So far, detailed studies on FIB induced Ga^+ ion damage were mainly performed on semiconductor materials, especially Si [8-15]. TEM investigations revealed the width of the amorphous surface layer introduced by ion milling to be in the order of several tens of nanometers, depending mainly on the kinetic energy and incidence angle of the used ions, and on the milling geometry [8-13]. Comparison of these results to Monte Carlo simulations, mainly using the SRIM code [11, 13-15], showed good agreement.

Few data on other materials is available [16-19], and the applied methods and parameters differ remarkably, preventing a conclusive comparison. Therefore, we decided to investigate the Ga^+ ion damage of Cu, a material we frequently investigate with respect to mechanical size effects [5, 7]. In addition to TEM investigations of the Ga damaged microstructure, Auger electron spectroscopy (AES) measurements were carried out for reliable information on the depth profile of the Ga concentration. The results are compared to SRIM calculations. Finally, the impact on mechanical data obtained by FIB-made mechanical test structures is discussed.

2. Experimental

2.1 TEM investigations

For the TEM investigation of the Ga^+ ion damage a 150 nm thick polycrystalline Cu film with an average grain size of approximately 300 nm deposited on a ~100 nm thick amorphous SiN_X membrane was used. The Cu film was intentionally damaged with Ga^+ ions using a dual-beam workstation (LEO XB1540) consisting of a high-resolution field-emission scanning electron microscope (SEM) and an integrated scanning Ga^+ FIB column. The kinetic energy of the primary Ga^+ ions can be varied between ~2 keV and 30 keV. After carefully positioning the flat sample in the SEM-FIB coincidence point, the milling patterns were defined using the SEM. This procedure prevents unintentional Ga^+ ion damage prior to the well-defined milling procedures. Three different types of patterns were milled for various primary Ga^+ ion beam conditions:

(i) Line pattern

In this mode the ion beam is scanned along a defined line with a length of 5 µm for 5 s with a frequency of 20 kHz. This pattern is intended to provide a defined edge to measure the thickness of the damaged layer with a TEM.

(ii) Milling rectangle

This is the usual working mode when attempting to remove material. The defined milling region is divided into several thin stripes with a certain overlap of the individual elements. These are successively scanned by the ion beam for a fraction of the total milling time (according to their area fraction), resulting in a step-like depth-profile of the milled area. This mode is comparable to the clean-up cut when using FIB instruments from other companies (e.g. [15]). In this study rectangles with a width of 10 µm and a height of 5 µm were milled for 30 s.

(iii) Deposition rectangle

This mode is conventionally used for ion induced material deposition or gas assisted etching. Rectangular areas of the same dimensions as in (ii) were scanned by the ion beam with a horizontal frequency of 20 kHz and a vertical frequency of 0.1 Hz. The duration of exposure was again 30 s. This results in a

very smooth surface topography. With this approach interfering surface irregularities due to selective sputtering, as reported by other authors for both polycrystalline and single-crystal Cu [15], can be minimized. The FIB parameters used for the various implantation experiments are summarized in Table 1.

Table 1: FIB parameters for the milling objects investigated by TEM. The calculated ion dose increases from $3.7 \cdot 10^{15}$ cm^{-2} for 10 pA to $7.5 \cdot 10^{17}$ cm^{-2} for 2000 pA (milling and deposition mode).

Milling mode	Line	Milling	Deposition	Line	Milling	Deposition
Accelerating voltage (kV)	30	30	30	5	5	5
Ion current (pA)	10	10	10	20	20	20
	50	50	50	50	50	50
	100	100	100	100	100	100
	500	500	500	200	200	200
	2000	2000	2000	500	500	500

The patterns of type (i) are intended to estimate the thickness of the damaged layer formed by grazing ion bombardment, which is the usual working condition. The patterns of type (ii) and (iii) were milled with perpendicular ion impact to serve as worst case examples in order to get an upper limit for the damage depth. The range of applied milling currents covers typical FIB parameters from coarse material removal down to surface finishing, from imaging conditions to TEM specimen preparation. In order to minimize the induced Ga damage, the accelerating voltage was reduced from 30 kV to 5 kV.

For Si it is well known from SRIM calculations [14, 15] and experiments [9-11] that milling under grazing ion impact will minimize the damage. Therefore, we also prepared TEM samples from single-crystal Cu under the mentioned grazing ion incident with kinetic energies of 30 keV and 5 keV. All samples were thinned down to a thickness of ~1 µm with 30 keV Ga^+ ions and milling currents of 1000 to 2000 pA. For the final thinning to a thickness of approximately 120 nm the applied ion currents were stepwise reduced to 50 pA for 30 keV Ga^+ ions or 100 pA for 5 keV Ga^+ ions. In order to keep the conditions comparable to samples exposed to perpendicular Ga^+ ion impact, no protective layer was applied prior to thinning.

Subsequently, all damaged regions were examined in a conventional TEM (Phillips CM 12) equipped with an EDX system (EDAX). An accelerating voltage of 120 kV was used for all investigations. The EDX spectra were acquired for 100 s using spot mode with a minimum spot diameter of ~25 nm.

2.2 AES measurements

Samples with dimensions of 3 x 3 x 1 mm^3 and a [100] surface normal were cut from a larger Cu single crystal using a diamond wire saw. Subsequently, the top surface was electro-polished to remove the deformation layer produced by the cutting process. An area of 50 x 50 μm^2 was exposed to the 30 keV Ga^+ ion beam using the deposition mode, with the parameters given in Table 2. Again, all milling patterns were pre-defined in the SEM mode.

Table 2: Milling currents, exposure times, and calculated ion doses for Ga exposed areas of 50 x 50 μm^2 in size. Ion doses are given in units of cm^{-2}.

Milling current (pA)	Milling time (s)			
	300	500	1000	3000
50	$3.7 \cdot 10^{15}$	$6.2 \cdot 10^{15}$	$1.2 \cdot 10^{16}$	$3.7 \cdot 10^{16}$
500	$3.7 \cdot 10^{16}$	$6.2 \cdot 10^{16}$	$1.2 \cdot 10^{17}$	$3.7 \cdot 10^{17}$
1000	$7.5 \cdot 10^{16}$	$1.2 \cdot 10^{17}$	$2.5 \cdot 10^{17}$	$7.5 \cdot 10^{17}$
10000	$7.5 \cdot 10^{17}$	$1.2 \cdot 10^{18}$	$2.5 \cdot 10^{18}$	$7.5 \cdot 10^{18}$

The AES investigations were carried out using a VG-Scientific Microlab 310-F field emission instrument with a thermally assisted Schottky field emission source at an accelerating voltage of 10 kV, a beam diameter of 10 nm, and a beam current of 10 nA. The electron analyzer is a double focussing spherical sector type with an electrostatic input lens. The spectrometer has five sequential electron detectors, each of which detects 2.5 % of the pass energy. Spectra are acquired with a constant retard ratio of 4, providing an energy resolution of 0.5 % of the pass energy.

The use of a field emission source in conjunction with an efficient electron spectrometer provides an overall energy resolution better than 2 %. Secondary electron imaging was performed to accurately position the Ga implanted regions

for the AES measurement. Repeated Ar^+ sputtering at 3 keV, with a sputter rate of 0.017 nm/s for Cu, followed by subsequent AES investigation, was used to obtain depth profiles of the Ga concentration in Cu.

3. Results

In this section we first describe the TEM results of the Cu samples exposed to different milling conditions under perpendicular and grazing ion impact. Subsequently, the AES measurements of the implanted Ga concentrations are presented.

3.1 TEM investigations

- Line patterns

Examination of the line patterns in Fig. 1a milled with an accelerating voltage of 30 kV under normal incidence (edge-on) showed an amorphous layer with a thickness of ~10 nm for a Ga^+ ion current of 50 pA, indicated in the inset of Fig. 1a. Fig. 1b presents the spectrum that was recorded at position A with a nominal spot size of 25 nm. No Ga was detected at this position within the limits set by noise. Fig. 1c shows the EDX spectrum of position B revealing a substantial amount of Ga. It is not attempted to quantify this result due to the unknown sample thickness at these positions. However, the EDX measurements indicate qualitatively that the Ga contamination is localized to the amorphous region. All spectra were acquired with a tilt angle of the sample of 20 °. At the edge (position B) the film to substrate ratio is smaller than at position A. This is reflected by the higher Si and N peaks in Fig. 1c deriving from the underlying SiN_X support.

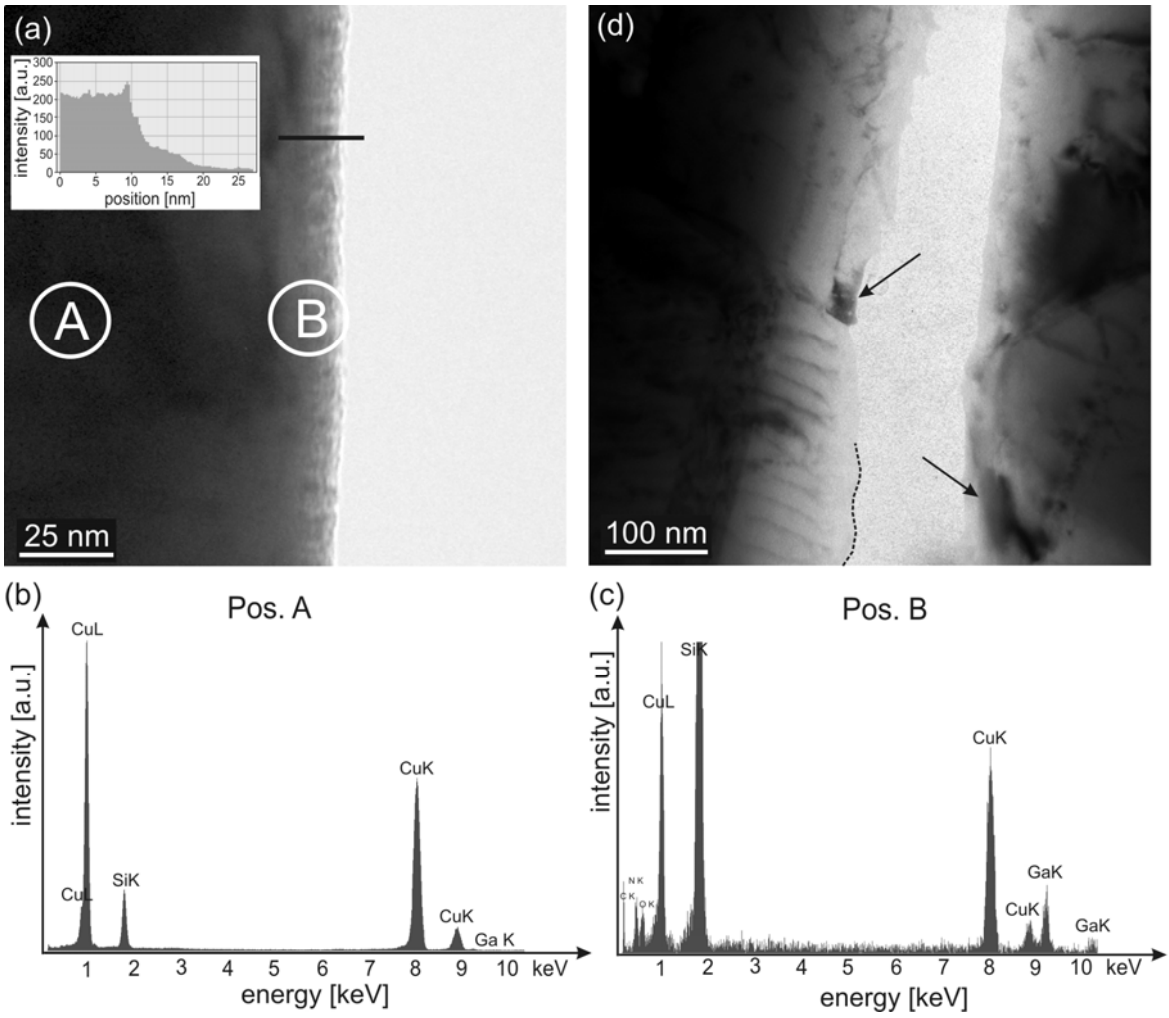

Fig. 1: (a) Bright-field TEM image of a line milled with 50 pA and an accelerating voltage of 30 kV. The inset shows the image intensity profile along the marked horizontal line, the circles indicate the position and spot size for the EDX measurements shown in (b) and (c). (d) Bright-field TEM image of a line milled with 50 pA and an accelerating voltage of 5 kV. See text for more details.

The lines milled with an accelerating voltage of 5 kV exhibit a damaged layer up to ~100 nm wide, as indicated in Fig. 1d. From the shape irregularities of the line patterns it can be concluded that the 5 keV ion beam is less well-focussed than the 30 keV beam. This in turn prevents an exact determination of the width of the amorphization zone for 5 keV Ga^+ ion bombardment, which seems to be smaller than ~3 nm.

- Rectangles produced in deposition mode

All areas bombarded with Ga^+ ions, even those with low milling currents and 5 kV accelerating voltage, reveal a damage structure with a strain contrast comparable to a dislocation network under two-beam imaging conditions. Fig. 2a shows a dark-field image of a ~1 µm large Cu grain extending across the border of the damaged into the undamaged region. The image was recorded using $g_{-2\ 2\ 0}$ diffraction condition as indicated in the inset in Fig. 2a. The right part of the grain was exposed to Ga^+ ions with a kinetic energy of 30 keV and an ion current of 50 pA. The left part of the grain appears to be devoid of Ga induced artefacts. Even after a Ga^+ bombardment using an accelerating voltage of 5 kV and an ion current of 50 pA a dislocation-like damage structure is observed in Cu (Fig. 2b).

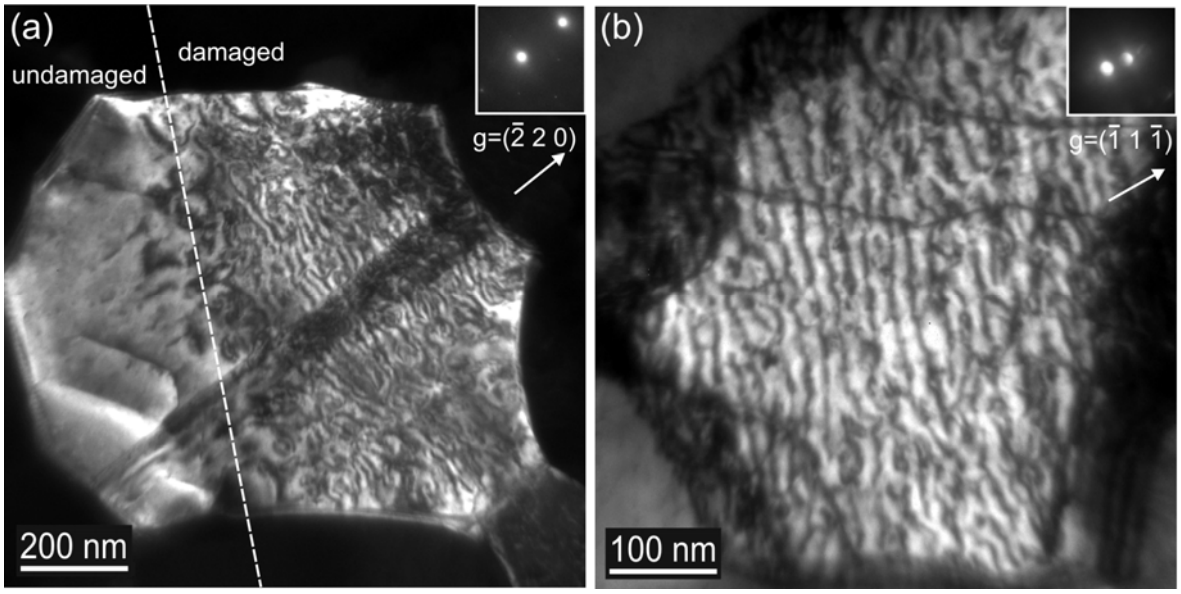

Fig. 2: (a) Dark-field TEM image of a Cu grain situated at the border of an ion damaged and undamaged region. The right part of the grain was exposed to Ga^+ ions with a kinetic energy of 30 keV and an ion current of 50 pA. The $g_{-2\ 2\ 0}$ diffraction condition is shown in the inset. (b) Bright-field TEM micro-graph of the damage pattern of a grain bombarded by 5 keV Ga^+ ions and an ion current of 100 pA. The $g_{-1\ 1\ -1}$ diffraction condition is shown in the inset.

The reduction of the accelerating voltage did not result in avoiding a disturbed region becoming visible in TEM images. At 5 keV the damage pattern is still present, in agreement with findings in literature [20]. Nevertheless, two differences between 5 keV and 30 keV damage were found. Pre-existing defects, like

individual dislocations which originated earlier during thermal straining [21], are still visible in the damaged region at 5 keV, but were hardly ever detected in areas exposed to a 30 keV Ga^+ ion beam. Furthermore, the poor focussing of the ion beam at the low accelerating voltage results in a damaged area exceeding the borders of the predefined milling area. This area becomes visible in bright-field TEM images even though no Ga can be detected by EDX. For 5 keV Ga implantation a noticeable EDX signal was obtained in our study for a ion dose $\geq 3.7 \cdot 10^{16}$ cm^{-2}. However, a quantitative EDX analysis of the Ga contents was prevented by the differences in remaining Cu thicknesses for the various milling conditions (see the calculated sputter yields for 30 keV and 5 keV in Table 3).

Table 3: SRIM calculated values of sputter yield and target depth at 0.5 dpa for a primary Ga^+ ion beam of 30 keV and 5 keV, respectively. The impinging angle was 89.9° in both cases.

Ion energy (keV)	Sputter yield (Atoms/Ion)	Target depth at 0.5 dpa (nm)
30	14.4	7.2
5	7.1	2.0

In order to analyze whether the damage structure observed by TEM stems from dislocations, different diffraction conditions were used. Fig. 3 shows as an example two TEM images of Cu grains exposed to perpendicular 30 keV Ga^+ ions and an ion current of 50 pA recorded under different diffraction conditions. The two different diffraction vectors are indicated for the large grain right hand side of Fig. 3. The visibility of the dislocation-like network changes with diffraction condition, as for a network consisting of dislocations with different Burgers vectors. Furthermore, the strain contrast vanishes for certain imaging conditions, as can be seen e.g. for the large grain in the centre.

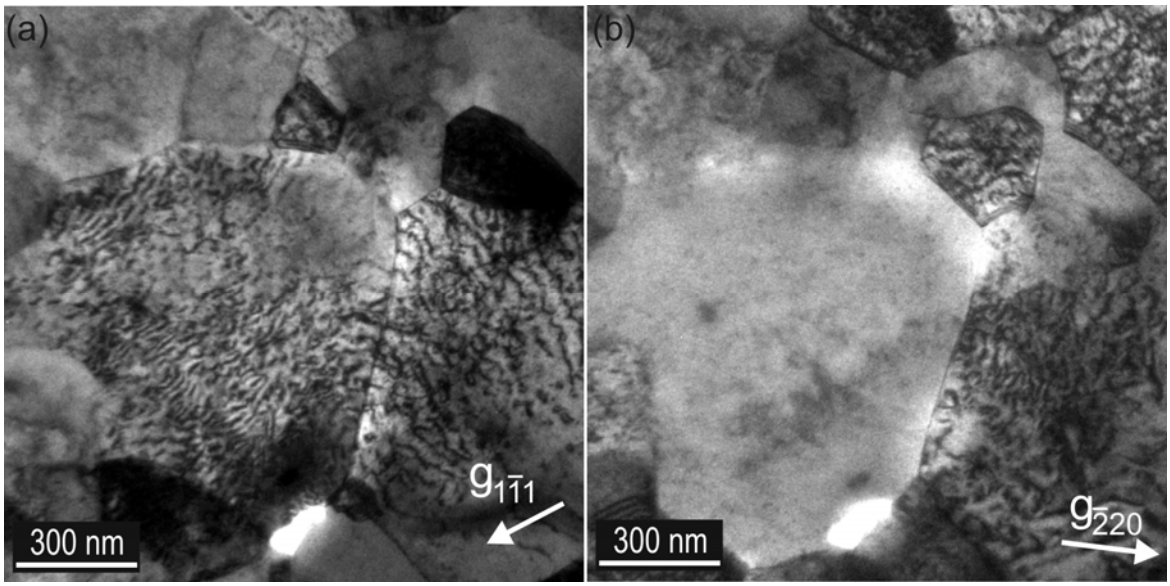

Fig. 3: Bright-field TEM images of Cu grains exposed to perpendicular 30 keV Ga^+ ions and an ion current of 50 pA under different diffraction conditions. The diffraction vector is shown for the grain on the right hand side. The strain contrast vanishes for certain conditions, as can be seen for several grains (compare Fig. 3a and b).

- Rectangles produced in milling mode

In this case, the same results hold true as for the deposition mode. In addition, contrast variations become visible if the overlap of adjacent milling lines at 30 keV is insufficient (see e.g. Fig. 4). For the patterns milled at 5 keV, the broad Ga^+ ion beam caused enough overlap to lead to identical patterns for milling and deposition mode.

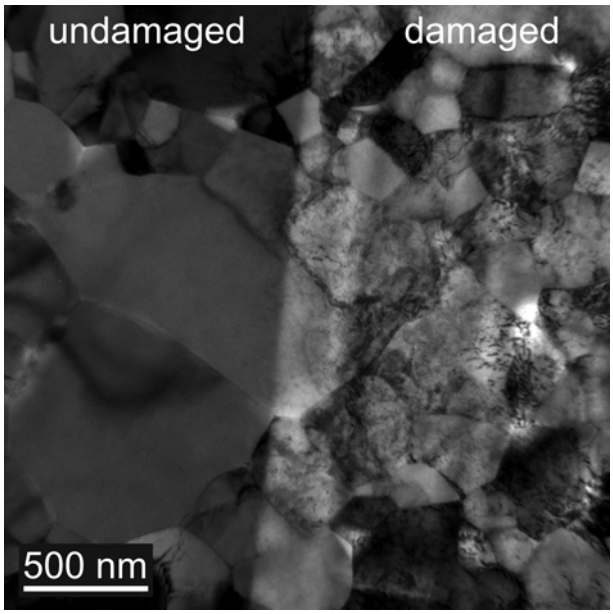

Fig. 4: Bright-field TEM micrograph of the Cu film showing undamaged (left) and Ga damaged (right) areas. Ga^+ ions with a kinetic energy of 30 keV and an ion current of 50 pA were used for milling. Contrast changes due to insufficient overlap of the adjacent milling stripes are clearly recognisable.

3.2 Grazing Ga^+ ion incident at 30 keV and 5 keV ion energy

We examined the reduction of Ga^+ introduced milling artefacts in Cu by reducing the ion incidence angle and ion energy. Fig. 5a shows a TEM bright-field micrograph of a single-crystal Cu specimen prepared by FIB with Ga^+ ions under grazing incidence at a kinetic energy of 30 keV and a milling current of 50 pA. The damage pattern is reduced compared to perpendicular impact of ions with the same kinetic energy (compare Figs. 2-5). Fig. 5b shows a TEM bright-field image of another area of the same Cu sample, which was finally thinned with a kinetic energy of 5 keV and a milling current of 100 pA. There is still some damage present, but it is distinctively reduced compared to Fig. 5a due to the reduction in ion energy, although the final milling current used was 100 pA.

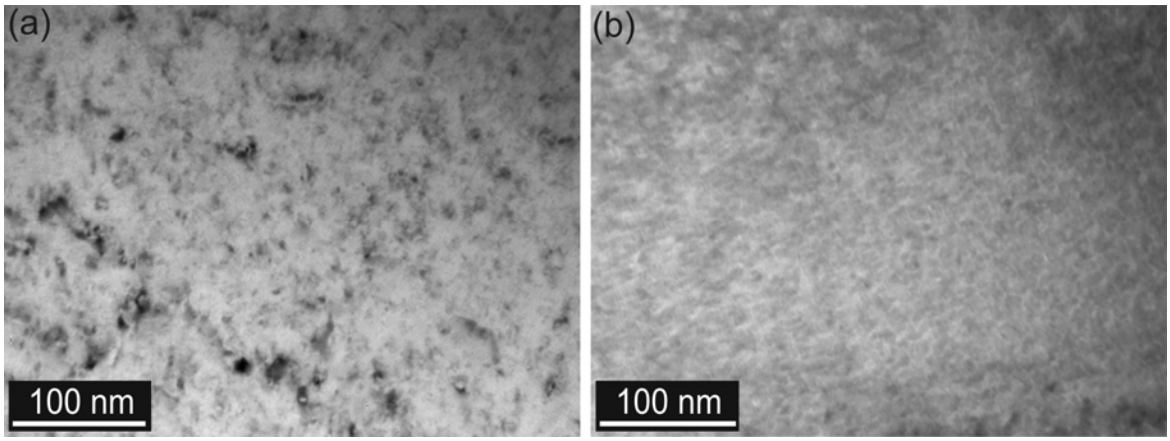

Fig. 5: (a) TEM bright-field image of a single-crystal Cu sample thinned with grazing incident Ga^+ ions with a kinetic energy of 30 keV and a final milling current of 50 pA exhibiting a damaged surface structure. (b) TEM bright-field micrograph of a region of the same sample milled with 5 keV grazing incident Ga^+ ions and a final milling current of 100 pA.

3.3 AES measurements

In contrast to the TEM studies, which were performed to reveal the surface damage, AES measurements were conducted to obtain quantitative chemical information on the amount of implanted Ga and the depth profiles for different Cu microstructures (single-crystal, polycrystalline), accelerating voltages, ion currents, and implantation times (ion dose). Fig. 6a shows the AES depth profiles for single-crystal Cu samples with a [100] surface normal exposed to 30 keV Ga^+ ion bombardment in deposition mode. Milling currents of 50 pA, 500 pA, 1000 pA, and 10000 pA were applied with milling times ranging from 300 s to 3000 s (see Table 2).

An increase of the maximum Ga concentration with increasing ion dose was found. For high ion currents of 1000 pA and 10000 pA and higher milling times a saturation concentration of 12 at% Ga is reached at a depth of ~10 nm. It takes 40 to 50 nm to decrease this concentration to values below 2 at% Ga.

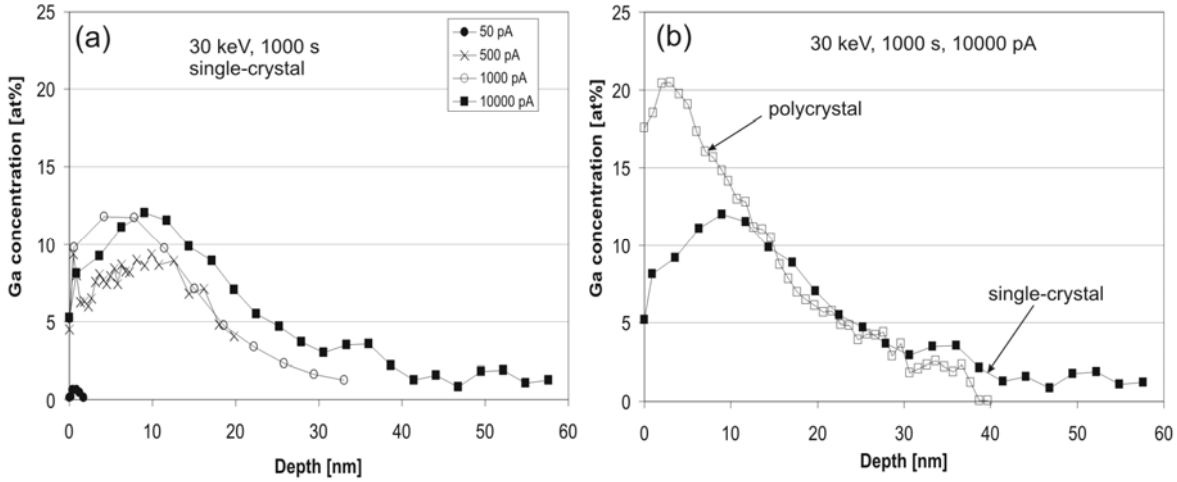

Fig. 6: (a) AES depth profiles showing the influence of the milling current (ion dose) on the resulting Ga concentration profile. (b) Comparison between the depth profiles for single-crystal Cu and severely plastically deformed Cu with a grain size of ~300 nm. The ion beam parameters are depicted in the diagrams.

Fig. 6b depicts the influence of the microstructure. For this purpose pure Cu with an average grain size of ~300 nm, produced by severe plastic deformation [22], was used. The grain size is comparable to the grain size of the Cu film used for the TEM investigation. The ultra fine grained (UFG) Cu reveals a higher maximum concentration (21 at% Ga) at a lower depth (~3 nm below the surface) compared to the single-crystal sample (12 at% Ga, ~10 nm). To reach concentrations below 2 at% a depth of 35 nm compared to 50 nm has to be removed for the polycrystalline Cu sample.

4. Discussion

In order to reduce the damage introduced by the Ga^+ ion bombardment, several possibilities exist. For example: (i) use of a protective layer, (ii) low incidence angle of the impinging Ga^+ ions, (iii) low ion energies, and (iv) optimized milling geometries in order to avoid redeposition. A further possibility to reduce the thickness of the damaged layer would be to increase the atomic mass of the impacting ions, as was demonstrated by Jamison et al. [13] for Ga^+ and In^+ ions on Si. However, most commercial FIBs use Ga^+ ion sources and variable FIB ion sources for one workstation are rather unusual. We will now focus on the influence

of (ii) and (iii) on the formation of an amorphous layer, the implanted Ga content and surface roughening during FIB milling, and the possible consequences on the mechanical properties of miniaturized samples.

4.1 Formation of an amorphous layer due to Ga^+ ion bombardment

The best known damage introduced during FIB milling is the formation of an amorphous Ga containing layer due to Ga implantation and knock-on damage.

The amount of damage caused by the ion bombardment can be estimated by Monte Carlo simulations using the SRIM code [14]. Fig. 7a and b show the displacements per atom (dpa) caused by a 30 keV and a 5 keV Ga^+ ion beam hitting the Cu target at a grazing angle of 89.9°. For a simple comparison between both bombardments the target depth for a certain dpa value can be used. Assuming that 0.5 dpa, which indicates that every second bond is broken, should destroy the crystalline structure, amorphous layer thicknesses of ~7 nm (30 keV) and 2 nm (5 keV) are postulated (Table 3). Healing effects are neglected in this calculation. For comparison, the amorphous layer thicknesses estimated from our conventional TEM studies amount to approximately 10 nm (30 keV, 50 pA) and less than 3 nm (5 keV, 50 pA).

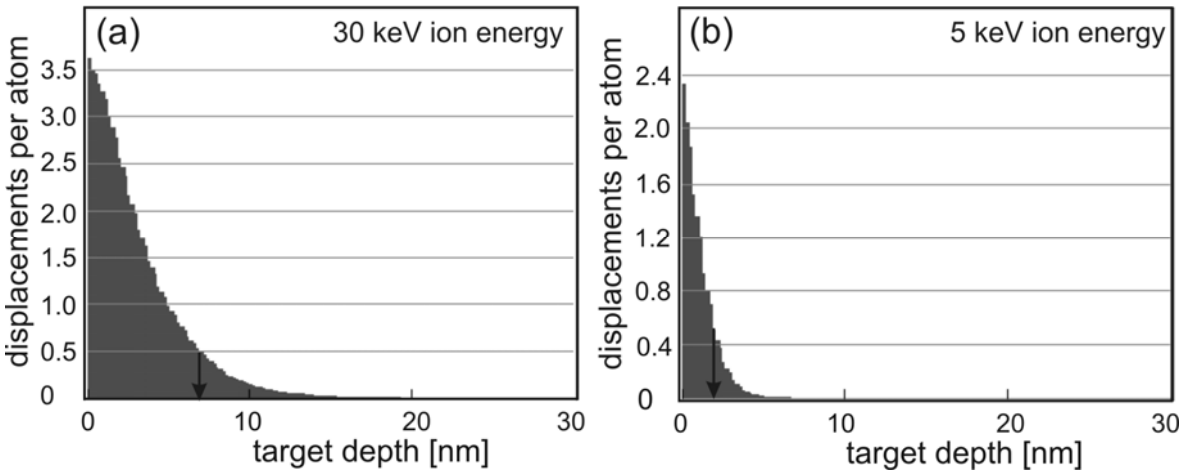

Fig. 7: SRIM [14] calculations showing the displacements per atom (dpa) for Cu exposed to a Ga^+ ion beam with grazing impact (89.9°) and a kinetic energy of (a) 30 keV and (b) 5 keV.

Matteson et al. [23] performed TEM and electron backscattering diffraction (EBSD) investigations on FIB-prepared Cu and Si cross-sections. They stated that no

amorphous layer was formed on Cu and justified this by the fact that EBSD patterns were obtained from FIB-prepared surfaces. From our TEM investigations it is clear that, depending on the ion dose [24], an amorphous layer with a thickness of up to ~50 nm (30 keV, 2000 pA) formed. Nevertheless, we also managed to obtain EBSD patterns from FIB polished Cu surfaces [25]. We conclude therefore that the presence of EBSD patterns does not exclude the presence of a thin amorphous surface layer.

4.2 Ga implantation and surface roughening during FIB milling

– Ga implantation:

Besides amorphization, implantation of Ga into the investigated material also takes place. The depth of implantation can again be estimated using the SRIM code [14]. Fig. 8a shows that the penetration depth for implanted Ga^+ ions with a kinetic energy of 30 keV and perpendicular ion impact is ~24 nm. Figs. 8b-d reflect the reduction in damage that can be expected when reducing the ion energy and/or the impact angle. For perpendicular impact of 5 keV Ga^+ ions a penetration depth of ~8 nm is predicted (Fig. 8b). For grazing incident of the Ga^+ ions these values reduce to ~15 nm at 30 keV (Fig. 8c) and ~5 nm at 5 keV (Fig. 8d).

These simulation results are in agreement with the experimental findings from our AES and TEM measurements. The AES investigations indicate a penetration depth of 40 - 50 nm for perpendicular Ga^+ ion bombardment of Cu at 30 keV (see Fig. 6), which is in the same order as the maximum width of the amorphous layer observed in the TEM investigations.

The AES measurements show that the maximum Ga concentration can be found several nanometres below the surface, as proposed by a dynamic damaging model by Rubanov and Munroe [9], in agreement with the maximum Ga^+ ion concentration depths evaluated by the SRIM simulations (Fig. 8).

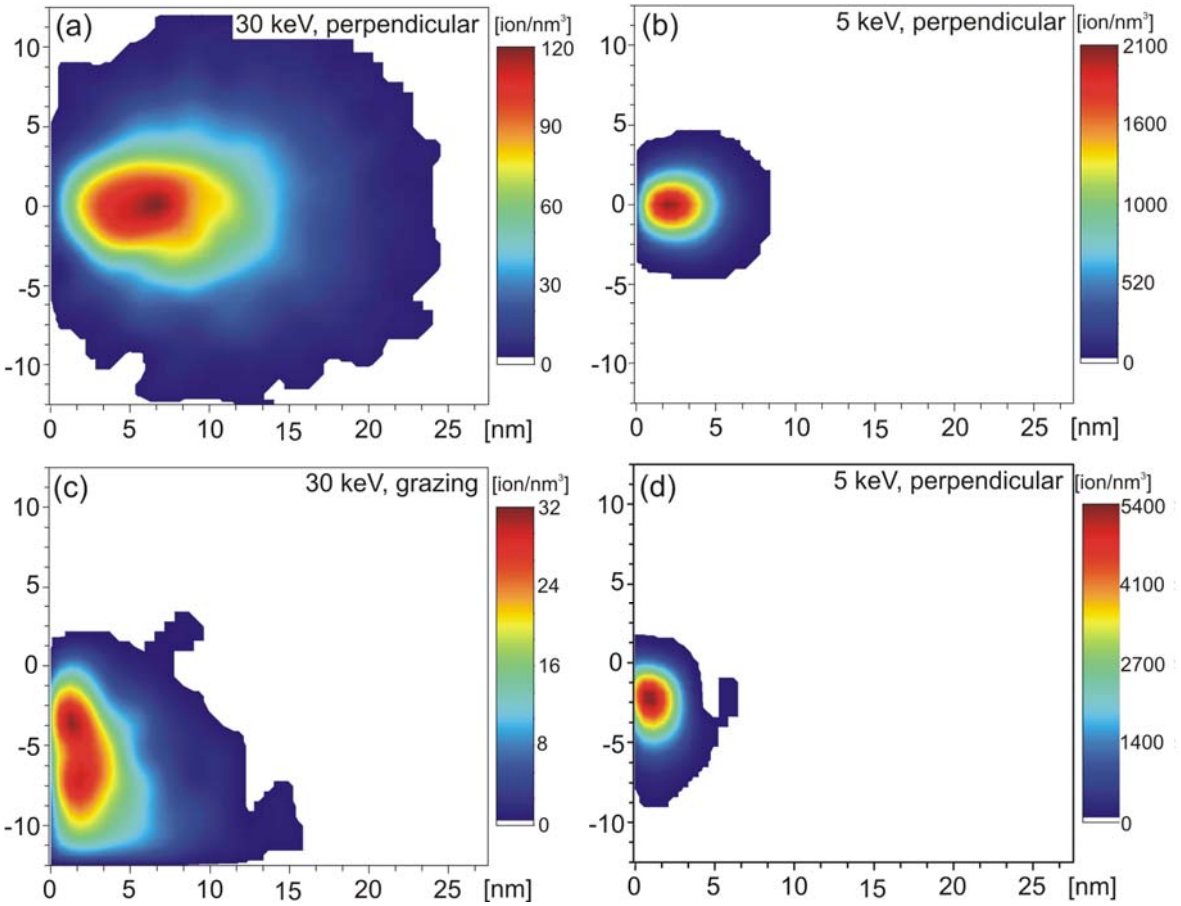

Fig. 8: SRIM [14] predictions for the penetration depth of Ga^+ ions into Cu for perpendicular impact at (a) 30 keV and (b) 5 keV ion energy and grazing impact at (c) 30 keV and (d) 5 keV. Ga concentrations below 2 at% are not displayed in the plots to keep them comparable to the AES measurements. As no atomic structure is underlying the simulation, the calculated ion concentrations can locally reach unrealistic high values.

The differences found in Fig. 6b between polycrystalline and single-crystal material in terms of maximum concentration and penetration depth can not be explained in the framework of this Monte Carlo simulation, as the target material is assumed to be amorphous for the simulation. The UFG material possesses a high concentration of grain boundaries, dislocations, and vacancies as well as a randomly oriented grain structure [22]. The smaller penetration depth is mainly caused by the various crystal orientations of the UFG Cu preventing channelling. The {100} crystal planes of Cu are more open than e.g. the {111} planes [26]. Thus, the random oriented grains of the severe plastically deformed Cu possess on average a reduced channelling depth than the {100} oriented single crystal. The structural defects present in the UFG material might even increase this effect. This

leads to a higher maximum Ga concentration for the UFG material. Consequently, the maximum concentration of Ga in the UFG material is closer to the Cu surface compared to the single-crystal material.

An opposite Ga depth profile would be expected if diffusion plays a role. Since the UFG microstructure remains stable, we exclude diffusion playing a role for the Ga depth profiles at room temperature. Furthermore, a calculation of the local temperature rise due to focussed ion beam heating during ion implantation predicts a local rise in temperature of only a few degrees, following the work of Melngailis [27] and Ishitani and Kaga [28], even taking into account the confined geometry and heat flux of micron-sized features, e.g. pillars. We therefore conclude that diffusion of Ga is not an important mechanism during FIB milling of Cu samples.

– Surface roughening:

Another aspect which should be considered, as it influences both the sample production and the subsequent investigations, is the existence of a surface topography. Surface roughening would lead to a self-exaggerating selective sputtering effect during FIB milling due to a variation of sputter yield with incidence angle, as shown by Prenitzer et al. [15]. Further complications could arise during Ar^+ sputtering when performing the AES depth profiles on a rough surface. Therefore, roughness measurements of the surface before and after exposure to the Ga^+ ion beam were performed for the single-crystal Cu specimen using an atomic force microscope (Digital Instruments DI 3100). The arithmetic mean roughness R_a for normal incidence increased only slightly from R_a = 10.6 nm for the electro-polished specimen to values ranging from R_a = 10.7 nm to R_a = 16.4 nm for the various milling parameters. No correlation between milling current, exposure time and resulting surface roughness was found for normal incidence. Therefore, the Ar^+ sputtering should lead to comparable AES depth profiles for the various Ga implanted areas. This may be different for grazing Ga^+ incidence, since this can cause surface roughness and rippling [29].

4.3 Defects

Several defects form in the ion bombarded area: point defects, dislocations and precipitates. Single point defects like Ga interstitials are hard to investigate, but vacancy clusters in form of stacking fault tetrahedra were e.g. reported by [24] for high energy bombardment and modelled by Caturla et al. [30] for 30 keV bombardment. Ga based precipitates formed by FIB milling were found by Marien et al., who performed a high resolution TEM investigation of a Cu metallization layer prepared by FIB methods [16], by Yu et al. [19], who investigated an interstitial free steel, and by Phaneuf and Casey [31], who reported the formation of a Cu_3Ga phase during near-normal incidence milling of single crystal [110] Cu.
With our conventional TEM we were not able to identify precipitates. Marien et al. and Yu et al. claimed the presence of a dislocation network, but did not perform further investigations on the nature of these dislocations. Dislocation contrast vanishes, if the diffraction vector is perpendicular to the Burgers vector [32]. As a consequence different dislocations may be visible for different diffraction conditions (see Fig. 3). The observed dislocation network may have formed as a consequence of the misfit strain induced by the precipitates detected by Marien et al.. Alternatively, dislocation loops from the collapse of vacancy clusters, which additionally may be decorated with Ga, can cause a similar contrast in their superposition. The invisibility of pre-existing dislocations for a 30 keV Ga^+ ion bombardment compared to 5 keV might result from a higher fraction of line defects and a higher Ga penetration depth. The damage structure created by the grazing ion beam at 30 kV (Fig. 5) is principally the same as for normal incidence (Fig. 3), but the lower Ga penetration depth for grazing incidence results in less defects and most likely a reduced Ga decoration. Therefore, the strain contrast of individual defect clusters becomes visible. Eventually, the strain contrast of the defects almost vanishes for 5 keV grazing incidence (Fig. 5b).
Surface phase formation [31] might have occurred in Fig. 1d adjacent to the amorphous layers in the dark regions which are indicated by arrows. Due to the less well focussed 5 keV ion beam, regions close to the milled line were exposed to near-normal Ga^+ ion bombardment. Generally, these surface phases should not play a dominant role when performing mechanical tests, because a grazing incidence of the ion beam is aspired for milling, where these phases were not reported to form [31].

4.4 Possible consequences on the mechanical properties

The recent interest in producing miniaturized mechanical test samples by the FIB technique requires knowledge of possible artefacts introduced by the Ga^+ ion bombardment. Depending on the kind of defects formed, the mechanical properties could be affected by the presence of Ga implantation. In this section we try to estimate the contribution of the Ga damaged surface layers to the flow stress evaluated for micron-sized Cu pillars with diameter *d* and height *h*, as schematically depicted in Fig. 9, by a simple composite model.

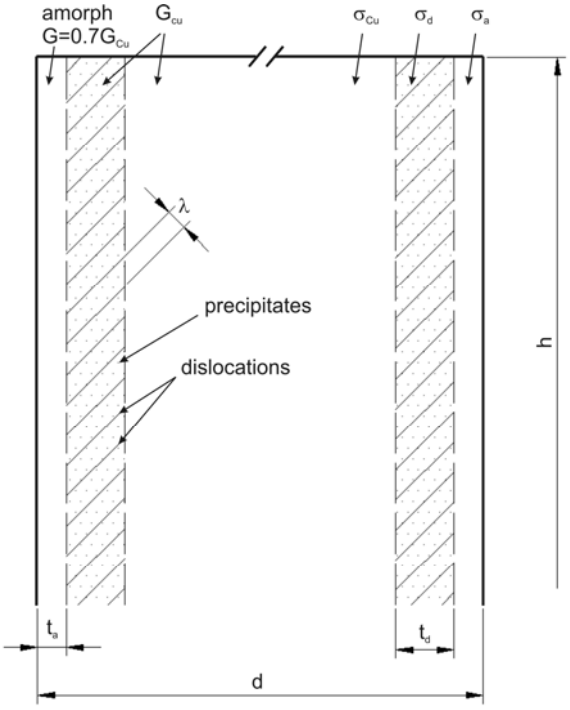

Fig. 9: Schematic composite model of a FIB fabricated pillar with height *h* and diameter *d*, consisting of an amorphous layer with a thickness t_a, shear modulus $G = 0.7G_{Cu}$ and flow stress σ_a, a damaged layer with a thickness t_d, shear modulus G_{Cu} and flow stress σ_d, and the unaltered material with the material properties being G_{Cu} and flow stress σ_{Cu}.

First we consider the outer amorphous layer, owing a thickness t_a of ~50 nm. Due to the absence of a crystal structure, we do not expect solution hardening to take place, nor the formation of dislocations. It remains unclear, whether Ga-based precipitates form in this amorphous layer, but as there are no dislocations present, Taylor hardening as well as precipitation hardening are excluded as possible hardening mechanisms in this layer.

Nevertheless, the amorphous layer can cause a pile-up of dislocations from the underlying material. This would exert a back-stress on operating internal dislocation sources, resulting in an increased flow stress. The model of Friedman and Chrzan [33] considers a single-ended dislocation pile-up at an interface and incorporates a source term, which becomes dominant for the deformation behaviour of submicron sized mechanical test samples. The necessary stress to operate a dislocation source against the acting back-stress was found to be

$$\sigma_{\mathrm{A}} = \left(\frac{G_{\mathrm{Cu}} b \sigma_{\mathrm{a}}}{\pi d} + \sigma_{\mathrm{S}}^2 \right)^{1/2}, \qquad \text{(VI.1)}$$

where σ_{A} is the applied stress, G_{Cu} = 47 GPa the shear modulus, b = 0.255 nm the Burgers vector, σ_{a} the flow stress of the amorphous interface, d the critical length scale, and σ_{S} the source strength. The back-stress resulting from the dislocation pile-up leads to an increased flow stress scaling inversely with the square root of the critical length scale. As σ_{a} is unknown, estimation of an upper bound value of σ_{A} can be performed as follows: Take σ_{a} to be equal to the theoretical shear stress of the Ga containing amorphous layer, which is assumed to have a shear modulus G 30 % lower than the crystalline material. This assumption is reasonable, as the elastic properties are dominated by the binding properties of the matrix and vary only slightly with the concentration of alloying elements. σ_{S} can be estimated by calculating the Frank-Read stress for an optimal source size of 1/3 of the critical sample dimension [34]. These considerations lead to an applied stress σ_{A} ~35 MPa for a sample with 10 µm diameter and σ_{A} ~110 MPa for a 1 µm sample, where flow stresses in the order of 200 MPa and 1 GPa have been reported, respectively [7].

In the next paragraph we consider the possible mechanical consequences due to the presence of a ~50 nm thick damaged zone succeeding the amorphous layer, which may contain point-defects, dislocations, and Ga-based precipitates (Fig. 6a). If the implanted Ga forms a solid solution, a negligible contribution to the flow stress in the order of 3-4 MPa can be predicted ($\Delta\tau \propto \sqrt{c_{\mathrm{Ga}}}$) [35-37] for the damaged zone when assuming an average Ga concentration of 2 at% (Fig. 6). The effect of an increased density of vacancies was neglected in these considerations.

The damage pattern visible in Fig. 2 can be interpreted as a dislocation network with a mean dislocation spacing of λ ~30 nm. When assuming that these dislocations spread over the whole 150 nm thick Cu film, a dislocation density of $\rho_d \approx 2 \cdot 10^{10}$ cm^{-2} would exist. For the damaged zone this leads to a Taylor hardening of

$$\Delta\sigma_d = \alpha\sqrt{3}G_{Cu}b\sqrt{\rho_d} \approx 70\text{MPa}, \quad \text{(VI.2)}$$

whereby α = 0.25 is a numerical constant and $\rho_d = 2 \cdot 10^{10}$ cm^{-2}. An error in the dislocation density by an order of magnitude results in a factor of ~3 for σ_A.

Marien et al. [16] reported the formation of precipitates with a radius r_p ~1.4 nm. If we assume a Ga concentration and penetration depth as observed in our AES measurements, the precipitates would possess an average spacing of l_p ~10.2 nm. Considering a simple Orowan type hardening mechanism, the precipitates would cause a local increase in flow stress $\Delta\tau_p$ by:

$$\Delta\tau_p = \frac{G_{Cu}b}{l_p - 2r_p} \approx 1600\text{MPa}. \quad \text{(VI.3)}$$

Such a remarkable rise in flow stress is unlikely to occur in the tested specimen, as these small precipitates will be cut by dislocations before the stress level to initiate the Orowan mechanism is reached. Concerning the possible strength reachable by precipitation hardening in Cu, Kudashov et al. [38] reported flow stresses in the order of 650 MPa for various oxide-dispersion strengthened UFG copper samples. Still, one has to keep in mind that the oxide particles used by Kudashov et al. possessed average diameters between 30 nm and 50 nm, compared to just several nm reported by Marien et al.. As the strengthening is expected to scale with r_p^{-1}, this might lead to significantly different stress levels.

Using a simple composite model to estimate the influence of such a precipitation hardened damage layer on the total stress σ_{tot} of the Cu compression sample gives:

$$\sigma_{tot} \approx \sigma_{Cu}\left(1 - \frac{4(t_a + t_d)}{d}\right) + \frac{\Delta\tau_p}{m}\left(\frac{4t_d}{d}\right), \quad \text{(VI.4)}$$

where σ_{tot} is the total measured stress, σ_{Cu} is the flow stress of the unaltered material, m = 0.278 is the Schmid factor to convert the shear stress into a flow stress for a [100] oriented Cu single crystal (e.g. [7]), and d, t_a, t_d are indicated in

Fig. 9. An evaluation of equation (4) is difficult, as σ_{Cu} is expected to be size-dependent and $\Delta\tau_p$ must be estimated, as the mechanical properties of the precipitates are unknown.

Taking the scaling behaviour of σ_{tot} as found in [7] and a thickness of the damaged layer of 50 nm, $\Delta\tau_p \approx 500$ MPa was calculated. Therefore, due to the decreasing d also the higher order terms neglected in equation (4) were taken into account. The size-dependent ratio between σ_{Cu} and σ_{tot} for an Orowan hardened layer with t_d = 50 nm, 25 nm, and 10 nm width and $\Delta\tau_p$ = 500 MPa is shown in Fig. 10. The critical pillar diameter for a deviation of the actual strength compared to the total strength larger than 10% is for a damaged width t_d = 50 nm 10 µm, for t_d = 25 nm 2.5 µm, and for t_d = 10 nm below 100 nm. We conclude therefore that FIB damage definitely limits the applicability of micro-compression tests. However, with grazing Ga incidence the critical size is clearly in the submicron dimensions.

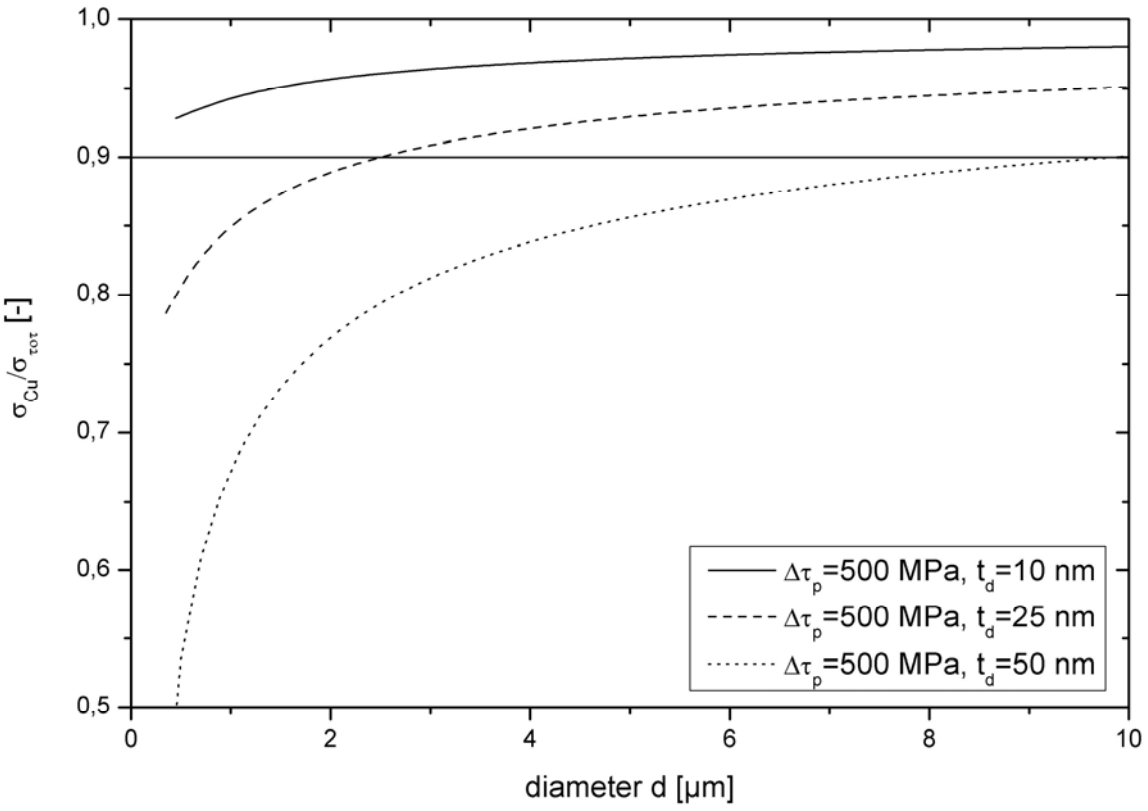

Fig. 10: Size-dependent ratio between the flow stress in copper σ_{Cu} and the total measured stress σ_{tot} for $\Delta\tau_p$ = 500 MPa and a thickness of the damaged layer t_d = 50 nm, 25 nm, and 10 nm.

Additionally other effects, such as segregation, may play an important role by completely altering the deformation behaviour. For example it is well known that less than a few at% Ga in Al lead to grain boundary embrittlement [39, 40]. Therefore, a critical examination of the damage mechanisms for complex materials (e.g. materials including grain or phase boundaries, or biological materials) has to be performed prior to micromechanical tests. “Unexpected” mechanisms like grain boundary embrittlement as mentioned before can have a large impact on the mechanical properties for even larger samples.

5. Conclusions

TEM and AES investigations were performed to elucidate the damage experienced by Cu exposed to Ga^+ ion bombardment. The influences of ion energy, ion dose and incidence angle were examined. Conventional TEM studies reveal the necessity to reduce the Ga damage by reducing the ion energy, milling current, and incidence angle, if pre-existing defects are to be analyzed. AES measurements were conducted to quantify the concentration and penetration depth of the Ga^+ ions. Ga concentrations as large as ~20 at% were found close to the surface of polycrystalline Cu. The penetration depth reaches up to ~50 nm for 30 keV Ga^+ ions. This value is in agreement with the width of the amorphous layer found in the TEM investigations and the predictions from Monte Carlo simulations. Possible consequences on the mechanical properties indicate stress increases of several MPa when assuming solid solution hardening, in the order of 100 MPa assuming Taylor hardening, and up to the GPa range for precipitation hardening. Thus, care has to be taken for miniaturized mechanical test samples with submicron dimensions designed by FIB.

References

[1] M. W. Phaneuf, Micron 1999; 30: 277.

[2] M. D. Uchic, D. M. Dimiduk, J. N. Florando, and W. D. Nix, Science 2004; 305: 986.

[3] D. M. Dimiduk, M. D. Uchic, and T. A. Parthasarathy, Acta Mater. 2005; 53: 4065.

[4] J. R. Greer, W. C. Oliver, and W. D. Nix, Acta Mater. 2005; 53: 1821.

[5] C. Motz, T. Schöberl, and R. Pippan, Acta Mater. 2005; 53: 4269.

[6] C. A. Volkert and E. T. Lilleodden, Phil. Mag. 2006; 86: 5567.

[7] D. Kiener, C. Motz, T. Schöberl, M. Jenko, and G. Dehm, Adv. Eng. Mater. 2006; 8: 1119.

[8] S. Rubanov and P. R. Munroe, J. Mater. Sci. Lett. 2001; 20: 1181.

[9] S. Rubanov and P. R. Munroe, J. Microscopy 2003; 214: 213.

[10] Z. Wang, T. Kato, T. Hirayama, N. Kato, K. Sasaki, and H. Saka, App. Surf. Sci. 2005; 241: 80.

[11] J. P. McCaffrey, M. W. Phaneuf, and L. D. Madsen, Ultramicroscopy 2001; 87: 97.

[12] S. Rubanov and P. R. Munroe, Mater. Lett. 2003; 57: 2238.

[13] R. B. Jamison, A. J. Mardinly, D. W. Susnitzky, and R. Gronsky, Microsc. Microanal. 2000; 6: 526.

[14] J. F. Ziegler, J. P. Biersack, and U. Littmark, *The Stopping Range of Ions in Matter* (Pergamon Press, New York, 1985).

[15] B. I. Prenitzer, C. A. Urbanik-Shannon, L. A. Giannuzzi, S. R. Brown, R. B. Irwin, T. L. Shofner, and F. A. Stevie, Microscopy and Microanalysis 2003; 9: 216.

[16] J. Marien, J. M. Plitzko, R. Spolenak, R.-M. Keller, and J. Mayer, J. Microscopy 1999; 194: 71.

[17] D. J. Larson, D. T. Foord, A. K. Petford-Long, H. Liew, M. G. Blamire, A. Cerezo, and G. D. W. Smith, Ultramicroscopy 1999; 79: 287.

[18] C. R. Hutchinson, R. E. Hackenberg, and G. J. Shiflet, Ultramicroscopy 2003; 94: 37.

[19] J. Yu, J. Liu, J. Zhang, and J. Wu, Mater. Lett. 2006; 60: 206.

[20] J. M. Cairney and P. R. Munroe, Micron 2003; 34: 97.

[21] T. J. Balk, G. Dehm, and E. Arzt, Acta Mater. 2003; 51: 4471.

[22] T. Hebesberger, H. P. Stüwe, A. Vorhauer, F. Wetscher, and R. Pippan, Acta Mater. 2005; 53: 393.

[23] T. L. Matteson, S. W. Schwarz, E. C. Houge, B. W. Kempshall, and L. A. Giannuzzi, J. Electron. Mat. 2002; 31: 33.

[24] B. N. Singh and S. J. Zinkle, J. Nuc. Mater. 1993; 206: 212.

[25] D. Kiener, R. Pippan, C. Motz, and H. G. M. Kreuzer, Acta Mater. 2006; 54: 2801.

[26] H. Ryssel and I. Ruge, *Ion Implantation* (Wiley and Sons, New York, 1986).

[27] J. Melngailis, J. Vac. Sci. Tech. B 1986; 5: 469.

[28] T. Ishitani and H. Kaga, J. Electron Microsc. 1995; 44: 331.

[29] L. A. Giannuzzi and F. A. Stevie, *Introduction to focused ion beams* (Springer, New York, 2005).

[30] M. J. Caturla, N. Soneda, E. Alonso, B. D. Wirth, T. Díaz de la Rubia, and J. M. Perlado, J. Nuc. Mater. 2000; 276: 13.

[31] M. W. Phaneuf and J. Casey, Microsc. Microanal. 2002; 8: 52.

[32] D. B. Williams and C. B. Carter, *Transmission Electron Microscopy* (Springer, New York, 1996).

[33] L. H. Friedman and D. C. Chrzan, Phil. Mag. A 1998; 77: 1185.

[34] B. von Blanckenhagen, E. Arzt, and P. Gumbsch, Acta Mater. 2004; 52: 773.

[35] R. L. Fleischer, Acta Met. 1961; 9: 996.

[36] R. L. Fleischer, Acta Mater. 1963; 11: 203.

[37] R. Phillips, *Crystals, Defects and Microstructures - Modeling Across Scales* (University Press, Cambridge, 2001).

[38] D. V. Kudashov, H. Baum, U. Martin, M. Heilmaier, and H. Oettel, Mater. Sci. Eng. A 2004; 387-389: 768.

[39] S. Schmidt, W. Sigle, W. Gust, and M. Rühle, Z. Metallkd. 2002; 93: 428.

[40] E. Pereiro-Lopez, W. Ludwig, D. Bellet, and C. Lemaignan, Acta Mater. 2006; 54: 4307.

VII Summary

Miniaturized compression experiments reveal a geometrical size effect of the flow stress of micron-sized single crystal specimens in the absence of strain gradients. This behaviour was unexpected and could not be explained by established theories of crystal plasticity. Emerging theories focus on two different basic assumptions. While one theory assumes a lack of available dislocations to accommodate the deformation at such small length scales, the other considers the truncation of sources in the small sample volumes prepared from larger crystals. In order to understand crystal plasticity at these dimensions, it is a prerequisite to identify the mechanisms governing the geometrical size effect. Within this context, it is a powerful approach to monitor the compression experiment time-resolved at high lateral resolution.

We developed a system allowing us to perform miniaturized loading experiments *in-situ* by mounting a microindenter in a scanning electron microscope. Besides high accuracy in alignment between sample and punch prior to loading, this provides insight into the deformation process during compression testing. A focussed ion beam workstation was used for sample fabrication. We prepared single crystal copper compression samples with a (111) surface and compared the observed size effect in flow stress to micro-bending experiments of the same material to highlight the influence of a strain gradient on the determined properties. Furthermore, the compression results were compared to mechanical data for copper obtained by other miniaturized deformation techniques to verify the validity of our method. Additionally, we were able to describe the flow stress of copper over several orders of magnitude by applying a modified Hall – Petch relation including a source term.

Comparable to the macroscopic world, microscopic compression tests pose several problems or limitations, for example; friction at the interface between punch and specimen, limited aspect ratios to avoid plastic buckling, an additional compliance at the sample base, and local stress concentrations due to the specimen geometry. We investigated this by loading different sample geometries with (111) and (100) crystal orientations and demonstrated that stress

concentrations at the sample base can be strong enough to cancel the geometrical size effect.
Investigation of the local crystal orientation after compression testing depicted distinct lattice misorientations. A dislocation based deformation model was introduced to explain the macroscopic deformation and the local lattice rotations. This also highlighted the importance of the interface between sample and punch, depicting dislocations piled-up at this interface. The back stress of these dislocations on the acting sources strongly contributes to the observed size-effect in micro-compression.

To eliminate this aforementioned interface and the other limitations inherent to compressive loading, a novel micro-tensile testing method was developed. Using this approach, the influence of sample dimensions and aspect ratio on the observed size effect was examined using single crystal copper specimens with a <-2 3 4> crystal direction parallel to the loading direction. For short gauge lengths we observed a dramatic rise in flow stress and significant hardening caused by dislocation pile-ups. The specimens with high aspect ratios showed reduced hardening and a weak size dependence of the measured flow stress. Furthermore, the flow stresses observed in micro-tension are well below the stresses determined in micro-compression. This is attributed to the additional constraints present in the compression tests.

A comparison of the size dependent shear stresses observed in micro-compression and micro-tension is shown in Fig. 1. For each crystal orientation the highest Schmid factor was used to convert flow stress to shear stress. The micro-compression specimens had an aspect ratio of 2:1, while the aspect ratios of the micro-tensile specimens are indicated in the diagram.

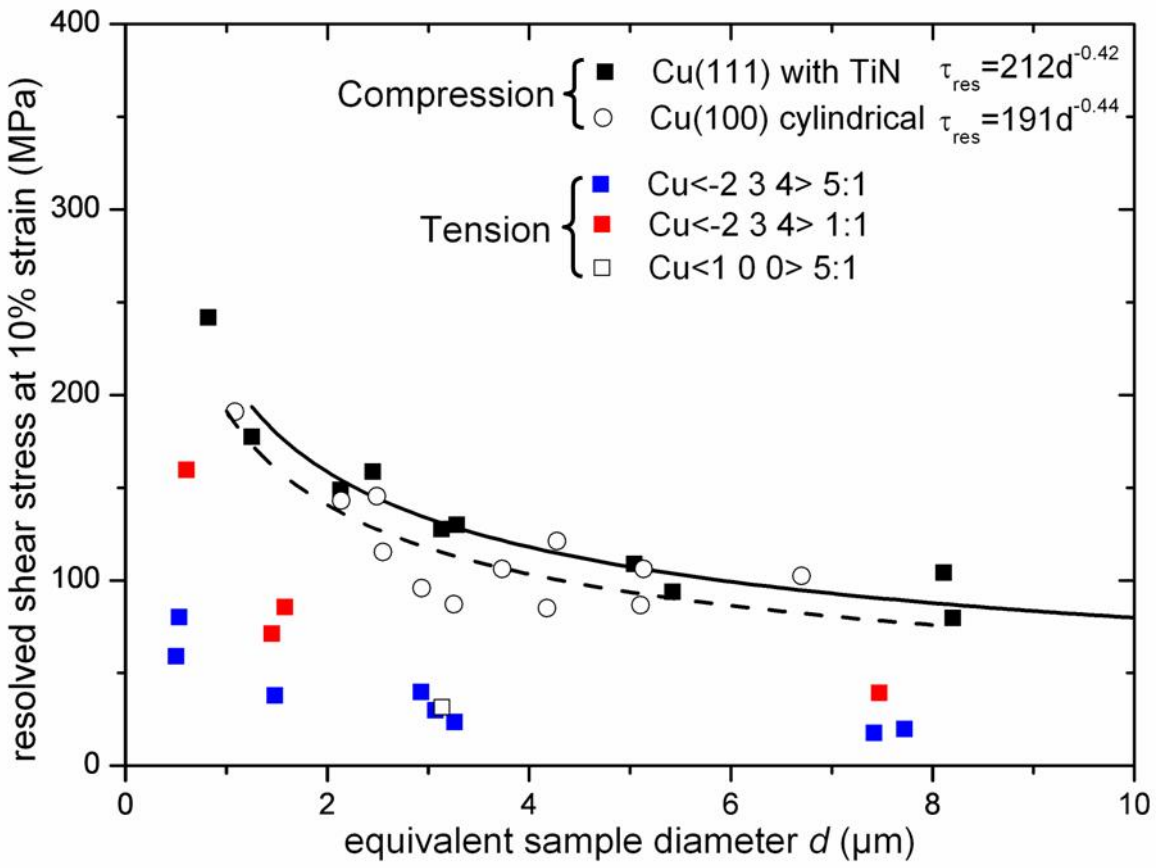

Fig. 1: Comparison between the size-dependent resolved shear stress in micro-compression and micro-tension. The crystal orientations of the different specimen are indicated in the diagram. The highest Schmid factor for each orientation was applied to convert flow stress to shear stress.

An important point to consider is the unintentional introduction of defects including also dislocation sources due to focussed ion beam machining. We conducted transmission electron microscopy investigations to characterize the defects induced by the Ga^+ ion bombardment of the sample along with depth sensing Auger electron spectroscopy to measure the concentration of implanted Ga atoms. Furthermore, taking into account all possible hardening mechanisms, a composite model was developed to quantify the influence of a surface layer with modified properties on the determined flow stresses.

To what extend these introduced defects act as dislocation sources is, at the moment, unknown and subject to further investigations. Several strategies to avoid this damage, in terms of utilizing different fabrication techniques or completely removing it by heat treatment, plasma cleaning, or etching procedures, are under consideration.

I totally agree with a statement made by John Ruskin:
“Say all you have to say in the fewest possible words, or your reader will be sure to skip them; and in the plainest possible words or he will certainly misunderstand them.”

Therefore, I will conclude in only two sentences:
To investigate the small scale mechanics of almost any kind of material, we developed a novel *in-situ* micro-tensile method which is easy to perform, highly sensitive, and less susceptible to artefacts than other methods.
Applying this method, we contributed significantly to the current understanding of mechanical size effects in crystal plasticity at small length scales by revealing unexpected dislocation pile-ups.

VIII List of Publications

C. Motz, D. Kiener, H. Kreuzer, W. Prantl, R. Pippan

Microstructural characterization of deformed volume beneath microindentations using FIB, EBSD and TEM

In: Proceedings of the 25th Risø International Symposium on Material Science: Evolution of Deformation Microstructures in 3D, eds. C. Grundlach, K. Haldrup, N. Hansen, X. Huang, D. Juul Jensen, T. Leffers, Z.J. Li, S.F. Nielsen, W. Pantleon, J.A. Wert, G. Winther, pp. 459-464 (2005).

M. Faleschini, D. Kiener, W. Knabl, R. Pippan

Fracture Toughness Investigations of Tungsten Alloys and Severe Plastic Deformed Tungsten Alloys

In: Proceedings of 16th International PLANSEE Seminar, eds. G. Kneringer, P. Roedhammer, H. Wildner, Vol. 1, pp. 701-711 (2005).

C. Motz, D. Kiener, T. Schöberl, R. Pippan, G. Dehm

Fokussierte Ionenstrahl-Technik (FIB) in der Mikro- und Nanomechanik

In: Handbuch der Nanoanalytik Steiermark, ed. W. Rom, pp. 162-163 (2005).

C. Motz, D. Kiener, T. Schöberl, R. Pippan, G. Dehm

Sekundärionen-Massenspektroskopie (SIMS) mittels FIB

In: Handbuch der Nanoanalytik Steiermark, ed. W. Rom, pp. 199-200 (2005).

D. Kiener, R. Pippan, C. Motz, H. Kreuzer

Microstructural evolution of the deformed volume beneath microindents in tungsten and copper

Acta Materialia, Vol. 54, pp. 2801-2811 (2006).

D. Kiener, C. Motz, T. Schöberl, M. Jenko, G. Dehm

Determination of mechanical properties of copper at the micron scale

Advanced Engineering Materials, Vol. 8, pp. 1119-1125 (2006).

D. Kiener, C. Motz, M. Rester, M. Jenko, G. Dehm

FIB damage of Cu and possible consequences for miniaturized mechanical tests

Materials Science and Engineering: A, Vol. 459, Issues 1-2, pp. 262-272 (2007).

S.H. Oh, M. Legros, D. Kiener, P. Gruber, G. Dehm

In situ TEM straining of single crystal Au films on polyimide: Change of deformation mechanisms at the nanoscale

Acta Materialia, Vol. 55, pp. 5558–5571 (2007).

M. Faleschini, H. Kreuzer, D. Kiener, R. Pippan

Fracture toughness investigations of tungsten alloys and SPD tungsten alloys

Journal of Nuclear Materials, Vol. 367–370, pp. 800–805 (2007).

D. Kiener, M. Rester, S. Scheriau, B. Yang, R. Pippan, and G. Dehm

Influence of External and Internal Length Scale of the Flow Stress of Copper

International Journal of Materials Research, Vol. 98, Issue 11, in press (2007).

D. Kiener, W. Grosinger, G. Dehm, R. Pippan

A further step towards an understanding of size-dependent crystal plasticity: *In-situ* tension experiments of miniaturized single crystal copper samples

Acta Materialia, accepted (2007).